Neural correlates of human motor planning and visuomotor transformation

Jing "James" Wu

A dissertation
submitted in partial fulfillment of the
requirements for the degree of

Doctor of Philosophy

University of Washington

2019

Reading Committee:

Rajesh P.N. Rao, Chair

Jeffrey G. Ojemann, Chair

Eric H. Chudler

Program Authorized to Offer Degree:
Bioengineering

University of Washington

Abstract

Neural correlates of human motor planning and visuomotor transformation

Jing "James" Wu

Co-Chairs of the Supervisory Committee:
Professor Rajesh P.N. Rao
Computer Science and Engineering

Professor Jeffrey G. Ojemann
Neurological Surgery

Goal-oriented coordinated movement is an everyday feat of computation, the mundaneness of which belies its immense complexity. When we lose function in disease or injury, however, we realize that our understanding of the neural bases of coordinated movements is currently insufficient to use engineered solutions to fully restore function.

Neural engineering for the restoration of goal-oriented motor function requires a more complete understanding of how context-dependent information might flow throughout the cortico-basal-ganglia motor circuit, and be informed by spatial cues and existing task-oriented memory. Successful design of bidirectional neurotechnology—with both feedforward model predictions and cortical stimulation feedback—may therefore require not only the state of movement neural correlates in the sensorimotor cortex, but also representations of spatial context and goal coordinates informed in part by hippocampal and subiculuar structures. A combination of deep-brain and surface cortical electrodes may be required to engineer functional neurotechnology capable of restoring spatially-aware volitional movement and sensory feedback.

We explore some of the cortical dynamics underlying movement visualization - specifically grasp preshaping, and our ability to adapt to rotated movement perspectives in virtual

fixed-viewpoint maze navigation in order to explore these complex interactions of movement, imagined movement goals, and task space. We use electrocorticography and stereo-electroencephalography electrodes clinically implanted in patients to interrogate the underlying neural substrates of human sensorimotor computation. We use the state trajectories of the spectral power sampled by these aggregate field potential-coupling electrodes to work towards a more thorough understanding of the neural dynamics underlying movement control, expand our understanding of the complex visual-spatial-motor interactions of the human body, and move towards a more complete implementation of complex, spatially aware neural technology.

ACKNOWLEDGMENTS

This work would not be possible without the help and guidance of a number of people. The author in particular wishes to express sincere appreciation to the faculty who made it possible: Drs. Jeff Ojemann and Rajesh Rao for the opportunity of investigating human cortex with computation, Eric Chudler for mentorship, Bing Brunton for amazing guidance, Felix Darvas for our discussions, Kurt Weaver for insight and support, Azadeh Yazdan-Shahmorad, Tamara Bonaci, Jeff Herron, and all of the Center for Neurotechnology (formerly Center for Sensorimotor Neural Engineering) at the University of Washington.

This work would similarly not be possible without dear colleagues, many of whom laid the foundation of this thesis with ample discussions and ideas. This includes, but is not limited to, Drs. and future Drs., scientists and engineers: Kaitlyn Casimo, David Caldwell, Jenny Cronin, Nile Wilson, Kelly Collins, Clark Guo, Katie Ly, Lila Levinson, Tim Brown, Katherine Pratt, Maggie Thompson, Luke Bashford, Arvid Guterstam, Jared Olson, Jeremiah Wander, Devapratim Sarma, Vikash Kumar, Tim Blakely, and Tim Blanche.

Most importantly, this work would not be possible without the ceaseless support of my partner Shirley Leung, my best friend Lissette Wilensky, and all of my family who have raised me to be a loving and caring person. My whole life is your work.

We finally acknowledge that this work was done on the unceded land of the Duwamish Tribe, the People of the Inside. The city of Seattle, the University of Washington, and I owe you our livelihoods on this land.

TABLE OF CONTENTS

LIST OF FIGURES

Chapter 1

ORGANIZING MOVEMENT

1.1 Sensorimotor Complexity

Living animals, including humans, have the unique ability to coordinate goal-oriented movement. For a majority of us from an early age, we stumble to eventually learn highly complex and organized movements that are incredible feats of coordination and computational prediction. These feats include balancing our flexible pose-shifting bodies on a single leg while in motion; grasping and moving topologically complex sheets of fabric into flowing organic shapes of our own choosing; or carefully navigating through the maze of our world, while inferring from brief glances, ground texture, obstacle shape, and the intent of other thinking beings. We regard *sports*, *sewing*, and *driving* as mundane activities which able-bodied individuals are able to accomplish daily. But this perspective belies the immense organization, model prediction, sensory fusion, and sheer computation that are so fundamental to these everyday feats.

In 1980s, renowned Carnegie Mellon robotics and artificial intelligence researcher Hans Moravec observed:

> "Encoded in the large, highly evolved sensory and motor portions of the human brain is a billion years of experience about the nature of the world and how to survive in it. The deliberate process we call reasoning is, I believe, the thinnest veneer of human thought, effective only because it is supported by this much older and much more powerful, though usually unconscious, sensorimotor knowledge.
>
> We are all prodigious Olympians in perceptual and motor areas, so good that we make the difficult look easy. Abstract thought, though, is a new trick, perhaps less than 100 thousand years old. We have not yet mastered it. It is not all that intrinsically difficult; it just seems so when we do it."[1]

In its essence, Hans Moravec predicted that the most difficult of our evolved skills to replicate

using technology would likely be the ones to which we are least consciously aware and most likely to consider mundane. This prediction is often called *Moravec's Paradox*.

That everyday sensorimotor function might be among the most difficult forms of computation is perhaps one of the only early predictions about artificial intelligence that have consistently held true in our current generation of rapidly shifting technological infrastructure [2]. Our ability to design and manufacture computing power has risen exponentially year over year. Further, algorithmic breakthroughs allow for artificial intelligence applications that required incredible human and computing capital one year to run on just consumer devices the next. One such algorithmic example is the `word2vec`, which allowed for effective natural language processing to move from large servers to personal computers [3]. Physical simulation, symbolic manipulation, vision, recognition, game-playing, and increasingly human language are becoming fields of development, engineering, and finally commoditized consumer products.

But unlike the above examples, our evolved and learned abilities to organize complex movement has, to date, stymied our ability to engineer similar-performing solutions. Much of the complexity surrounding what we might consider everyday simple movements can be attributed to problems of high dimensionality, deformation, and unpredictability, all of which present problems living animals have evolved to navigate for our survival.

First, sensorimotor behavior is referred to as *high dimensional*, as the number of movable joints, joint shapes, ligaments, tendons, and muscles that make up the complex system of hands, arms, feet, and legs, also form highly underdetermined systems with many degrees of freedom. This implies that for any particular task such as holding a rock steady, we have far more moving degrees of freedom than is necessary. Simple pincers might do in accomplishing that single task. However, we must use the same limb to accomplish a dazzlingly wide variety of tasks and apply a wide array of tools. As such, our hands are better thought of as actuators, with varying degrees of suitability, capable of accomplishing the superset of all our tasks. Second, biological structures possess a high degree of *deformation*; fluid and viscoelastic mechanics are difficult to predict using only simplified, rigid-body mechanics.

This increases the complexity of computation significantly in order to determine physical outcomes in terms of contact patch, area, resulting forces on limb, and the composition of the object, shear, and friction of contact. Due to the unique nature of these mechanics, some researchers have attempted to name the unique set of dynamical constraints under deformation "terradynamics" [4]. Finally, the principles of our biochemical and electrical perception, communication, and execution in our nerves and end effectors means that a large amount of sensory and control noise is present throughout the system, giving a large factor of computational uncertainty. The degree to which our innate control strategies are highly resistant to input and execution noise further adds mystery to the mechanics of our sensorimotor control strategies.

1.2 Clinical and Social Impact

The dramatic complexity of sensorimotor systems also means that impairment of these sensorimotor systems carries heavy individual and societal burden. Volitional movement impairments can significantly interfere with the quality of life in individuals living with motor and sensory deficits as a result of stroke or paralysis due to spinal cord injury, with limited medical or technological interventions that can restore full function to a pre-injury condition. This can imply impairments in daily travel, navigation, movement, eating, object and tool use, or even speaking and controlling the direction of vision. In particular, approximately 5 million Americans suffer from some form of paralysis, with large social and economic impact in daily living and capacity to work. Estimates of costs and economic impact of stroke and paralysis can be as much as $40 billion in the US alone [5]. While the loss of quality of life differs between individuals, both quantitative and qualitative analyses of engineered interventions reveal a clear clinical need for improved intervention, though not at the expense of access [6] .

A wide array of rehabilitation methodology, rehabilitation-assistive devices, as well as mechanical and biological interventions have been developed in order to address this underserved clinical need. In particular, technologies that have been developed include various

passive and powered prosthetics, noninvasive transcutaneous spinal stimulation [7], and pluripotent stem cell transplants. These interventions, ranging from commonplace to highly experimental, have offered some restoration of sensory deficits or motor function. However, in order to develop better rehabilitation techniques, quantify impairment, and identify root cause sensorimotor deficits, better understanding of the underlying control structure—where deficits may lead to a loss of volitional control—need to be carefully studied.

However, expanding sensorimotor systems knowledge is not without some degree of social impact. A large portion of skilled jobs in the global economy are dependent on human sensorimotor supremacy over current forms of robotic automation, especially for unpredictable manipulation of flexible, liquid, or viscoelastic materials in our everyday lives. Cooking, folding, sewing, cleaning, farming, and other forms of versatile tool use remain difficult-to-automate pools of jobs today. Increased ability to reproduce these complex sensorimotor skills in technology can lead to a variety of socioeconomic consequences. However, due to the unique need of these skills in restoring human quality of life, and the possibility of producing large improvements in quality of life without similar mastery of sensorimotor computation, the trade-off may be worthwhile. The importance of recognizing the trade-off and the danger research can pose due to misuse, however, is an important aspect of ethical engineering.

1.3 Intracranial Electrophysiology

Given the nature of the above complex limitations, what is the role neural engineering might play in uncovering the principles of our sensorimotor function? First, the modality of direct access to the substrate of neural computation may lead to some insights into the structures of hidden states that underlie the overall phenomena. Second, our ability to understand the system likely requires uncovering the hidden dynamic functions or states of a system, as illustrated in Fig. 1.1.

To interrogate these hidden states, a wide variety of methods to measure a proxy of neural activity have been devised. This includes functional magnetic resonance imaging (fMRI), magnetoencephalography (MEG), positron emission tomography (PET), functional near-

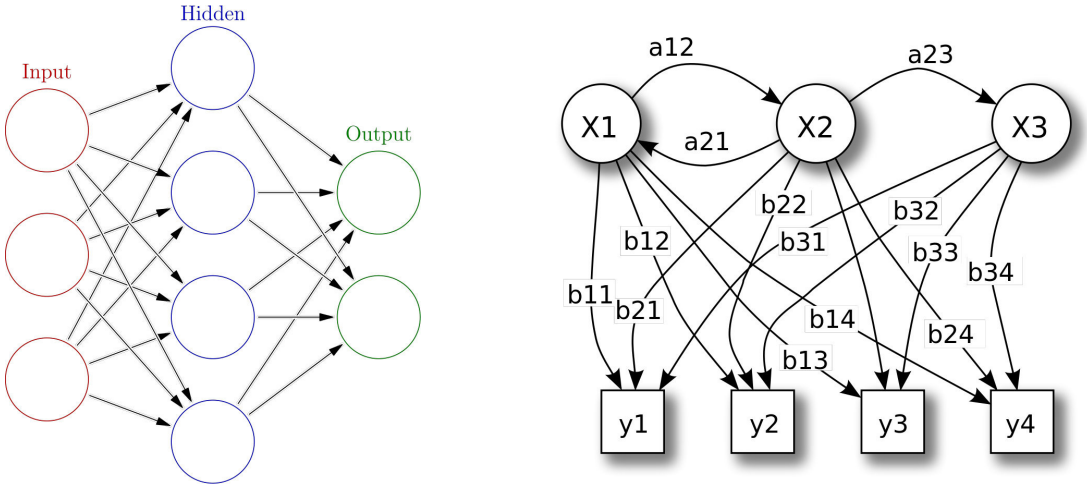

Figure 1.1: Left: Hidden layers translate observed inputs to observed outputs, but a complete understanding require probing of the hidden layer. Right: Understanding of the hidden states in Hidden Markov Models give the full state space of the system. Adapted from [8] and [9] respectively.

infrared spectroscopy (fNIRS), and a variety of functional electrophysiology. In particular, electrophysiology tools for studying the brain benefit from the lack of need for pharmaceutical radiotracers, the lack of need for large shielded rooms or nitrogen-cooled superconductive coils, and relative prevalence due to the ability to leverage low-cost consumer electronics advances in integrated technology. Additionally, they also possess the benefit of high temporal resolution (1ms samples or faster), and a high degree of versatility and scalability in terms of spatial resolution and degree of spatial coverage.

Electrophysiological tools have been used to detect either the depolarizing activity at individual neurons (single unit), the secondary biochemical gradient flow near individual neurons (local field potential, or LFP), or the aggregate activity of a large population of neurons, often in the order of 10^5 or 10^6 in each aggregate signal. Unfortunately, very large scale recordings of 10^3 or more individual neurons or LFPs are extremely costly, and very rarely done in human subjects during the timeline of this work. The latter mechanism of

aggregate field potential signals sees significantly more clinical and research usage, and is the primary research modality for this work.

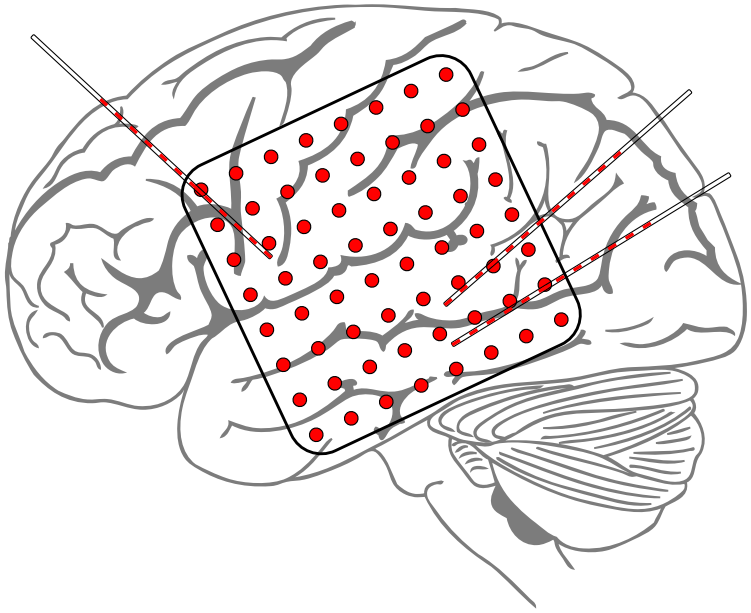

Figure 1.2: Electrocorticographic (ECoG) array, rectangular foreground with red electrode dot locations. Commonly used clinical size specifies 10mm between-electrode spacing, 3.5mm exposed electrode surface ($10mm^2$), and 2kΩ impedance. Stereotaxic EEG (sEEG) electrodes, three cylindrical depth implants illustrated. Commonly used clinical size specifies 6-16 electrodes down the cylindrical shaft, 5mm spacing, 1.1mm diameter, 2.3mm length, $16mm^2$ exposed surface area, and 2kΩ impedance. Mean human brain, 15cm length, as size reference, gray background, adapted from [10].

While the precise mechanisms by which the cortex might generate these latter aggregate field potentials remain a contentious topic, a commonly accepted model involves *dipole theory*, or the dipole model. As hypothesized in this model, large sheets of parallel pyramidal neurons in cortical structures layers III and IV are structured in highly parallel sheets across the outermost gray matter surface of the human and primate neocortex. Activity causes these highly aligned neuron sheets to depolarize, and subsequently induce a large, slower secondary return current during the course of bringing the membrane potentials back into a pre-firing, polarized state. This secondary current flow induces a temporary dipole across the

neuron, focused at apical dendrites, with electric field lines emanating outside the skull where the aggregate volume conduction of in-phase neurons are located on a gyrus [11]. In turn, these much larger, longer-lasting signals can be detected as oscillatory coupled activity using capacitive antennae, which are commonly implemented as disks or gel electrodes placed either outside the skull (electroencephalography, EEG), implanted inside the skull and draped over the surface of the cortex (electrocorticography, or ECoG), or embedded into deep neural tissue (stereotaxic EEG, sEEG) as seen in Fig. 1.2.

Due to the early discovery of EEG, early work in the detection of cortical states of movement, including [12], [13], or [14] tended to use electroencephaography. While this non-invasive modality is common and easy to use in healthy and able-bodied individuals with very minimal risk, the modality suffers from the issues of extreme spatial blurring due to distance and often requires compensation in the form of solving indeterminate inverse mapping, also known as source localization. Similarly, the signal-to-noise ratio of this modality suffers heavily as a result of the much higher coupling impedances between the electrode and skin barrier, often on the order of 10-100 kΩs, making the resulting miniscule coupled currents immensely susceptible to induced, capacitive, or thermal noise in the electrode, sensors, or circuitry. Instead, intracranially implanted electrocorticography [15], as well as stereotaxic electroencephalography [16], has been previously used to successfully record aggregate field potentials inside the skull, where the electrode-to-dipole distances are much closer, which is very significant since dipoles follow the inverse cube law where signal fades proportional to $1/r^3$ where r is distance. By having electrodes sit atop the pial surface or penetrate tissue to capture deep brain structures, ECoG and sEEG can obtain impedances in the range of 1kΩ and a signal-to-noise ratio approximately 10 times greater than EEG. These two general recording modalities are used in this work.

1.4 Upper-Limb Motor Control

When separated into component parts, the everyday action of reach-to-grasp is an orchestra. Visual identification of a target object is followed by the evaluation of its position in space

relative to the body, with a 3D transformation from visual space to egocentric body space. The complex inverse kinematics problem of moving a range of joints to a designated position in Cartesian space is solved in order to plan a series of joint angles and muscle activations. The solution space for this is very confounding; here exists a high degree of motor redundancy, where unlimited possible trajectories are present in a partially constrained (but not fully constrained) trajectory space, where some limb joints have some limited range of motion, but with varying orientations relative to the body in each solution. Evaluation of a candidate posture with which to grasp the target object is planned. After reaching the object, a grasp is applied, and continuous kinetic feedback keeps the object stable.

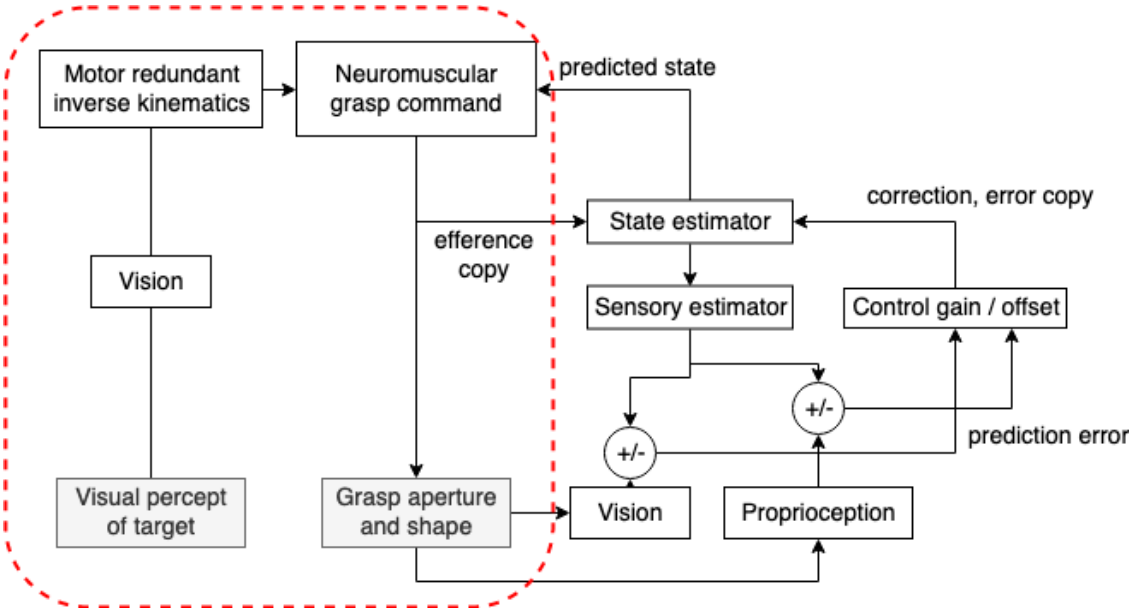

Figure 1.3: Example upper limb motor control systems diagram of feedforward and feedback models. This does not include models of motor redundancy solution. Left, red dotted box: these arm feedforward components constitute the major focus of this work. Adapted from [17].

Prior work into the examination of these intermediate hidden processes tends to model this behavior as one or more closed loops of control. These control loops incorporates visual, tactile, proprioceptive, and error feedback, all of which are integrated into feedforward and

feedback model predictions that adjust end-effector muscle actuation, as well as gain and parameters of intermediate model variables. Several theories of feedforward and feedback control, one of which is illustrated in 1.3 have been proposed over the years that optimize for varying hidden or output states in the model [18, 19, 20]. This includes optimization end goals of smoothness, minimization of end output uncertainty, or task outcome uncertainty [21].

In this work, we focus on the feedforward components of the model, with particular attention to the investigation of neurocorrelates of motor planning in arm movements and grasp preshaping prior to object contact. This focus on the feedforward aspects of the model hopes to disambiguate the neural circuits responsible for retrieving past experience from memory and derive motor plans from uncertain conditions with redundant solutions. Furthermore, we want to examine the potential independent hierarchical nature of these feedforward models: that is, are reach motor maps solved independently from grasp in differing circuits? The answer to this question may inform our ability to combine multiple neural correlates and electrophysiology-based inferences to help drive practical prosthetic usage, as well as reveal more about the distributed nature of sensorimotor neural computation.

1.5 Upper-Limb Movement Under Visual Perspective

Just as upper limb movement is a holistic system with various compensatory, predictive, and learning mechanisms distributed throughout the neocortex and basal ganglia, the interaction between spatial cues and motor movements is a similarly complex field.

Various parts of the visual-spatial-motor system have been studied individually in neuroscience, segmented by specific experimental design. For example, invasive rodent-in-maze spatial navigation studies using implanted microwire electrodes can localize populations of hippocampal and entorhinal neurons with correlated firing rate and phase precession to maze spatial location [22, 23]. Investigations into the underlying spatiotopy of this mechanism—how spatial mapping in the real world translate to the placement of these place-correlated cells—tentatively found both time-dependent [22] and context-dependent [24] underlying

structures. But this is still not sufficient to understand how we can effectively influence our movement given a set of visual snapshots of the world.

However, successfully inferring one's egocentric (self-centered) location in a 3D environment using only allocentric (objects-centered) visual cues must also require some degree of spatial transforms occuring in the brain, with rotational invariance as an assumption. That is, the environment should stay consistent even when visual perspective changes. Neurons that modify behavior with respect to rodent head direction (egocentric frame of reference), sometimes called *head-direction cells*, have been proposed to mediate the interaction between multiple frames of reference [25, 26]. These cells' location in the subiculum, directly between the hippocampus and the direct basal ganglial projections up to the sensorimotor cortex, hints strongly to their involvement in visual and motor systems.

Subiculum cells, however, are not the only neural structures that has been found to be involved in correction to visual rotational disturbances. Parallel bodies of work in the sensorimotor learning literature—usually based on tasks where humans or primates move 2D cursors towards prompted targets with varying degrees of angular error added as rotation inference—have pointed to the posterior parietal cortex as a central structure of learning to adapting to visuomotor change [27, 28, 29], with its own distinct learning and conslidation timescales and mechanisms.

In this work, we attempt to bridge these findings using a novel allocentric rotated-maze navigation task in human patients, controlled by upper-body movements, and characterize some of the capacities and the limits surrounding both these types of our neural circuits.

1.6 Layout of This Work

For our vision of the world to affect the movement of our bodies, human neural structures are responsible for the computation of a full chain of sensorimotor and visuospatial transformations, informed by past memory and experience. Some of these transformations from our senses to our movements can be captured in coupled field potentials in electrodes implanted in cortical tissue. Some well-timed aspects of movement such as kinematics and movement

onset have previously been localized to the sensorimotor areas of the cortex. However, more abstract aspects essential to our daily lives, such as movement visualization and adapting to changing spatial perspectives, may be a complex synergy of sensor fusion, motor learning, and spatial memory.

The following research is limited in scope and focused upon the direct prediction of upper-limb motor behavior from local field potential based cortical activity from humans implanted with electrocorticographic and stereotaxic electrodes. Its specific aims are classification of grasps from concurrent grasping movement, the feedforward aspects of movement with pre-movement cortical dynamics of direction, state space interpretation of movement visualization and visual movement follow, with a structure of movements, and the working model of posterior subiculum movements.

Chapter 2 focuses on building upon prior ECoG BCI grasp decoding paradigms by experimenting with a particular type of grasp kinematic decomposition: *non-negative antagonistic postural components*. We examine how this biomimetic decomposition attempt of high-dimensional grasp postures may correlate better with real-time ECoG spectral density in primary motor cortex representations of the hand, allowing for the potential of dynamic dexterous decoding. We also examine the potential linearities that may exist in kinetic grasp decoding in grasp-and-hold steady grip output tasks. Finally, we examine a successful application of decomposition of these high-dimensional grasp postures.

Chapter 3 focuses on examining the pre-movement kinetic features of limb movement, in order to examine our ability to predict motor output using only pre-movement cortical dynamics in relatively lower-density clinical ECoG electrode recordings. Using the same dataset, we also examine the flow of directionally-distinguishing information across the cortex, which may help illuminate independent hierarchical natures of limb movement models.

Chapter 4 focuses on imagined cortical dynamics of hand grasp preshaping. Comparing visually-guided overt grasp shaping with imagined grasp shaping, we examine the medium-term dynamics of these grasp movement transitions and use statistical shape matching methods to predict imagined hand grasp postures. We examine the template matching paradigms

of these long term dynamics.

Chapter 5 focuses on the proposed phenomena of *mental frame sync* in the performance of virtual visuomotor navigation tasks. We examine overt performance in a novel overt trackpad-controlled task, where camera view is rotated without rotation of the trackpad controls. Additionally, cues in the virtual environment allow the subject to re-reference their egocentric perspective with visual cues. We examine the neural correlates that correspond to differing task performance under differing maze rotation conditions, as well as one case study of interference in task performance in a rotation-specific condition.

Chapter 6 examines some of the tooling developed in the course of this work to address common issues faced with the use and deployment of electrophysiology recording infrastructure in an unpredictable clinical environment with patients and healthcare providers in the hopes that some of the difficulties in future work within these experimentally unique conditions can be alleviated.

Chapter 2

DIMENSIONALLY-REDUCED CORRELATES OF HUMAN UPPER-BODY MOVEMENTS FOR HUMAN BCI

2.1 PCA-Based Kinematic Movement Components

2.1.1 Introduction

The implementation of a brain-computer interface (BCI) capable of decoding neural intent into useful motor output can produce user-controlled volitional prosthetics [30, 14]. These neural interfaces possess great potential to drastically improve quality of life in individuals living with disability [31, 32]. BCIs have been proposed as a therapeutic modality for patients with severe paralysis, such as high traumatic spinal cord injury, to gain volitionally controlled function via robotic prosthetics or functional electrical stimulation. In particular, electrocorticography (ECoG) has been previously demonstrated as a recording modality with recorded activity associated with representation of upper-limb motor movement [33, 34, 35, 36, 37, 38, 39]. ECoG recordings as used in clinical seizure source localization [40] provide a stable source of field potential recordings with large coverage and, with relatively high degrees of signal to noise characteristics and temporal resolution in human subjects. and the ECoG-based BCI is a relatively recent development showing rapidly expanding promise in the past decade [39, 38, 41, 42].

However, the development of a rehabilitative upper-body prosthetic has posed a difficult challenge. In particular, with 27 articulating joints in the human hand-wrist system [43], the neural decoding and control of coordinated hand movements have been difficult due to a very high-dimensional state space. While existing efforts in ECoG BCI have been able to demonstrate activity associated with arm movement trajectories [44, 45], hand and finger movement [46, 47, 48, 49, 50], and various grasping actions [51, 52, 53, 54, 55] with

varying degrees of decoding success, current BCI frameworks for hand movement still rely on discrete hand positioning from a limited, fixed repertoire of possible hand positions or finger movements in a predetermined task timeline [48, 53, 54]. Existing solutions have not been able to allow for unscheduled, dynamic free-exploration and on-demand repositioning of complex hand postures in possible posture space in real time, and this lack of free control with real-time end-user error correction represents a barrier to volitionally-controlled hand-arm prostheses. Furthermore, the increasing success in deciphering finger movements has also been driven high-density electrocorticographic implants [50, 54]. While more spatial resolution is certainly more preferable, we believe it highly attractive to decode coordinated movements is from a sparse spatial resolution using the principles of underactuated control without the use of pre-screening motor areas followed by focal spatial sampling.

While the possible space of hand postures resides in a high dimensional space, these joint positions are driven by redundant and antagonistic motor units, and are not independently controlled given a specific set of contact positions and forces. As a result, by sacrificing flexibility for immediate access to functionality, the control of a large variety of functional grasps can be driven in real time in a much lower dimensional space from underactuated control signal sources and allow for complex grasping motions in 3D space. Existing physiological literature for decades has proposed combinatorial motor primitives, or muscle synergies, as possible mechanisms of high-complexity vertebrate motor control [56, 57, 58, 59], with up to 70% of the variance for possible space of hand shapes needed for clinically functional tool use captured in the first two "postural synergies", or principle component directions. While postural variance does not encompass all the intricacies of coordinated movement, they can serve as shortcuts for immediate access to function.

Improving upon previous methods, we perform postural decomposition of joint angles by "splitting" each principal component that serve as behavioral correlates into halves. We perform this decomposition under the rationale that grasp and ungrasp actions of the hand are actuated by antagonistic muscle groups. As such, they serve to pull the fingers apart in postural space from a postural neutral while at rest. We hypothesize that this non-

negative-factorialization-like decomposition may improve linear separation of these motor control correlates.

We investigate the representation the set of possible movements as a set of PCA-based synergies that allow for free exploration of hand postures in a lower dimensional space, and its application and performance in BCI in clinical ECoG monitoring subjects in controlling the movement of a virtual robotic hand.

2.1.2 Methods

Subjects and Recordings

Five subjects (ages 6-50, 1 female 4 male) with intractable epilepsy undergoing clinical seizure localization with long-term (4-10 days) electrocorticographic monitoring were included in the study, with written consent to participate in the University of Washington Institutional Review Board (UW IRB)-approved protocol. The experiment was performed under University of Washington Healthcare guidelines (Seattle, Washington, USA). The subjects were implanted with 8×8 platinum electrode grids (Ad-Tech, Racine, Wisconsin, USA) with 3mm electrode diameters embedded in silastic (Ad-Tech) with center-to-center distances of 10mm, based on necessary clinical indication. All subjects were BCI-naïve prior to the study and were asked to perform overt tasks while cortical activity and hand motion were experimentally recorded at the bedside without clinical recording interruptions. Recordings were captured using g.USBAmps (g.tec medical engineering GmbH, Schiedlberg, Austria) sampled at 1200 Hz, and the finger joint positions of the hand contralateral to grid implant were synchronously recorded with a 22-degree of freedom CyberGlove (CyberGlove Systems, San Jose, California, USA) in the software package BCI2000 [60].

Experimental Design

The study was divided into offline mapping and simulated decoding phases. Subjects were presented with six objects of varying sizes and shapes in a position optimal for eliciting

archetypal grasp types: power, precision/tripod, oblique, palmar/extension, spherical, and hook (Fig. 2.1) adopted in part from the Southampton Hand Assessment Procedure and the Toronto Rehabilitation Institute Hand Function Test [61, 62].

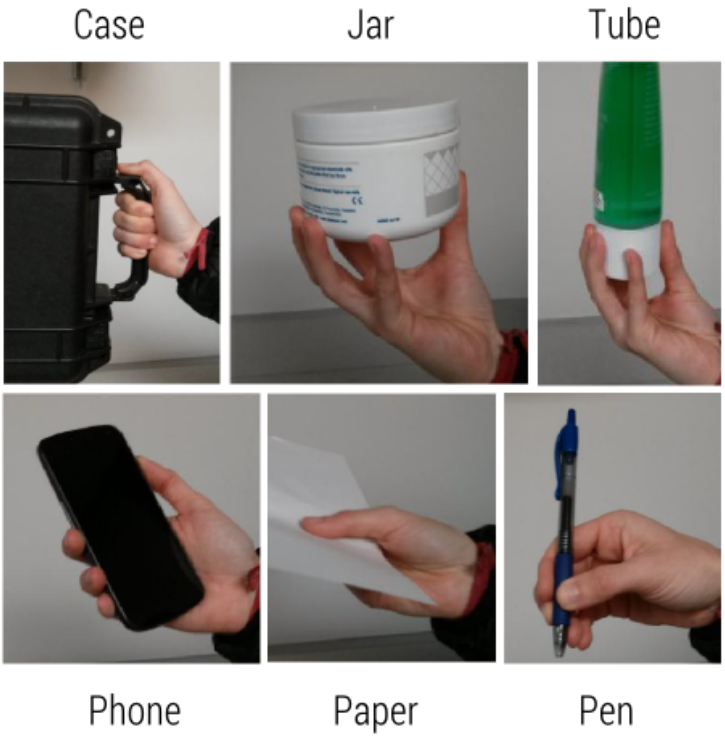

Figure 2.1: Six different grasping objects that elicit combinations of various archtypal grasp types when successfully grasped and held. Case (handle), Jar (lid), Tube (small lid), Phone, Paper, and Pen are used in this reach-and-grasp task. Hand and wrist joint angles are captured with an instrumented Cyberglove.

The subjects were first shown the target postures for grasping the objects, and then cued for two seconds to grasp, hold, and release the object with the hand contralateral to the grid implant, with three seconds of inter-trial rest time in between objects. Concurrently, the contralateral hand motion is captured by the Cyberglove with ECoG by the g.USBAmps. Each subject was cued to grasp at least 48 times in randomized order with equal numbers of each training object. The object was presented by the experimenter in the same position,

and the subjects were instructed to minimize arm and non-task related movements during the trials. In the decoding task phase, we explore the simulated ability of the subjects to control a virtual robotic arm in low dimensional synergy space for functional arm movements by replaying captured data through a real-time decoder onto a virtual 24-degree of freedom robotic hand [63] [64]. The similarity between decoded movements and captured movements are compared.

Time-frequency spectral power analysis

The recorded ECoG data at 1200 Hz was highpassed at 1 Hz to remove DC offset and notched filtered at 60 Hz with a 5 Hz width stopband to remove line noise, using a 4^{th} order acausal Butterworth filter. A common average reference filter is applied across each 8×8 grid. Estimated spectral power density time series for each channel of the grid are sampled at the nominal spectral resolution of 3 Hz and temporal resolution of 50ms using Welch's method of one-sided modified periodogram using Hanning windows of 400 sample length and 85% overlap. The subsequent extracted spectral power density between 70 and 150 Hz is averaged in order to obtain a broadband spectral power density for the high-γ spectra.

PCA-based hand movement synergies

Joint movements as recorded by the Cyberglove were upsampled by piecewise cubic hermite interpolating polynomial (PCHIP) interpolation [65] and individually normalized to known recorded maximum sensor ranges in order to obtain fractional range-of-movement estimates as an approximation of relative joint angle, and smoothed by a 1 Hz lowpass. The joint movements were then centered, and principal component analysis (PCA) was performed and truncated to the top three principal components in order to locate the three principle axes of the movement space with the maximum postural variance. The projected movements were then projected along the three-dimensional axes to form a reduced 3D trajectory of the movement time series, before numerical differentiation in order to obtain synergy velocities.

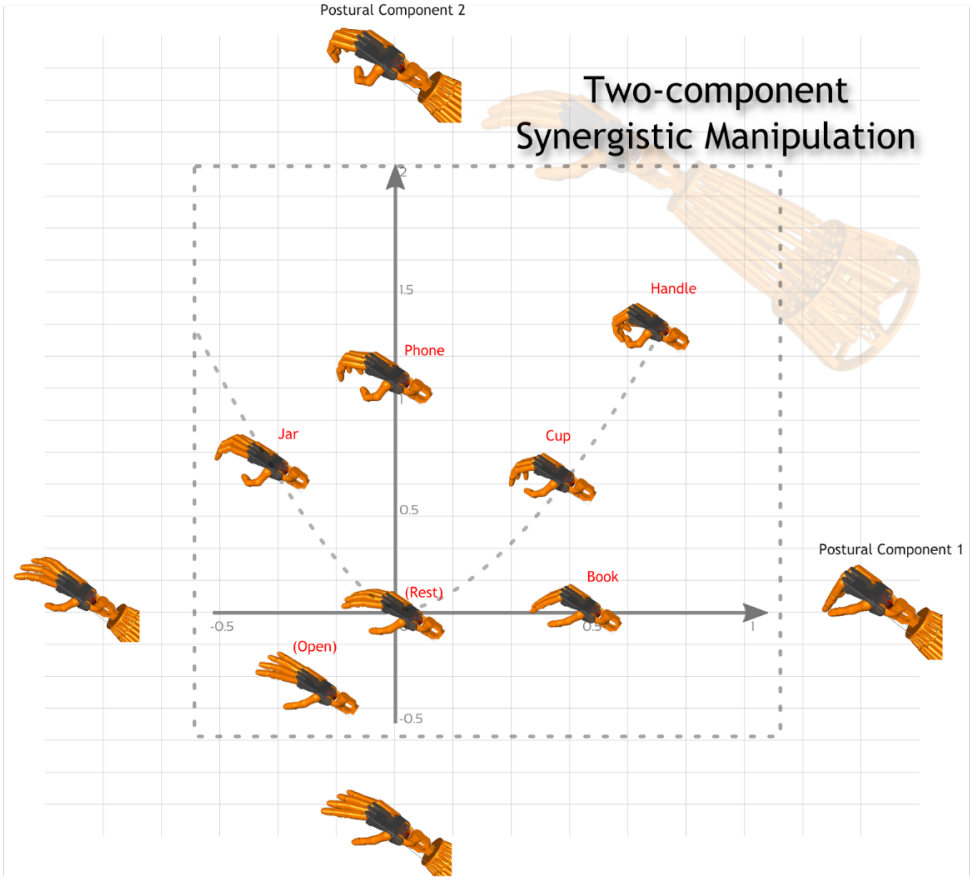

Figure 2.2: Overview of postural grasp mode / movement synergy mapping analysis, with multiple grasp types represented in the same reduced two-dimensional space. ECoG recordings and glove data are both used in pairwise analysis.

In order to separate the movement of antagonistic muscle group directions separately, the three synergy velocities are then divided along the zero crossings in each axis into 6 independent time series, where positive and negative movements in each postural component are separated into (+) and (-) movements, as seen in Fig. 2.3.

Spatial localization of synergy component correlates

Spatial-frequency relevance map of electrode-frequency pairs to each movement synergy component was located using pairwise cross-covariance between each of the 6 independent pro-

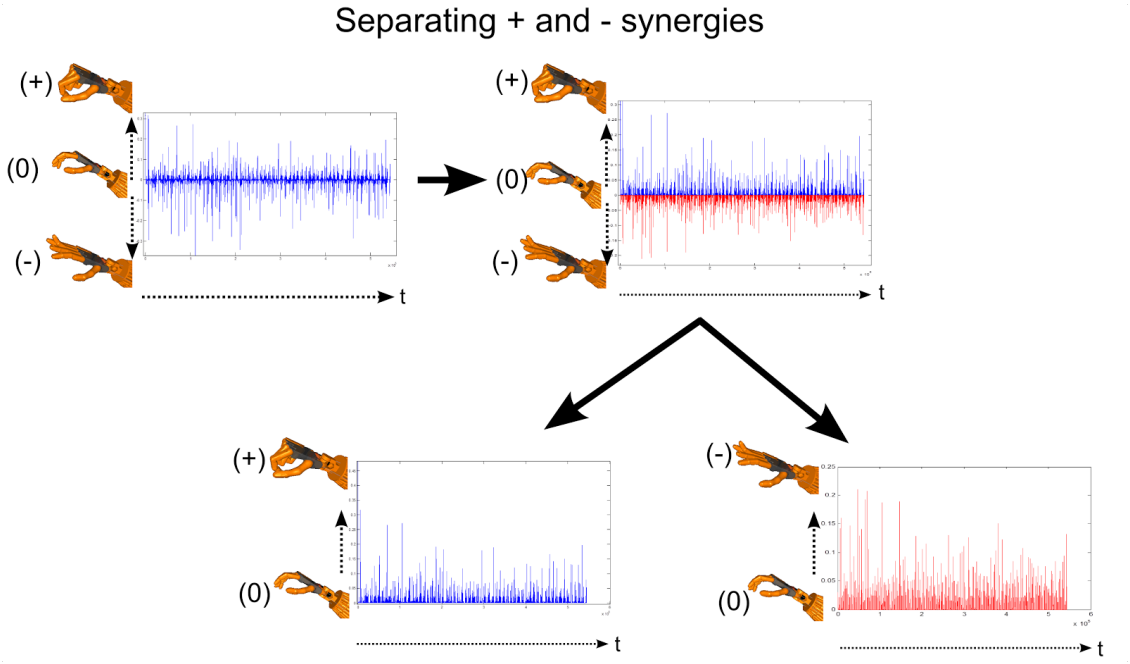

Figure 2.3: Illustration of splitting a centered PCA-based postural component into two non-negative antagonistic pairs. This postural representation approximates non-negative activations of muscle pairs in the hand that pulls hand posture from a neutral centered position.

jected movement time series of non-negative antagonistic muscle pairs, and the estimated spectral power density through time of each captured electrode. The maximum value of the covariance within a ± 150 ms time window where the spectral power density of each electrode-frequency pair was found to highly covary with hand movement component is plotted below as a time-frequency feature of maximum relevance. Figure 2.4 illustrates this mapping for postural component 1, which is the power grasp axis. As can be expected, motor areas above 65 Hz exhibit the maximum relevance to this postural component activation. Note that the relevant time-frequency region extends far above the canonically used frequency of 120 Hz.

Subsequently, these relevance maps are contrasted with each other. Figure 2.8 illustrates and the electrode-frequency pairings of maximum variance is plotted as an anatomical overlay to identify regions and frequencies of interest for movement decoding.

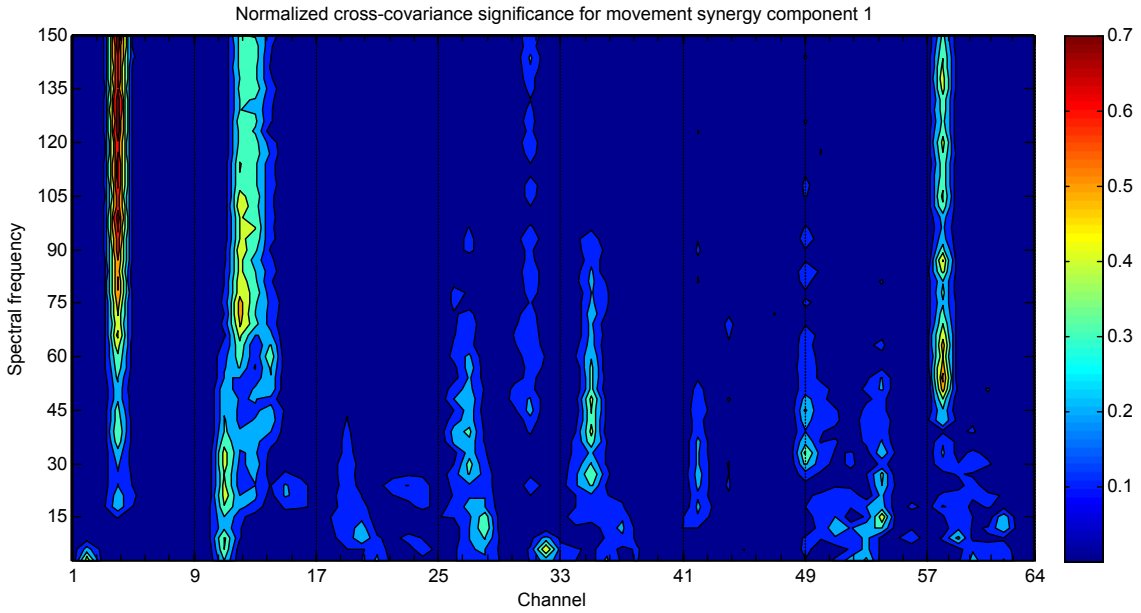

Figure 2.4: A spatial × spectral frequency plot of maximum relevance to power grasp / synergy component 1. Each contour color corresponds to to a maximum cross-covariance value (normalized arbitrary units) between ECoG spectral density and non-negative antagonistic postural component 1 (power grasp) across time.

Fast spectral power estimation

The recorded ECoG data was highpassed at 1 Hz to remove DC offset and common average referenced in the implanted grid, and notched filtered at 60Hz to remove line noise. The gross spectral power in the 70-100 Hz high gamma band, and any frequencies of interest identified through localization mapping associated with motor movement at each point in time is calculated via envelop detection by taking the amplitude of the Hilbert analytic transform of the per-channel time series. Finally, the mean spectral power is calculated for 200ms bins along the time series.

LDA dynamic movement classification

Recorded grasping movements were replayed in two-dimensional space by active dynamic classification of the movement using a linear discriminant analysis classifier. The wide-

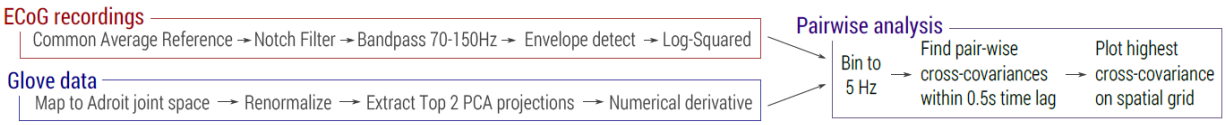

Figure 2.5: Overview of postural grasp mode / movement synergy mapping analysis. ECoG recordings and glove data are both used in pairwise analysis.

band high gamma (70-100Hz) and beta (8-25Hz) log-spectral power of each channel were Z-score converted and used as 128 possible features (2 bands $\times$ 64 channels) to train a linear discriminant analysis classifier with three movement directions in two-dimensional synergy space as labels. Every 200ms, the hand was classified as moving toward one of 8 non-negative antagonistic component directions in space.

The dynamically decoded hand movements were then cross-validated using leave-one-out paradigm where every 200ms time block was evaluated for rest/move and for movement direction. The velocities of these movements were predicted using linear regression. The velocity-time product was then integrated in order to produce a joint position replay of the hand movement timeseries, which was then assessed for accuracy by correlation to the original recording. This overall processing pathway is illustrated in Fig. 2.5.

2.1.3 Results

Variance accounted in the functional synergy space

In agreement with existing literature (Santello, Flanders, and Soechting 1998), we find that on average 75% of the postural variance can be explained by the top two PCA components, and 85% by the top three components. On average, relatively little (<10%) of variance is explained past the 4th component. We find excellent agreement and low between-subject variability in the top synergy space axes for recorded hand movement for the overt hand movement time series motion captured during the object grasping task. In general, the top postural component forms a movement reminiscent of a power grasp, and the second postural

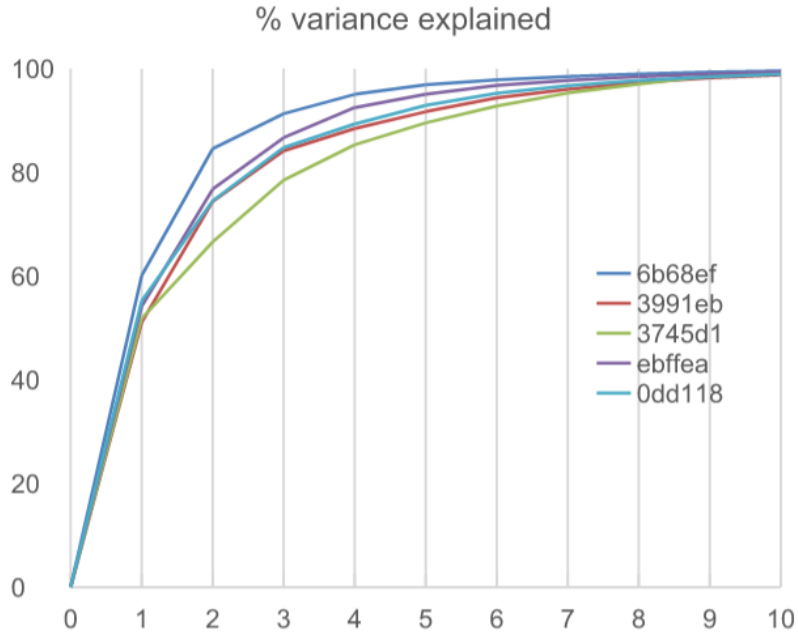

Figure 2.6: Variance accounted for using up to 10 component movement synergy spaces, with inflection point found at 2 components. These two standard PCA components would be split into four non-negative components in the dynamic movement classification.

component a palmar grip. The synergy space in all subjects can achieve a wide variety of grasps in an underactuated control model, including the prototypical power, precision, and palmar grasps, in the coordinate space expanded from the principal component axes.

Spatial localization of synergy component correlates

For each subject, the top cross-covariance based metric reveals the relevant spatial location in the implanted ECoG grid for the sensorimotor area from movement, with no assumption or prior knowledge of the task structure. This type of localization was done in specific bands of interest (70-100Hz, Figure 9), as well as across all available frequencies (Figure 10). The top four to six electrodes are easily localized for each individual subject from the relatively low background of various other areas in the frontal and temporal lobes, as determined by clinical coverage, and are located in the expected somatotoptic hand representation of

the sensorimotor area in all subjects. Within the sensorimotor area, two or more differing movement synergies are also spatially separable by the combination of rankings of electrode relevance, as the overall motif of the dominant electrode within the top relevant electrode varies depending on the type of the movement.

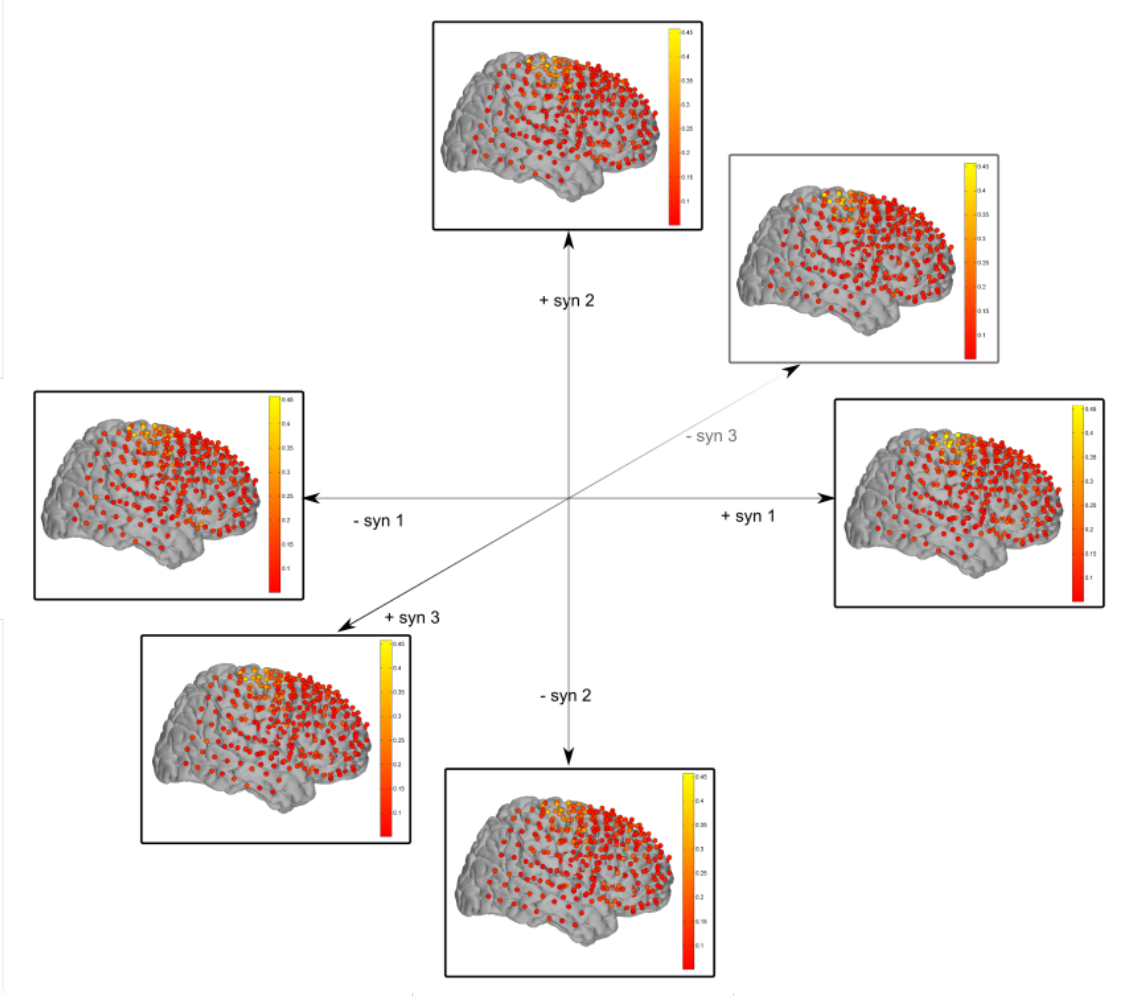

Figure 2.7: Overlaid spatial maps of postural movement components for all subjects, for testing consistent functional somatotopy of postural components across individuals. A consistent somatotopy was not found in this experiment.

The overlay of all subject grids in MNI coordinate space reveals localization to the somatosensory cortex but no immediate patterns in synergy movement functional somatotopy

across differing individuals, as see in Fig. 2.7.

Spatial and frequency localization of ECoG differences between synergistic movements

Of particular interest is the map of distinction in maximum cross-covariances. While the 70-100 Hz segment is highly correlated with overall hand movement, it carries minimal synergy component distinction information, whereas the 100-115Hz and 130-150Hz spectral densities carry the most information about synergy components and are best suited for classification.

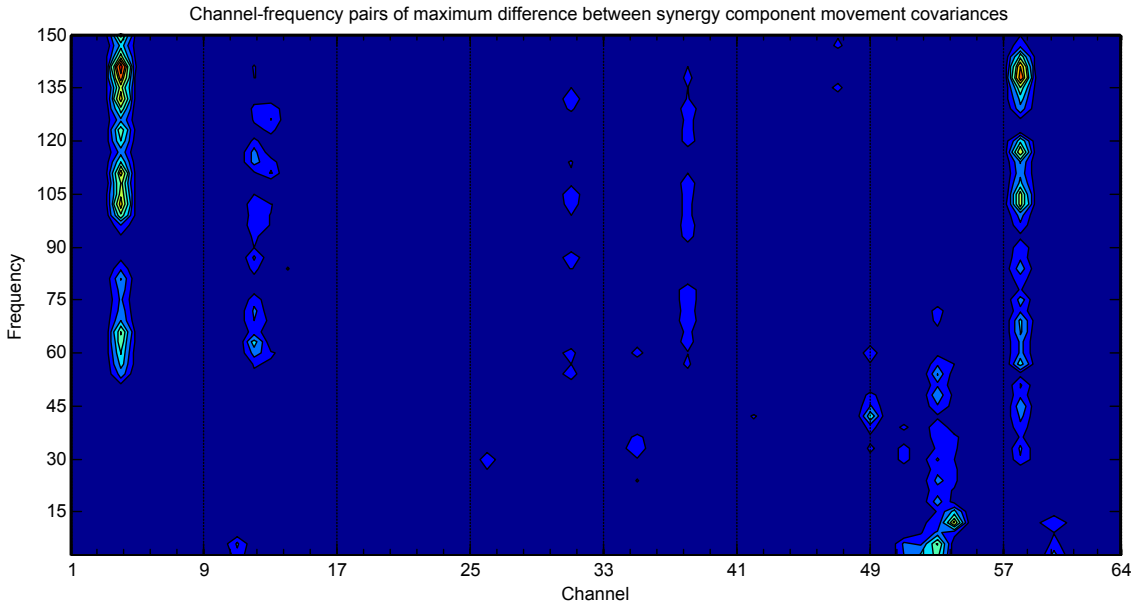

Figure 2.8: Overview of postural grasp mode / movement synergy mapping analysis. ECoG recordings and glove data are both used in pairwise analysis.

Simulated On-line decoding

Utilizing the trained LDA classifier in leave-25% out validation, the move/rest state and the direction of movement is classified for all 200ms blocks and the total accuracy is summarized below for all 5 subjects tested.

Subject	Move/Rest accuracy *(baseline)*	Directional accuracy
6b68ef	85% *(50%)*	66% *(16%)*
3991eb	90% *(50%)*	70% *(16%)*
3745d1	78% *(50%)*	54% *(16%)*
ebffea	87% *(50%)*	45% *(16%)*
0dd118	81% *(50%)*	56% *(16%)*

Table 2.1: LDA decoding accuracy at all 200ms timepoints.

2.1.4 Discussion

Dynamic decoding of ECoG sensorimotor signals

Dynamic hand postural decoding is a novel and powerful method in ECoG-based motor BCI. As it is extremely desirable for rehabilitative devices for sensorimotor disabilities to exhibit continuous volitional control in order to facilitate the free exploration of the living environment with active feedback, it is increasingly important to apply continuous dynamic decoding to the domain of ECoG-based upper limb neuroprosthetics. While existing "task catalog"-based classification BCI has achieved limited success in demonstration, this study demonstrates increasing promise in sufficient extractable information in clinical resolution electrocorticography implants in order to enable a reduced-dimensional model of volitional control for rapid access to the most function given a neuromotor signal source with limited spatial resolution.

While ECoG does not have the spatial resolution of intracortical recordings, its ability to capture large neural populations in aggregate throughout a wide area of the cortical surfaces allows still for the real-time capture of varying type of motor correlates and allows for continuous, real-time feedback control of joint-space representation of hand movements. The possibility of a neuroprosthetic implant incorporating of dynamic feedback is especially crucial as it allows for the possibility of artificial sources of sensation for a full sensorimotor

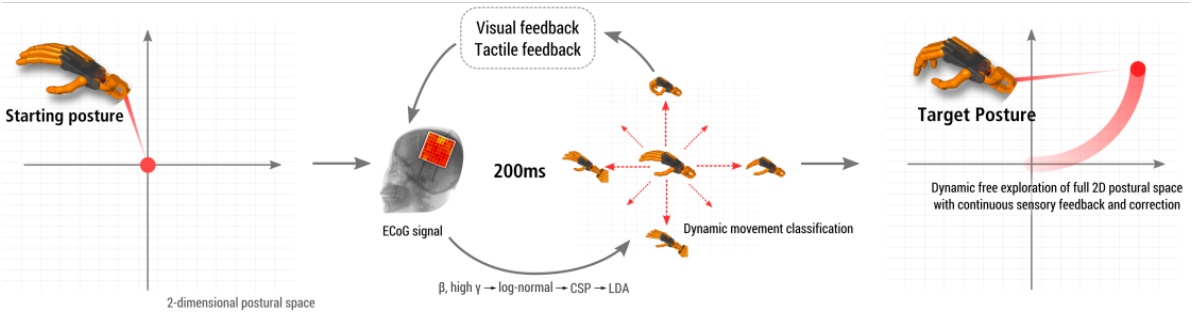

Figure 2.9: Overview of postural grasp mode / movement synergy mapping analysis. ECoG recordings and glove data are both used in pairwise analysis. Unlike previous work, this model allows for active decoding and exploration through 2D kinematic grasp space.

experience, the holy grail of upper-limb neuroprosthetics.

Physiological relevance of PCA-based synergies

Principal component analysis, as it is applied in this study, derives orthonormal principal axes on the relative variance observed in joint positions. As grasping postures of different objects exhibit variability between individuals based on circumstance, habitual motions, hand shape, and hand size, it may be reasonable to expect variability in the joint variance and thereby the principal components. However, this study has found that the between-subject axes have stayed relatively consistent. While it is possible that this demonstrates a methodological bias of PCA as a methodology when applied upon joint angle time series, the degree and extent by which movements projected along these PCA axes covary with sensorimotor ECoG, with variable dominant motifs for different synergy movements, suggests some underlying pattern that is suitable for exploration with dimensionality reduction. Further, in synthetic data of the same technique applied to 10 different postures of the Toronto Rehabilitation [62], we have found that the grasping postures of the principal PCA components also agree with the patterns found in recordings. The overlay of relevance motif locations on a neuroanatomical atlas has not revealed clear signs of somatotopic mapping of PCA synergy movements with any particular region of the hand knob. The implications of this is not cer-

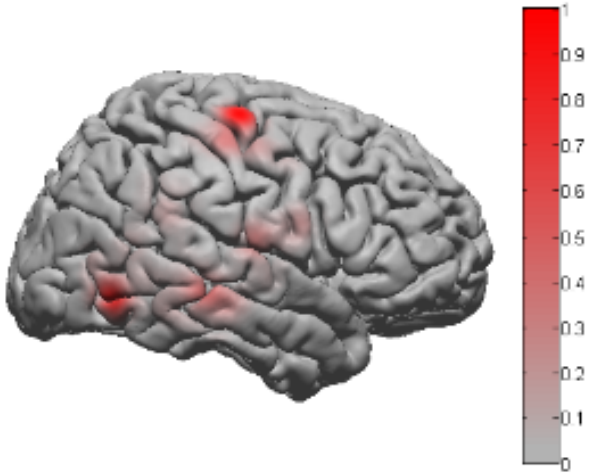

Figure 2.10: Regions of the cortex with a high degree of correlation to directionally-distinguishing high γ signal that can distinguish between differing kinematic grasping modes. In addition to the expected primary motor cortex finding, note the potential involvement of the temporoparietal junction and temporal-occipital junction. Arbitrary units.

tain; it is possible that between-individual variability of motor mapping inherently precludes uniform somatotopic mapping of movements, or that the PCA orthonormal axes are not "biomorphic" coordinate spaces, natural coordinate spaces determined by physiological processes. However, even movement coordinate spaces that are similar to natural physiological coordinate spaces can still lead to rapid gains in function, as even very complex coordinated hand postures can be represented in a relatively low dimensional space.

Both the spatial and frequency distribution of cross-covariance magnitude and variability conveys that useful information above noise threshold regarding hand movements extend far beyond 100 Hz in M1 areas, and that spectral densities of bands above 100 Hz carries the most information capable of separating between synergy components in grasping tasks.

The directional decoding accuracy, at the time resolution of 200ms, is significantly higher than chance. This implies that extractible information of grasp kinematics exists in the high gamma band at short timescales, but their separability at high temporal resolutions

still requires improvement. The overall ability to distinguish motor patterns in this case improves upon individual finger decoding in that coordinated, functional grasping activity is dynamically decoded from the cortex.

2.1.5 Limitations and future work

This study examines the extractible information of coordinate hand movements in the sensorimotor cortex given ECoG grids clinically implanted for preoperative seizure monitoring; as such, compared to similar experiments utilizing long-term implants of high density ECoG or intracortical implants, there was poor control and resolution over the spatial regions of interest potentially carrying the maximum information regarding coordinated movement.

This study is also limited by its short duration, variability in reaching actions and non-joint-position grasping parameters, and the specificity of the motor task. A small catalog of objects was used in the study with relatively few repeated trials, and the external validity of a PCA-based cross-covariance is unclear. There is also an unknown amount of variability in grasping tactic that the subjects applied in each trial. While care was taken to minimize variability in arm positioning and movements and to focus on grasp, this cannot be perfectly controlled for in a clinical environment. The amount of contact forces are also not quantified or controlled, which affect sensorimotor representation of the task.

In order to achieve the eventual goal of closed-loop real-time BCIs in neuromotor-impaired individuals, it is not sufficient to decode positional state but intent. As such, this work builds upon prior work in decoding individual finger movements and instead interprets intended joint movement velocities as a function of ECoG signal. This decoding technique holds promise in the development of future real time dynamic BCIs with dynamic feedback.

2.2 Identify ECoG Relationships to Kinetic Output

This work is done in conjunction with Katie Ly *et al.*, and published as [66]. *Author-specific contributions follows. Adapted in part from [66], ©2018 IEEE. Reprinted in part, with permission from authors.*

Interacting with objects entails kinetic activity; therefore unknown factors concerning kinetic behavior are particularly relevant for the improvement of dexterous neural prosthetics. Spatial representation of kinetic intent, direction, and magnitude would provide insight regarding neural dynamics of kinetic behavior and electrode sensor placement for better signal resolution. In this study, we investigated high gamma ECoG power in human sensorimotor, posterior parietal, and premotor cortices during hand and upper-limb kinetic tasks to evaluate kinetic intent and sustained force magnitude and directional motor output.

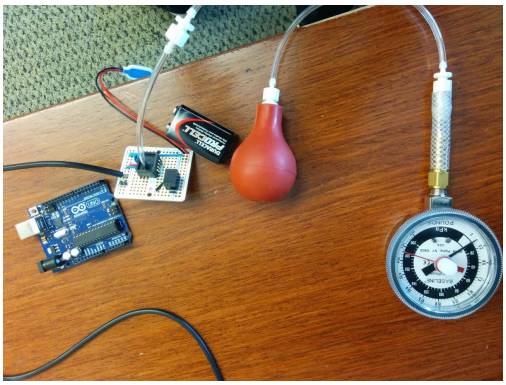

Figure 2.11: Instrumented squeeze-bulb dynamometer used in task in kinetic output task.

2.2.1 Methods

Cortical surface potentials were collected from two volunteering patients undergoing clinically recommended epilepsy monitoring (1 bilateral and 1 right hemisphere) with normal preoperative motor function during directed isometric arm force and power grasp tasks. Prior to testing, participants provided written informed consent through a protocol approved by the Institutional Review Board. All subjects received a preoperative anatomical MRI and implanted with platinum electrode sheets (Ad-Tech, Racine, WA, USA), with 3mm electrode-diameter (2.4mm exposed) set in silastic with 10mm center-to-center distances. An X-ray CT imaging followed to capture electrode placement. A 128-channel Tucker-Davis Technology (Alachua, FL, USA) System 3 RZ5D Neurophysiology Base Processor with associated PZ5

NeuroDigitizer was used to sample the electrodes at 1220.7 Hz.

In one experiment, a 26-year-old right-handed male was implanted with two 2×8 electrode strips in the frontoparietal region and four 1×8 electrode strips in the ventrotemporal and precuneus regions (two strips in each region). He was comfortably positioned in front of a digital display and prompted via visual cues to apply isometric force, using his right hand, in one of 6 orthogonal directions (up, down, left, right, forward, backward) to an affixed AMTI force transducer handle (Watertown, MA, USA). Each trial included a 2-second hold of approximately 15lbs (67N) of force, without force magnitude feedback, with 3 seconds of inter-trial interval. A total of 60 isometric force trials were collected comprising of 10 trials of 6 isometric force directions.

In another experiment, an 8×8 electrode grid along with 1×8 and 1×6 electrode strips (not included in analysis) were implanted in the right hemisphere of a 33 year-old male. The subject was visually prompted to apply a grasping force with contralateral hand on a pneumatic dynamometer (Baseline, White Plains, NY, USA) with visual feedback from a pressure gauge. The subject applied kinetic output in 4 pressure conditions (0, 20, 30, 40kPa) for a total of 24 trials (6 trials per pressure condition) with 5-second hold and 2.5 second inter-trial interval.

Using Statistical Parametric Mapping (`http://www.fil.ion.ucl.ac.uk/spm`). pre-operative MRI was co-registered with postoperative CT. Cortical surfaces was reconstructed with FreeSurfer (http://freesurfer.net) and custom mapping and projection code was implemented in MATLAB (Natick, MA, USA) [16]. In the isometric task, data quality was visually inspected in the two 2×8 grids in the frontoparietal hemisphere. 1 channel in the contralateral left grid and 2 in the right were rejected due to high level of artifacts and low impedance. For both experiments, artifacts were removed from raw ECoG time series and filtered with a 4th order Butterworth band pass filter (70–110 Hz) to extract γ-band activity. Power spectrum envelopes were then extracted by taking the Hilbert transform. Dimensionality reduction was performed using principal component analysis (PCA) to extract the top 12 principal components (PCs). Recorded force transducer voltages were converted to force

(lbs) using manufacturer sensitivity calibration data and Cartesian forces were transformed to spherical coordinates to obtain force direction and magnitude. Dynamometer force data was converted into pressure (kPa) via the manufacturer's conversion equation. All filtered and processed high gamma time series and kinetic data were then binned to 50ms intervals.

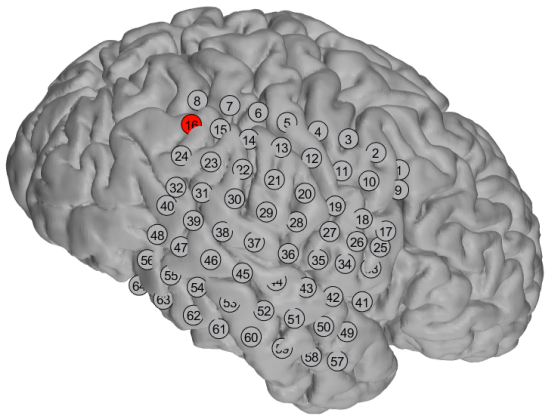

Figure 2.12: Electrode placement for dynamometer hand grasping task on right hemisphere. Linear relationship between high gamma power and force magnitude was found in channel 16 which was located in the posterior parietal cortex.

In the isometric kinetic task, force magnitude was classified in 3 conditions (prompted rest, low, and high). Force classes were defined by removing passive resting time points and using 33.3th and 66.7th percentile values to discriminant data into respective force magnitude classes. In the grasping task, dynamometer force data was only recorded in one participant thus time series of the cue was used to determine grasping related cortical activity. High gamma activity analysis classified with either force data or cued data yielded similar results, therefore cue time series was used to classify available pressure conditions for consistency. Correlation analysis between spectral power and absolute force time series across all ECoG channels were performed on each dataset.

Binned gamma potentials were transformed using principle component analysis (PCA), using top 12 PCs. Top 12 PCs accounted for 72% variance in isometric task, and 77% and 95% variability in dynamometer experiment and were used to train Quadratic Discriminant Analysis (QDA) with 5-fold cross validation to predict force class.

Kinetic directions of active arm force output time points were classified into 6 orthogonal directions: up, down, left, right, forward, and backward, as determined by the output of the force transducer. Any time points containing accidental movements, deviating from the orthogonal directions by more than 15° were excluded from the analysis. The QDA model was also used to determine classification accuracy. The model was trained using the top 12 PCs of binned high gamma spectral power with synchronized binned force direction classes using 5-fold cross validation.

2.2.2 Results

Utilizing the above experimental setup, we were able to find a linear relationship between kinetic output of grasp force and high-γ spectral power, in posterior parietal cortex structures (Fig. 2.12). Further, in the experimental setup with kinetic arm output forces, we were able to find precuneus as a dominant contributor of directional distinguishing information in a PCA-QDA classifier (Fig. 2.13).

2.3 Implementing Kinematic Components for Cortical Stimulation Feedback

This work is done in conjunction with Jeneva Cronin *et al.*, and published as [67]. *Author-specific contributions follows. Adapted in part from [67], ©2016 IEEE. Reprinted in part, with permission from authors.*

Direct cortical stimulation (DCS) may provide a method by which an approximation of tactile feedback may be directly encoded and perceived by the brain in future neuroprosthetics. It is however unclear whether or not patients fitted with cortical stimulation neuroprosthetics can perceive and use the direct stimulation signals in order to modulate their behavior in motor tasks. Grasp aperture, which is a measure of the approximate di-

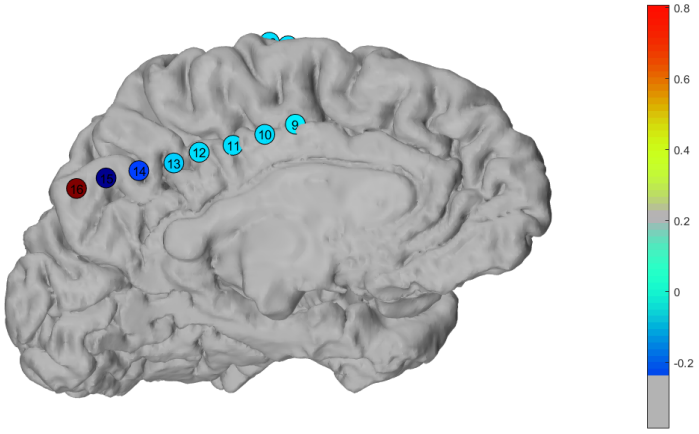

Figure 2.13: Electrode placement for kinetic force output. Inter-hemispheric view of left hemisphere showing channels in the precuneous as a dominant contributor for principal components contributing to kinetic force output direction classification.

ameter of the kinematic posture of the hand in a grasping position, can provide an easily measurable, continuously-modulatable motor task by which to evaluate the efficacy of DCS feedback.

Subjects were hospitalized for clinical monitoring of epilepsy with implanted electrocorticography grids (see, e.g., Leuthardt, et al. [68]). Clinicians determined their electrode locations strictly by clinical needs without consideration for research. We conducted stimulation studies after subjects were back on their anti-epileptic medications (AEDs). This experiment was approved by the Institutional Review Board of the University of Washington, and all subjects gave written, informed consent.

Three subjects wore a 22 degree-of-freedom dataglove (Cyberglove II, CyberGlove Systems, San Jose, CA) to measure the position of their hand, which we sampled every 50 ms with a custom MATLAB script. To begin the task, subjects opened and closed their hand (in a palmar grasp, as if grasping a cylindrical object) with the dataglove for approximately 20 seconds. We took the first vector of the singular value decomposition of these movements

as the primary trajectory of aperture motion. During the task, every new glove sample was projected onto the primary trajectory, and the magnitude of the resulting vector was taken as the non-normalized aperture value. We then calculated the normalized aperture value ranging from 0 to 1 based on the subject's minimum (closed) and maximum (open) hand positions. We instructed subjects that they would be asked to open and close their hand to find and follow a target aperture path. Cortical electrical stimulation using the waveforms described above provided feedback to the subjects on their current state.

The first vector of the singular value decomposition was demonstrated to be an effective way of quickly calibrating for the aperture representation of grasp in each patient. As all grasp kinematics are projected along the this first vector, a quick method of measuring palmar/power grasp aperture can be derived in under 1 minute, which is a significant improvement over a full calibrated mapping with a high degree of requirement to match a large series of postures in order to find joint limits.

This methodology concurs with kinematic mapping in Fig. 2.2 and was effective in facilitating a feedback task with subject performance well above chance, with a best task performance in a sensory feedback task of R^2 of 0.93 and accuracy of 76%.

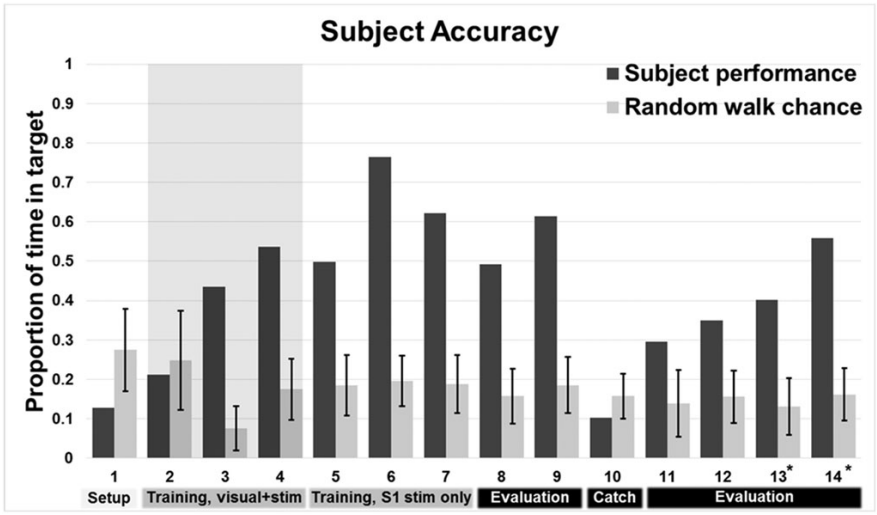

Figure 2.14: Subject performance accuracy as evaluated by "accuracy", which is % of time within the a designated dynamic movement envelope. Note the statistically significant loss of accuracy during a catch trial, signifying the importance of DCS sensory feedback to task performance.

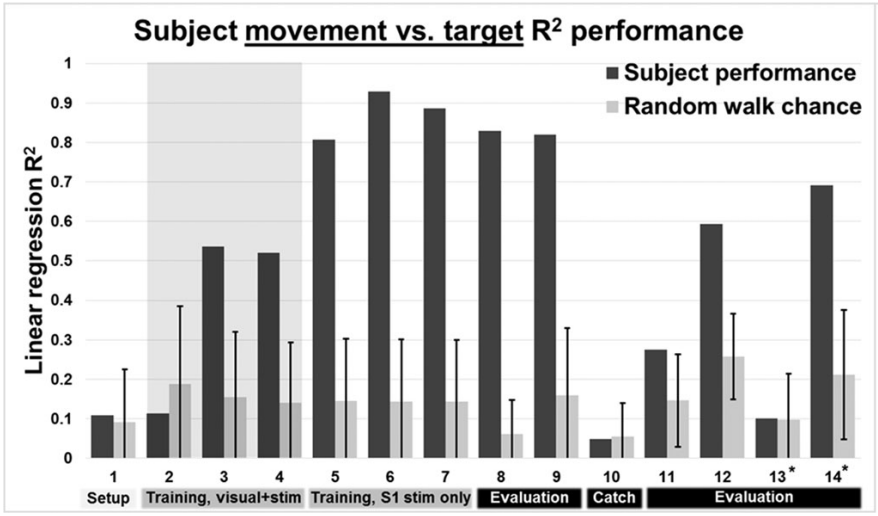

Figure 2.15: Similar to 2.14, with subject performance accuracy as evaluated by R^2, which represents the goodness-of-fit of subject movement with respect to a dynamic movement target median track.

Chapter 3

PRE-MOVEMENT FEATURES OF LIMB FORCE DIRECTION WITH REDUCED-RANK CLUSTERED MARKOV MODELS

Neural correlates of movement planning onset and direction may be present in human electrocorticography in the signal dynamics of both motor and non-motor cortical regions. We use a three-stage model of jPCA reduced-rank hidden Markov model (jPCA-RR-HMM), regularized shrunken-centroid discriminant analysis (RDA), and LASSO regression to extract direction-sensitive planning information and movement onset in an upper-limb 3D isometric force task in a human subject. This mode achieves a relatively high true positive force-onset prediction rate of 60% within 250ms, and an above-chance 36% accuracy (17% chance) in predicting one of six planned 3D directions of isometric force using pre-movement signals. We also find direction-distinguishing information up to 400ms before force onset in the pre-movement signals, captured by electrodes placed over the limb-ipsilateral dorsal premotor regions. This approach can contribute to more accurate decoding of higher-level movement goals, at earlier timescales, and inform sensor placement. Our results also contribute to further understanding of the spatiotemporal features of human motor planning.

3.1 Introduction

Decoding human arm movement has been a major goal of motor brain-computer interfaces (BCIs) for the development upper-limb neuroprostheses. Many previous decoding approaches have related recorded sensorimotor signals with specific virtual or robotic movements [44, 70, 51], allowing a potential BCI to reconstruct intended movements from a combination of basic signal changes. For example, primary motor cortex signals during individual

finger movements could be combined to reconstruct multi-axis virtual cursor movements [14, 42], or pinch or grasp movements [46, 48, 71]. Alternatively, more abstract representations of movements, or movement plans, may be present in recorded brain signals prior to the onset of movement. The presence of these signals may especially be true in areas outside of the sensorimotor cortex. For instance, studies in non-human primates and human neuroimaging have established that, during an upper-extremity movement in a reach task [72, 73, 74], the parietal and premotor cortices play a key role in the representation of target trajectories and executing planned movements in the desired spatial coordinates. An effective control signal for a BCI must maximize the information available, including preparation prior to the onset of movement. Patients with indwelling electrocorticography (ECoG) electrodes implanted for medically intractable epilepsy provide recordings with centimeter resolution combined with millisecond sampling over a large brain region. These signals offer an opportunity to detect correlates of the entire movement preparation and execution process. Previous work have demonstrated the capacity of ECoG signals to resolve the timing and interaction between regions during finger movements [71], upper-limb movements [44, 70], as well as premotor responses that precede the sensory and motor cortex activation up to 100ms in advance [75]. One previous work has also shown some success in detecting ECoG representations of onset and direction of hand-arm movements [76] However, the temporal and spatial distributions of the recorded signal in motor preparatory regions are not well-established in human ECoG. It is yet unclear which non-motor regions contain ECoG signals with direction-distinguishing preparatory information, whether these signals are localized to just the contralateral hemisphere or both hemispheres, and how they are localized in time. It is also unknown whether correlates of preparatory activity are limited to reach trajectories, or also can generalize to other directional tasks such as isometric force application towards planned directions. These unknown factors are particularly relevant to the engineering of BCI, as signals conveying information about the planning of a movement may allow for better resolution of differing task goals, inform locations for sensor placement, and enable decoding of these goals earlier than signals in the sensorimotor cortex. In this work, we investigated

the recorded ECoG activities of a patient with fortuitous bilateral implantation of electrodes in the parietal and arm-associated sensorimotor cortices. The patient performed a right arm isometric force task toward designated directions. We constructed a three-stage model to examine the localization and timing of direction-discriminable information, allowing for the parallel prediction of isometric force onset and direction.

3.2 Methods

3.2.1 Experimental Task and Data Acquisition

The patient is a 26-year-old right-handed male with intractable seizures thought to be related to a medial parietal lesion; invasive monitoring of bilateral parietal regions was recommended. The subject received pre-operative anatomical MRI, and was implanted with two frontoparietal 2×8 platinum electrode grids and two 1×8 strips (Ad-Tech, Racine, WA, USA), with 3mm electrode-diameters embedded in silastic with center-to-center distances of 10mm. Subsequently, X-ray CT imaging captured the location of the electrodes. These electrodes were sampled at 1220.7 Hz on a 128-channel Tucker-Davis Technology (Alachua, FL, USA) System 3 RZ5D Neurophysiology Base Processor with associated PZ5 NeuroDigitizer. The subject had normal motor function pre-operatively and throughout the experiments and inpatient stay. The patient gave written, informed consent through a protocol approved by the University of Washington Institutional Review Board.

The patient was comfortably positioned in front of one screen during the task, and was visually cued to apply isometric force in one of 6 directions (up, down, left, right, forward, back) to an affixed AMTI force transducer handle (Watertown, MA, USA) held in the right hand (Fig. 3.1). Each trial consisted of a hold with approximately 15 lbs (67 N) of force and 2 seconds in duration, with an inter-trial interval of 3 seconds. 10 trials of each of 6 directions were recorded for a total of 60 isometric force trials.

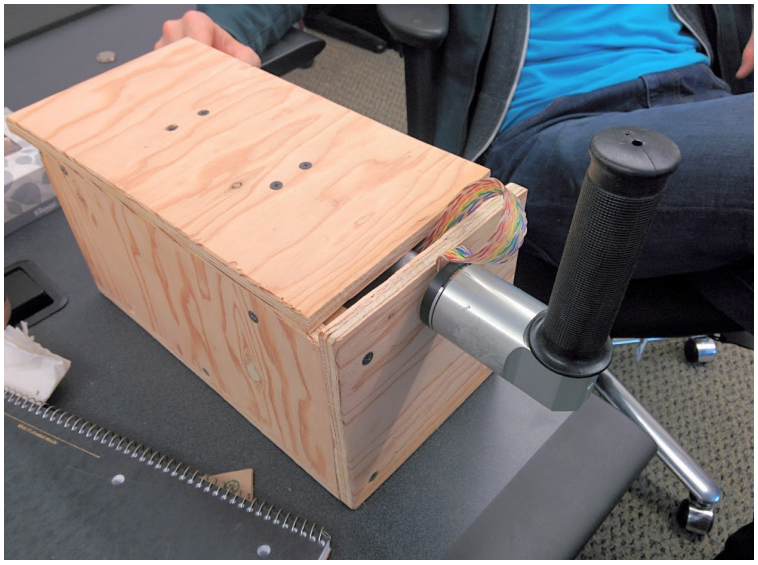

Figure 3.1: Image of an instrumented assisted walker load cell from AMTI used in this experimental data acquisition.

3.2.2 Data Preprocessing and Feature Extraction

Pre-operative MRI was co-registered with postoperative CT using Statistical Parametric Mapping (`http://www.fil.ion.ucl.ac.uk/spm`), with the pial surface reconstructed with FreeSurfer (http://freesurfer.net) and custom mapping and projection code [77] implemented in MATLAB (Natick, MA, USA). The two frontoparietal hemisphere 2×8 grid recordings were visually inspected for data quality, and channels with high level of artifacts and low impedance were rejected (1 in the contralateral L grid and 2 in R). The remaining 29 recorded channels were filtered with a common average reference filter

$$s_i' = s_i J^{-1} \sum_j s_j \tag{3.1}$$

for J non-rejected channels within each separate lateral grid. The filtered signals were then analyzed for time-frequency content by continuous wavelet transform with the non-analytic Morlet wavelet defined by

$$\Psi(s\omega) = \pi^{-1/4} \exp(\frac{-(s\omega - \omega_0)^2}{2}) \tag{3.2}$$

where $\omega_0 = 6$ and s reflects log scaling factors to obtain $1/8$-octave resolution across pseudo-frequencies $2 - 200Hz$. We used the absolute magnitude of the wavelet coefficient time series at each scaling, and also extracted the lowpassed ECoG local motor potential (LMP) for each channel as outlined in [78] as an additional time series. All time series were binned by 50ms and normalized to unit variance. Recorded force transducer voltages were converted to force using manufacturer sensitivity calibration data; Cartesian forces were transformed to spherical coordinates to obtain task force direction and magnitude. Subsequently, the initiation and end of recorded isometric force in each trial were carefully hand-labeled (examples shown with dotted force traces and vertical onset lines in 3.4).

3.2.3 Pre-Movement Classification of Force Direction

jPCA-RR-HMM analysis: We constructed a reduced-rank hidden Markov model (RR-HMM) [79] from the normalized binned time series using jPCA. This is a specialized dimensionality reduction method designed to find orthonormal bases that also exhibit a rotational structure by computing circularity metrics of the subspace. A circular repeating structure in the reduced rank phase space is used in order to investigate dynamics that rhythmically repeating over time in the source neural data. This implies a greater probability that those reduced rank subspaces contain task-relevant or goal-specific structure, as the task structure is repetitive [80]. To find these repeating mean trajectory templates, filtered time series were split into 2-second segments, aligned to the initiation of movement, reflecting a time period of $[-1000ms \ldots + 1000ms]$ for each movement trial.

The mean $\bar{x}$ of the high-dimensional time series

$$x_{w,t,c} \mid t = [-1000, -950, \ldots 0, \ldots + 1000] \tag{3.3}$$

for each channel $c \times$ frequency w pair:

$$\bar{x} = \frac{1}{|t|} \sum_t x_{w,t,c} \tag{3.4}$$

were obtained for each of the 6 movement direction conditions $d = [1 \ldots 6]$, to form mean trajectories for each template type. jPCA was used on these mean timeseries to obtain a

top 10 set of jPC coefficients that describe a 10-dimensional space to maximize rotational dynamics in these mean ECoG signal trajectories. The original trial segments $x_{w,t,c,d} \mid t = [-1000 \ldots + 1000]$ were then projected through these jPCs, such that each trial segment is now reduced to a 10-D space:

$$x'_{[jPC_{1,2}],t,d} \mid t = [-1000 \ldots + 1000] \tag{3.5}$$

All time points were then labeled as belonging to one of 12 clusters in phase space agnostic to condition, using unsupervised hierarchical clustering of all x' time points with Ward's method, which recursively locates clusters that minimize within-cluster distance variance in the dimensionally-reduced Euclidean space. This method generated a list of observed states $s_{t,d} \mid t = [-1000ms \ldots + 1000ms]$, where all observed s are categorical class labels, $s = [1 \ldots 12]$, and d is one of six directions of movement.

The pre-movement cluster-time-series were then isolated and used as the sole training data to construct the HMM. Cluster labels immediately preceding movement $s_{t,d} \mid t = [-500ms \ldots 0ms]$ were grouped by movement direction condition, and used as observed sequences to train six hidden Markov models H_d, one for each force movement direction with $d = [1 \ldots 6]$. The Baum-Welch algorithm was used with 12 observed states and 8 hidden states to train each H_d. Direction predictions were made with leave-one-out validation, where each HMM generated from training $s_{t,d}$ was used to calculate the posterior state probability of observing the sequences in the testing $s_{t,d}$. The direction associated with the H_d giving the highest posterior probability (smallest negative log-probability) was used as the classified direction.

Regularized discriminant analysis

The normalized, binned time series were split into 1-second chunks aligned to the initiation of movement segments, reflecting a time period of $[-1000ms \ldots 0ms]$ for each trial, with the start corresponding to 1 second before movement initiation. Each feature $x_{w,t,c}$ at wavelet scale w, timepoint t, and channel c is used as a feature for the training of a multiclass regu-

larized discriminant analysis model with 10-fold validation, where the posterior probability that observation $x \in k$ follows

$$\hat{P}(k|x) = \frac{P(x|k)P(k)}{P(x)} \tag{3.6}$$

$$= \frac{\frac{1}{(2\pi|\sum_k|)^{1/2}} \exp\left(-\frac{1}{2}(x-\mu_k)^T \sum_k^{-1}(x-\mu_k)\right) P(k)}{P(x)} \tag{3.7}$$

Shrunken centroids regularization as described in [81] attempts to reduce overfitting bias by (a) introducing a modified covariance matrix to stabilize the cross-validated sample covariance Σ and (b) applying a threshold to a modified correlation matrix to prune down the number of useful predictors, as described by

$$\tilde{\Sigma} = (1-\gamma)\Sigma + \gamma D \tag{3.8}$$

$$(x-\mu_0)^T \tilde{\Sigma}^{-1}(\mu_k - \mu_0) = \left[(x-\mu)^T D^{-1/2}\right]\left[\tilde{C}^{-1} D^{-1/2}(\mu_k - \mu_0)\right] \tag{3.9}$$

$$D = \text{diag}\left(\hat{X}^T \hat{X}\right) \tag{3.10}$$

$$\tilde{C} = (1-\gamma)C + \gamma I \tag{3.11}$$

$$\delta \leq \tilde{C}^{-1} D^{-1/2}(\mu_k - \mu_0) \tag{3.12}$$

This is accomplished by iteratively searching through parameters γ and δ, where γ modifies the sample covariance matrix Σ, and δ thresholds the correlation matrix C and reduces the number of predictors by thresholding them from the posterior probability evaluation [81].

3.2.4 Movement Onset and Force Magnitude Prediction

The normalized binned time series was fit to the magnitude of the force using least absolute shrinkage and selection operator (Lasso) regression [82]. Two-fold validation was used wherein the whole time series of the each half of the recorded movement session $r_{w,c}$, with channel $\times$ frequency wavelet coefficients through time was used to fit linear regression coef-

ficients β where, the predicted values through time $\hat{y}_t$:

$$\hat{y}t = \beta_{w,c,t} r_{w,c,t} + \beta_0 \tag{3.13}$$

This generates $\beta_{w,c,t}$ as a function of a regularization parameter λ, which thresholds the number of nonzero β coefficients. λ was chosen such that the mean-squared-error is the lowest in validation, which resulted in 132 nonzero β coefficients, which were used to predict the forces in the other half of the recorded session. The predicted force time series $\hat{y}_t$ were then smoothed using a 1st-order, 2 Hz, -10dB Butterworth lowpass filter and numerically differentiated to obtain $\frac{d\hat{y}_t}{dt}$. Peak analysis was used to find the local maxima of $\frac{d\hat{y}_t}{dt}$ using a fixed threshold, and the local maxima points represent potential times of force onset.

3.3 Results

3.3.1 Force Direction Classification Using jPCA-RR-HMM

An average HMM classification accuracy of 35.6% was obtained using pre-movement clustered timepoints 500ms prior to the onset of movement. Accuracies were computed using leave-one-out cross-validation between 6 force application directions using jPCA-projected, hierarchically clustered pre-movement ECoG. This performance is significantly higher than chance of 17%. Figure 1 shows the confusion matrix of classification in the 6 directions, where the main diagonal shows the correct classifications. Five of six directions showed accuracies above chance, with the most accurate direction being isometric movement back toward the torso, which also had very low false-prediction rates.

3.3.2 Time-Space Localization of Directional Information

In a second analysis, we used regularized discriminant analysis directly on the wavelet features of recorded pre-movement ECoG signals to obtain a cross-validated directional classification accuracy of 27%. While this is not as high as the outcome obtained with the jPCA-RR-HMM analysis, RDA regularization and shrinkage operates on the original feature space,

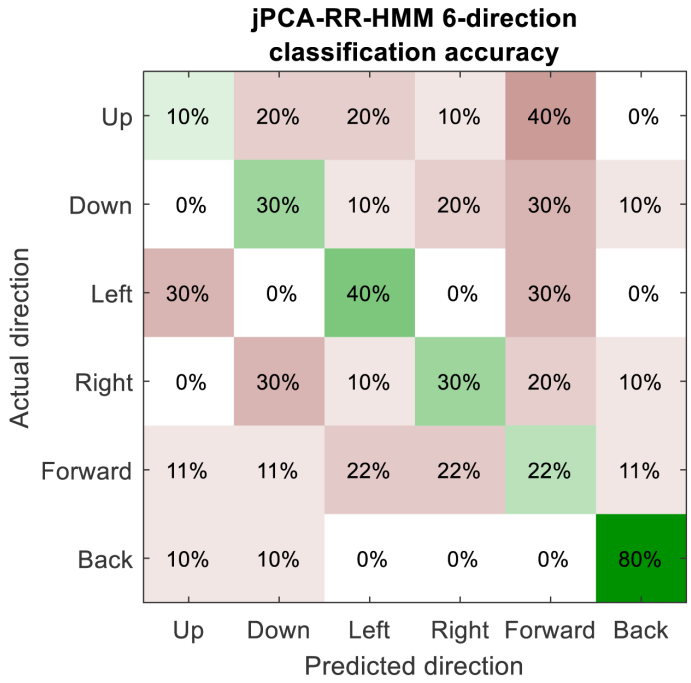

Figure 3.2: Confusion matrix of the model classification accuracies using jPCA-RR-HMM, in 59 valid isometric force application trials in 6 directions using pre-movement ECoG recordings. Bottom axis is predicted direction, left axis is actual direction. Main diagonal indicate correct prediction rates.

and the remaining 27 features included in computing the posterior class probability must exceed the regularization threshold set by δ as outlined in equation 3.12. These remaining wavelet coefficient features demonstrably contain cross-validated directionally-discriminable information, and are localized in time and space. Interestingly, the spatiotemporal distribution of these features as shown in Fig. 3.3 reveal that the earliest information about movement is present in channel 26 (dorsal premotor cortex), then passes on to channel 17, and finally to channel 5 (primary motor cortex).

3.3.3 Lasso Regression Onset and Force Prediction Results

Cross-validated force predictions agree with overall force magnitude ($R2 = 0.42$), but a strong predictive relationship between peak force magnitude and ECoG signals magnitude in this

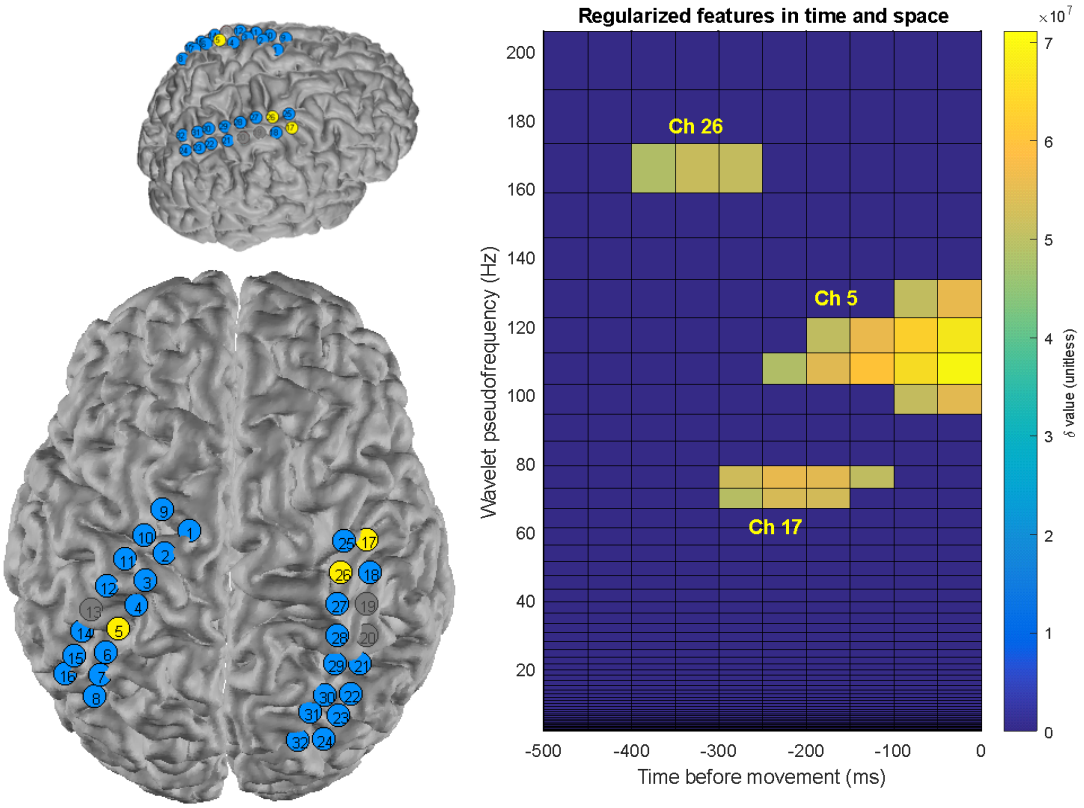

Figure 3.3: Left: Blue = recorded electrodes; Yellow = recorded electrodes corresponding to regularized features in Right plot; Gray = rejected for artifacts. Right: Time-space plot of salient features from regularization. Each block refers to one feature, most salient (high δ) features in yellow.

task was not found. However, the smoothed predicted force time-series can be numerically derived to obtain an accurate assessment of force onset, predicting onset to within 250ms at a 60% accuracy and within 500ms at an 80% accuracy. The false positive predictive rate was 22%.

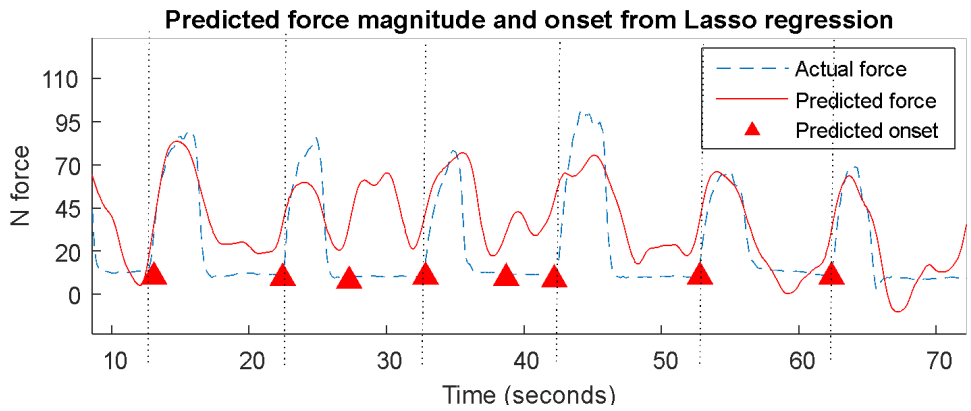

Figure 3.4: Force and onset timing predictions from Lasso regression. Triangles: predicted force onset; dotted vertical lines: actual onset.

3.4 Discussion

3.4.1 Direction-Discriminating Dynamics

We showed that the combination of dimensionality reduction and HMM allowed for RR-HMM states to capture complex multidimensional dynamics in a relatively small number of observed states. The performance of this technique suggests that the dynamics between ECoG timepoints during movement preparatory behavior may carry useful task-relevant information. Though the predictive performance of this technique is not sufficient alone to drive brain-computer interfaces, it may be used in combination with techniques such as Kalman filters that can benefit from earlier probability updates to improve the inference of user intent.

3.4.2 Spatiotemporal Feature Localization

We found that wavelet-based spectral characteristics of ECoG recordings can discriminate between different directions of isometric arm movements significantly better than chance in a regularized discriminant analysis, despite the overlap between the recruited muscle groups and the isometric task. We find that signals carrying direction-discriminatory information

occurred over the ipsilateral premotor cortex up to 400ms before the onset of detected force, in contrast to the signals from the contralateral sensorimotor cortex which showed the strongest discrimination ability starting roughly 100-150msec prior to movement onset (Fig. 3.3). The timing of the information in ipsilateral changes is particular interesting in potentially offering a technique to screen for neural processes spanning multiple cortical regions, and may give hints to the possible timing of distributed trajectory planning processes.

3.4.3 Differences Between Movement Trajectory and Magnitude

While the ECoG signal can be used to both decode direction and force onset in parallel, we found in this dataset that high-performing regression features in predicting force changes do not also perform well in discriminating between directions, potentially suggesting separate usable ECoG signatures for motor execution and planning.

3.4.4 Future Considerations

Further work is necessary to determine whether these particular correlates of movement planning generalize across tasks to other types of upper-limb movements, or generalizes to other measures of force application such as non-task muscle contraction. We also wish to examine the possibility of learning effects with repeated practice.

Chapter 4

IDENTIFYING MENTAL VISUALIZATION OF GRASP PRESHAPING WITH STATE SPACE SHAPE-SIMILARITY METHODS

Identification of intended movement type and movement phase of hand grasp shaping are critical features for the control of volitional neuroprosthetics. We demonstrate that neural dynamics during visually-guided imagined grasp shaping can encode intended movement. We apply Procrustes analysis and LASSO regression to achieve 72% accuracy (chance = 25%) in distinguishing between visually-guided imagined grasp trajectories. Further, we can predict the stage of grasp shaping in the form of elapsed time from start of trial ($R^2 = 0.4$). Our approach contributes to more accurate single-trial decoding of higher-level movement goals and the phase of grasping movements in individuals not trained with brain-computer interfaces. We also find that the overall time-varying trajectory structure of imagined movements tend to be consistent within individuals, and that transient trajectory deviations within trials return to the task-dependent trajectory mean. These overall findings may contribute to the further understanding of the cortical dynamics of human motor imagery.

4.1 Introduction

The ability to translate the cortical activity of imagined motor movements into usable motor output is a crucial step in the development of volitional neuroprosthetics [14, 32, 31]. Electrocorticography-based brain-computer interfaces have previously demonstrated promise in reconstructing overt reach-to-grasp movements [38, 49, 50, 53, 84, 46], as well as to control brain-computer interface tasks both with and without overt movement [42, 39, 85, 86, 87].

However, these previous decoding approaches are limited by their attempts to find the neural direct correlates of overt movement performed in motor-intact individuals, or by their reliance upon an extensive BCI training process through which subjects gradually learn to modulate task-specific cortical activity with specific abstract feedback such as center-out cursor movements. While cortical spectral differences from rest related to motor imagery can be observed in the sensorimotor cortex of untrained BCI-naïve individuals, they are reported to be substantially weaker in magnitude [87], and subsequently less successfully suited as features for real-time movement decoding, prior to protracted BCI feedback training.

However, while direct spectral power changes associated with movement imagery may be small in magnitude in the primary motor cortex, the overall time-varying dynamics of the cortical signal from both motor and non-motor regions may still bear valuable information with regards to motor planning and intent. Recent investigations in neural populational dynamics during reaching movements reveals that even noisy single-trial dynamics of neural populations can provide accurate state estimations given the correct dynamical model [80, 88]. These findings signify that time-varying neural trajectories, when projected into a subspace that maximizes output-relevant dimensions, can extract task-specific movements even when mixed within signals arising from task-irrelevant processes or noise. A dynamical model incorporating broad anatomical regions to reconstruct motor imagery is also particularly relevant in light of previous work establishing that parietal and premotor cortices play a key role in the representation of reach movements [70, 73, 74]. Patients with ECoG electrodes implanted for medically intractable epilepsy provide recordings over a large brain region, providing the spatial coverage that may be necessary for full reconstruction of the underlying motor imagery dynamics, which can overcome some generalization limitations in prior studies due to limited anatomic scope. In this work, we investigated ECoG recordings in three patients with implanted electrode grids. The patients performed overt and imagined motor movements synchronous to visual observation of an animated hand. Using a dynamical model based on Procrustes analysis, we examined the movement type and timing of imaginary movements for the prediction of grasp shaping and timing, achieving high

classification accuracy with only dozens of trials in BCI-naïve individuals.

4.2 Methods

4.2.1 Experimental Task and Data Acquisition

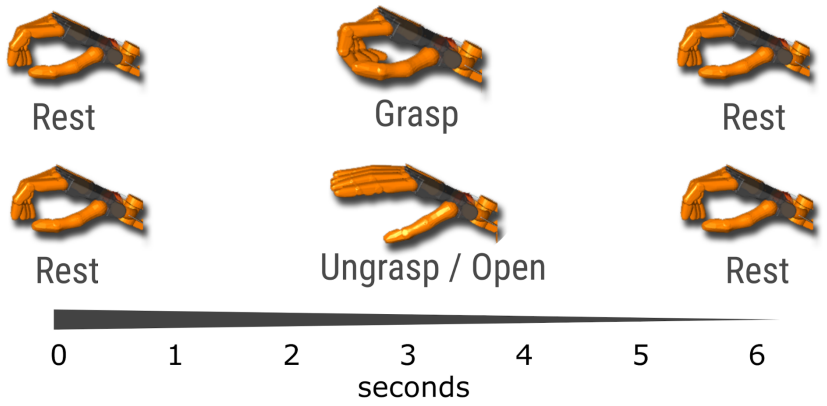

Figure 4.1: Two of four example grasp shaping trial visual stimuli shown: Grasp and Ungrasp. Not shown: Pinch, Unpinch.

Three patients (ages: 13-33; 1 female, 2 male; 2 left hemisphere, 1 right) with normal motor function volunteered for this study during clinically recommended invasive monitoring of seizure-related cortical regions, with written, informed consent through a protocol approved by the Institutional Review Board. All subjects subject received a pre-operative anatomical MRI, and was implanted with an 8×8 platinum electrode grid (Ad-Tech, Racine, WA, USA), along with 1×8 and 1×6 electrode strips (excluded from this analysis). All electrode grids and strips consist of 3mm diameter platinum discs, set in silastic with center-to-center distances of 10mm. Subsequently, X-ray CT imaging captured the location of the electrodes. These electrodes were sampled at 1220.7 Hz on a 128-channel Tucker-Davis Technology (Alachua, FL, USA) System 3 RZ5D Neurophysiology Base Processor with associated PZ5 NeuroDigitizer.

The patients were comfortably positioned in front of one screen during the task. The

screen displayed two separate videos of an animated robotic hand [89] with four different smooth movements, consisting of two pairs of kinematically opposing movements: a power-grasping movement (grasp), a spherical-open movement (ungrasp), a palmar pinch movement (pinch), and an claw-open movement (unpinch). One of these movement pairs (grasp-ungrasp) are shown in Fig. 4.1.

Each of these smooth movements began with a neutral pose (0s), proceeded to the designated pose (3s), and returned to a neutral pose (3s). The patients carried out the poses using the hand contralateral to their implant, regardless of hand dominance. Patients were visually cued to alternately follow with their own hand, or with motor imagery only. In the imagined movement condition, patients were instructed also to imagine feeling the sensations of the movement animation as they would with overt movement. Each animation proceeded for 6s per trial with a 2s inter-trial intervals. Each patient performed 20 to 70 movement trials.

4.2.2 Data Preprocessing and Feature Extraction

The pre-operative anatomical MRI was co-registered with the postoperative ECoG CT using Statistical Parametric Mapping (`www.fil.ion.ucl.ac.uk/spm`), with cortical surfaces reconstructed with FreeSurfer (freesurfer.net) and custom mapping and projection code implemented in MATLAB (Natick, MA, USA) [77]. The recorded channels from the implanted grids were filtered with a common average reference filter within each implanted grid. The filtered signals were then analyzed for time-frequency content by continuous wavelet transform with the non-analytic Morlet wavelet defined by

$$\Psi(s\omega) = \pi^{-1/4} \exp \frac{-(s\omega-\omega_0)^2}{2} \tag{4.1}$$

where $\omega_0 = 6$ and s reflects log scaling factors to obtain $1/4$-octave resolution across pseudo-frequencies 2-200 Hz. We used the absolute magnitude of the wavelet coefficient time series at each scaling. All time series were binned by 50ms and normalized to unit variance per captured channel-frequency.

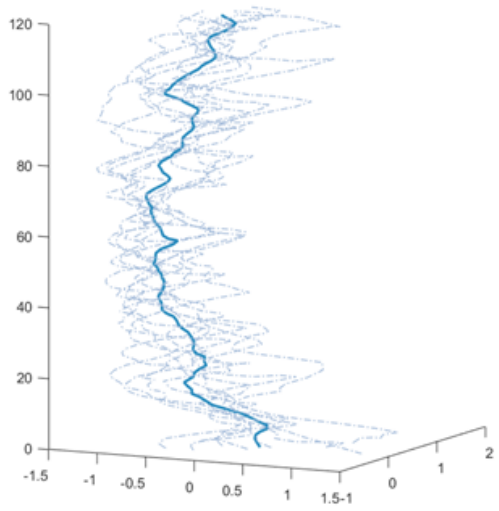

Figure 4.2: Example of deriving the Grasp mean trajectory template for subject A. With repeated trials, the mean trajectory template should contain more task-relevant features and fewer in-trial heterogeneities.

4.2.3 Procrustes Analysis Classification

The filtered and normalized wavelet coefficients, constituting a time series for each channel×frequency pair, was dimensionally reduced using principal component analysis (PCA) to the top 20 principal components (PCs). The time series were then projected into this 20-dimensional space.

Procrustes analysis was employed for classification by statistical shape similarity. The shape of the dynamical signal trajectories of each of 8 grasp conditions: overt- (grasp, ungrasp, pinch, and unpinch) and imagined (grasp, ungrasp, pinch, and unpinch) were analyzed, and for each individual recording session, leave-one-out validation was applied. For all training trials, the mean trajectory templates were computed for each grasp condition. These mean time series were used as templates against which per-condition Procrustes distance

was computed for each testing trial.

$$d = \sqrt{(u_1 - x_1)^2 + (v_1 - y_1)^2 + \dots}$$
$$(u_1, v_1) = (\cos\theta w_1 - \sin\theta z_1, \sin\theta w_1 + \cos\theta z_1)$$
$$\text{where, } \theta = \arctan\left(\frac{\sum_{i=1}^{k} w_i y_i - z_i x_i}{\sum_{i=1}^{k} w_i y_i + z_i x_i}\right)$$

where d is root mean square translation distance of $(u_i, v_i, \dots)$ from the centered coordinate $(x_i, y_i, \dots)$, and θ minimizes the sum of squares distance between points (w_i, z_i) and (x_i, y_i). Fig. 4.5 illustrates the category-mean template trajectories for each individual. The condition with the minimum Procrustes distance bears the maximum 20-D shape similarity to the testing trial, and is classified as that grasp condition.

4.2.4 Lasso Movement Phase Classification

For all visually-guided motor imagery trials we further employed least absolute shrinkage and selection operator (Lasso) regression [82] to determine the phase of the imaginary smooth grasp shaping movement.

Six-fold validation was used where each imagined or overt movement trajectory $r_{w,c}$, with each The 20D mean trajectory of each imagined grasp condition computed from training trials was used to fit linear regression coefficients coefficients β where, the predicted values through time $\hat{y}_t$:

$$\hat{y}t = \beta_{w,c,t} r_{w,c,t} + \beta_0 \tag{4.2}$$

This generates $\beta_{w,c,t}$ as a function of a Lasso regularization parameter λ, which thresholds the number of nonzero β coefficients. λ was chosen such that the mean squared error is lowest in 6-fold cross-validation. Testing trials were multiplied by the regression coefficients to obtain elapsed time since the start of trial to obtain predicted movement phase.

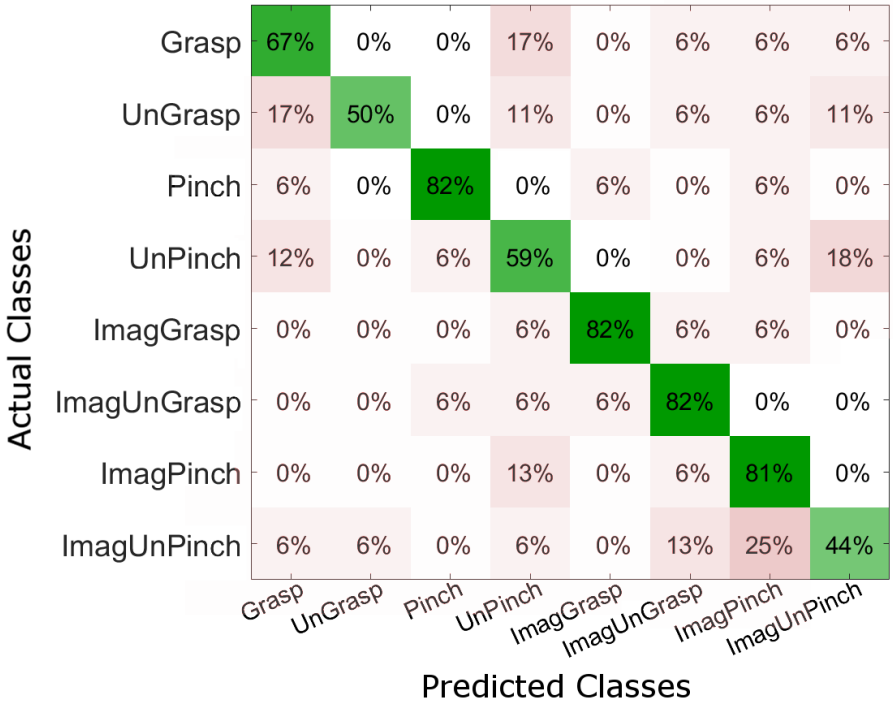

Figure 4.3: Confusion matrix of the model classification accuracies using procrustes analysis using leave-one-out validation, in 136 trials in 3 subjects. Left: Actual conditions. Bottom: Predicted conditions. Main diagonal: Correctly predicted trials. Off-diagonal: Incorrect predictions.

4.3 Results

4.3.1 Grasp Shape Classification Using Procrustes Analysis

Dynamical trajectory analyses reveal separation between grasp types in dimensionally reduced wavelet transform ECoG recordings, as well as trajectory similarities in closely-related grasp postures (see Fig. 4.5). In this case, imaginary trajectories were classified at a higher success rate than overt movement trajectories under Procrustes analysis. Mean true-positive classification accuracy was 68% for all conditions (12.5% chance), and mean imaginary grasp shaping classification accuracy was 72% between 4 conditions. The results of the classification are represented in the confusion matrix in Fig. 4.3.

4.3.2 Movement Phase Regression and Prediction

Cross-validated movement elapsed time agree with predicted using Lasso regression indices in all subjects, with mean $R^2 = 0.4$ across the 3 subjects. This reflects the degree to which each moment within the visually-guided imagined movement is unique in dimensionally-reduced space, and phase can be identified in time by regression alone. Fig. 4.4 illustrates an example of a mapping between the trajectory and elapsed time, and predicted elapsed trial time.

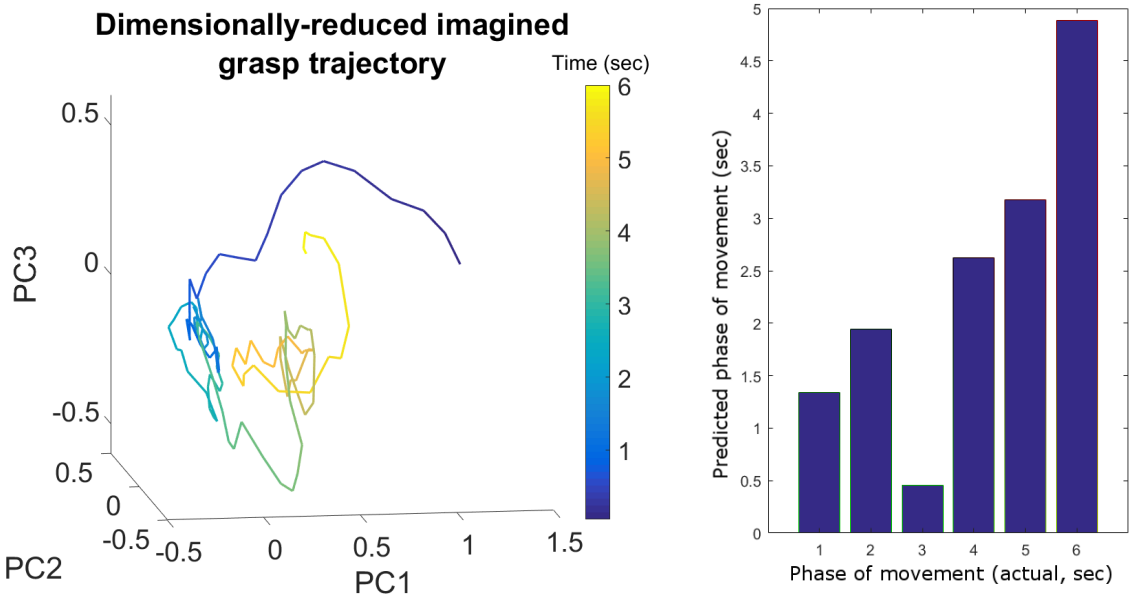

Figure 4.4: Left: Sample mean trajectory for imagined-pinch for subj A projected into the top 3 PCS. Color reflects time elapsed in trial. Note relatively unique mapping for each timepoint in 3-PC space. Right: Sample binned predicted timestamps for the nearest second in a single trial.

4.4 Discussion

4.4.1 Statistical Shape Similarity as Stable Dynamical Feature

In this work, we used Procrustes distance from the mean template trajectory as a proxy measure to classify between dimensionally-reduced, frequency-normalized wavelet coefficients.

We demonstrate high classification performance in distinguishing four different types of both overt and imagined single-trial smooth grasp shaping movements. The success of this relatively simple statistical shape metric carries implications about the nature of the underlying signal dynamics under visually-guided motor imagery.

First, this signifies that the overall trajectory shape of the cortical signal remains relatively stable, despite the existence of relatively large trial-to-trial variances in specific timespans of the trajectory. While each individual trial may exhibit deviations from the expected mean template in certain time segments within a trial, the deviations tend to return to the template trajectory, such that the overall shape of the multidimensional trajectory still more closely approximates its expected overt or imaginary grasp condition, allowing for ordinary Procrustes distance to correctly identify the class.

Second, this result may further imply that task-relevant cortical activity exists in a high-dimensional subspace that is captured by the overall shape of the time series formed by principal component projections of frequency-normalized wavelet coefficients, and that this task-relevant manifold can be relatively resistant to non-task-related spectral changes. While the combination of PCA and Procrustes analysis are not specifically designed to separate task-relevant and task-irrelevant manifolds of cortical activity, the time-locked structure of this visually-guided task may force cortical trajectories perturbed by task-irrelevant activity to return to the nearest task-relevant state, resulting in a preservation of trajectory structure.

Further work into the structure of these dynamics should incorporate techniques that are specifically suited for separating latent factors, such as Gaussian-process factor analysis [90]. Furthermore, specific insights about the task-relevant stability of these trajectories should consider rotation, scaling, and shifting as different manipulations to the dynamical structure of the cortical signals, and their significance with respect to the neural state. For example, trajectory rotations would imply a change to the manifold of underlying cortical signal modulation.

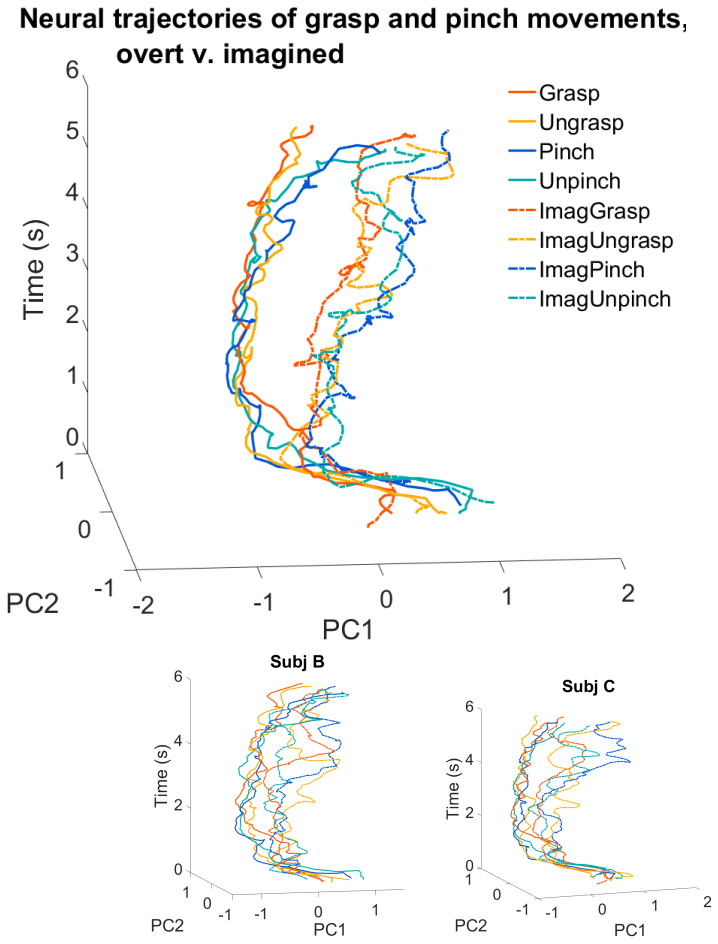

Figure 4.5: Plot of the mean time-varying cortical power spectrum varying through time. Top two PCA components shown in x-y plane. Left: Subject A. Right top: Subject B. Right bottom: Subject C.

4.4.2 Somatotopic Localization of Principal Components

The top PCs of all recorded electrodes in all subjects involve sensorimotor cortex, premotor cortex, and posterior parietal regions when electrode coverage is available, as expected. However, other PCs involve regions not traditionally associated with motor movement, such as dorsal temporal regions or the temporoparietal junction. These may reflect task-dependent modulation in visual attention during the task, or other unidentified internal representations of motor imagery warranting further investigation. Further work may involve identifying

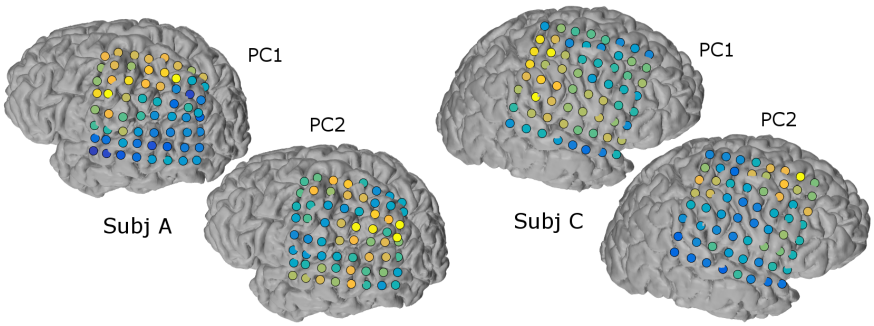

Figure 4.6: Example localization for the top PC weights for two subjects. Contributions from all frequency bins have been summed (root sum of squares) for spatial visualization. Blue: Low contribution to PC. Yellow: High contribution to PC. Note this 2D representation collapses frequency and cannot represent the full range of trajectory features subsequently used in procrustes analysis.

transient functional connectivity changes between these regions, and identifying similar clusters of spatial-spectral interactions between regions during guided visual imagery.

4.4.3 Movement Similarity Hierarchies

As can be both observed in Fig. 4.5 and Fig. 4.7, there is a strong similarity within the overall trajectories of all overt movements, but very different dendrograms are seen between visually-guided imaginary movements. Some of this variability can be attributed to different electrode placement, but the retained high classification rate implies that despite varied placement, different individuals retain structural consistency in individual time-varying representations of imaginary grasp-shaping behavior, in a wide variety of motor and non-motor regions.

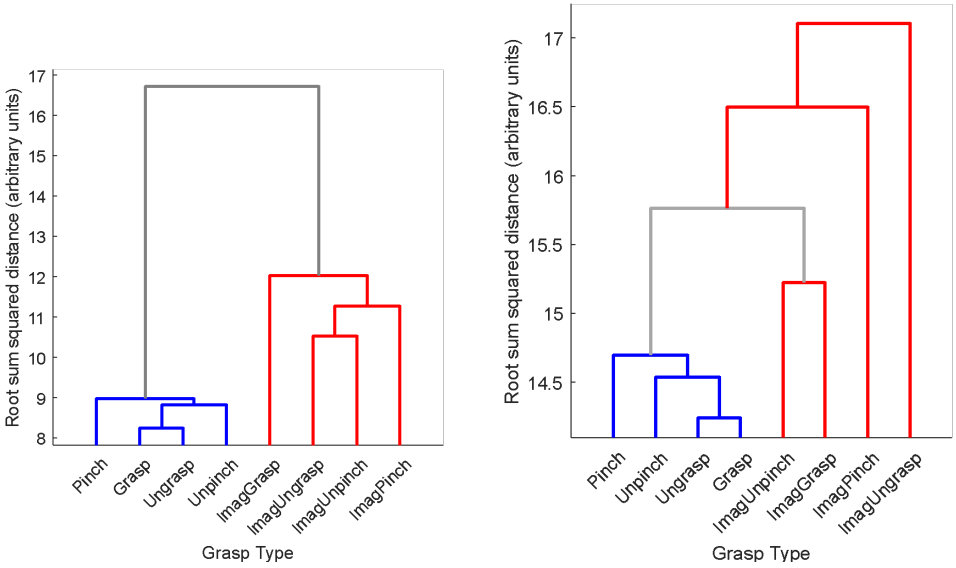

Figure 4.7: Grasp trajectory similarity dendrogram computed as the sum squared euclidian distances across time between mean grasp condition template trajectories for left: Subj A, right: Subj C. Even with varying electrode coverage, different individuals have very similar overt grasp similiarity hierarchies, but very different imaginary similarity hierarchies.

Chapter 5

VISUOMOTOR SPATIAL TRANSFORMATIONS IN MOTOR PLANNING

5.1 Introduction

The successful performance of a goal-oriented coordinated task requires rapid transformation between several frames of reference; this includes an environment-centered allocentric frame of reference, to a torso-centered egocentric frame of reference, upon which limb positions, joint angles, and proproceptive feedback can be successfully computed in a reach-to-grasp motor task. Understanding the multiple roles of spatial coordinate transformations in a visuomotor task can be crucial to the development of rehabilitative and predictive neural interfacing technologies that rely on visual cues in the environment to help control user motor outputs. These rehabilitative and assistive devices, whether it be in the form of a high-DoF biological or artificial limb, or in applications of direct brain computer interfacing, ultimately requires a real-time mapping between visual inputs, proproceptive signals, and individual muscle activations. Furthermore, understanding spatio-visual transformations in motor planning may also be crucial to the development of complex arrangements of teleoperated robotics, and avatars in virtual reality.

Three distinct bodies of literature involve rotated frames of visual reference in some way. Prism adaptations using head-fitted mirrors or lenses, first pioneered in the earlier part of the century [91, 92], illustrates both the remarkable ability for rotated visual inputs to be remapped into a sensorimotor feedback loop over time, but also illustrates its relative lack of generalizability. For example, this type of visual learning is demonstrated to not translate between different motor tasks, or different speeds by which the motor tasks are performed [93, 94]. This relative non-generalizability does not appear to apply for the rotational context

switching we experience in the world, as reach-to-grasp objects placed in different egocentric frames of reference do not require task-specific training.

Another body of literature involves adaptation to control trajectory errors [95, 27, 28]. This extensive body of work is usually performed with 2D overt movement cursor control, where a rotated control basis is introduced, or additional noisy rotation errors are superimposing to a center-out 2D control task. In multiple studies, *Krakauer et al.* localizes neurocorrelates of these trajectory adaptations to visuomotor disturbances to the posterior parietal cortex, with a well-documented learning and consolidation curve over multiple sessions. Furthermore, the adaptation appears to be remapped to the movement control trajectory itself, instead of the spatial imagery of the target position [29]. However, these tasks also demonstrate an adaptation "tuning curve" of up to 60° of visual perspective disturbance, within which trajectory correction can successfully occur. Additionally, these adaptations do not exhibit bimanual transfer, even when performed as a three-dimensional task [95]. While these feedback adaptation mechanisms explains small-angle task-specific disturbances using motor feedback circuits, the role of feedforward large rotational spatial disturbances, with or without the contribution of circuits related to previous motor memory or reinforce learning, is unclear. It is further not understood the origin of neural correlates for which feedforward motor planning might adapt, using visual cues, to visual disturbances of larger angles such as 180°.

The final body of literature involves rotated spatial maze navigation, where model animals navigate an egocentric environment continuously, without an internal representation of singular movement trajectories, by free exploration with many possible allocentric visuospatial frames of reference. In this body of literature, we see the correlation between hippocampal "place cells" that may encode internal spatial representation of location in a "cognitive map". In this modality, we have ability to recall locations in cognitive map from dissonant visual inputs from differing perspectives, and engage a generalized remapping of our motor behavior where all sensorimotor coordinates become re-aligned to this new environment. In other words, cognitive spatial maps can be inferred from sets of 2D visual cues,

with the constraint of rotational invariance [96, 17]. What allows for this generalizable and transferrable ability to use new spatial maps, when prism adaptations and trajectory error adaptations exhibit task-specific learning?

The emerging body of literature points to the possibility of the subiculum, located directly in between the hippocampus and motor-rleated basal ganglia structures as the "motor output" of the hippocampus, as a significant cortex where hippocampal place fields that constitute cognitive spatial maps may be rotated [22]. These *head-direction cells* associated with the subiculum may be associated with an internal sense of rotation in the world, as they fire with high degrees of correlation to place cell activity as well as head direction [26], and may process and compress spatial high-dimensional spatial representations into contextual information other distributed regions can use [96]. More recently, the subiculum has been implicated in encoding precisely the axis of spatial map alignment [97], and is associated in humans in 2D navigation tasks near virtual boundaries [98].

We propose that the concordance of previous work on the subiculum may point to its function as a hippocampal output, where multiple place representations in the hippocampus is combined to create generalizable, rotationally invariant mappings usable by visuomotor systems for motor output. In order to investigate the contribution of the subiculum to the processing of spatial frames of reference in a manual manipulation task, we constructed a task that contained continuous-feedback, overt-motor controlled, fixed-view synchronized visuomotor rotations. This combined the elements of both maze navigation and motor trajectory correction, in a third-person setting, in order to interrogate whether or not the subiculum is engaged during this proxy for fine manual manipulation under visuomotor disturbance.

Finally, we attempt to demonstrate the direct involvement of the subiculum in motor performance by altering the behavior in the subiculum-adjacent area via direct cortical simulation.

5.2 Methods

5.2.1 Experimental Design

We implemented a novel visuomotor rotation task in order to replicate and isolate the effects of continuous movement control and cognitive spatial map rotation. In order to engage both navigation and motor learning circuits under different rotational disturbances, the virtual simplified maze environment was created in the Unity game engine (Unity Technologies, `https://unity3d.com/`) in third person view.

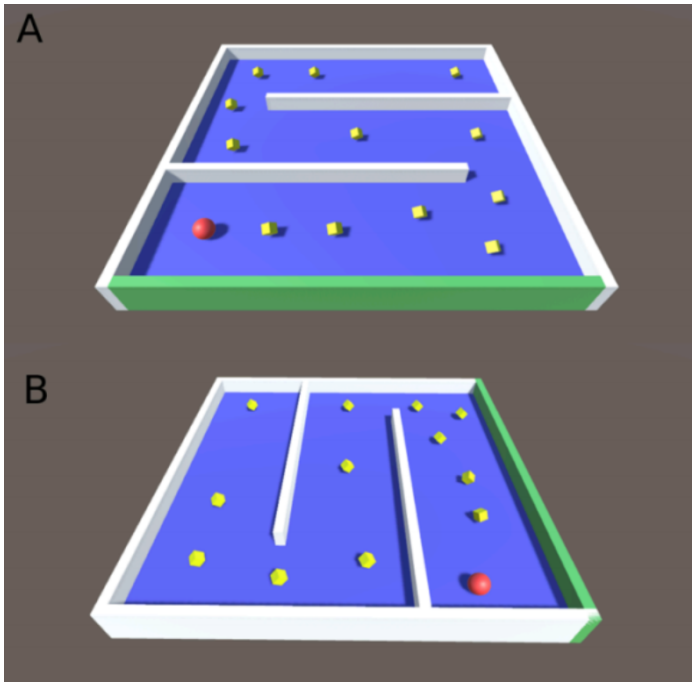

Figure 5.1: A virtual simplified maze task with velocity mapping to trackpad. The controlled avatar appears as a red ball in the center of the maze, with yellow cubes as designated targets. This virtual maze environment rotated to one of four camera orientations: 0° (unrotated), 45°, 90°, and 180°.

Eleven patients with normal motor function volunteered for this study during clinically recommended invasive monitoring of seizure-related cortical regions, with written, informed consent through a protocol approved by the Institutional Review Board. All subjects subject

received a pre-operative anatomical MRI, and was implanted with 1×8, 1×10, 1×12, or 1×14 stereotaxic EEG depth electrodes (PMT Corporation, Chanhassen, MN, USA), and/or a 8×8 platinum electrode grid (Ad-Tech, Racine, WA, USA), along with 1×8 and 1×6 electrode strips (strips excluded from this analysis). All sEEG electrodes consisted of 1.1mm diameter, 2.3mm length platinum cylinders, set around silastic cylinders with center-to-center distances of 5mm. All electrode grids and strips consist of 3mm diameter platinum discs, set in silastic with center-to-center distances of 10mm. Subsequently, X-ray CT imaging captured the location of the electrodes. These electrodes were sampled at 4882.8 Hz on a 128-channel Tucker-Davis Technology (Alachua, FL, USA) System 3 RZ5D Neurophysiology Base Processor with associated PZ5 NeuroDigitizer.

Pre-operative MRI was co-registered with postoperative CT using Statistical Parametric Mapping (`http://www.fil.ion.ucl.ac.uk/spm`), with the pial surface reconstructed with FreeSurfer (http://freesurfer.net) and custom mapping and projection code [77] implemented in MATLAB (Natick, MA, USA).

5.2.2 Task Design

The trackpad is directly mapped to the movement of an avatar in this fixed-perspective simple maze. Unlike previous task designs optimized for error trajectory correction, this design facilitates recall by adding a spatial landmark; the green wall of the maze always indicates the perspective of the original maze orientation without any rotational disturbances. The controlled avatar appears as a red ball in the center of the maze, with yellow cubes as designated targets. Furthermore, the direct velocity-to-velocity mapping of the trackpad movement, to that of the ball avatar, emulates the characteristics of a manual manipulation task rather than a maze navigation task. This virtual maze environment rotated to one of four camera orientations: 0° (unrotated), 45°, 90°, and 180°. In each case, only the third-person camera angle is rotated around the perimeter of the maze; the trackpad controls remain in the unrotated axis and therefore experiences a control basis rotation of 45°, 90°, and 180° respectively in the latter 3 conditions, to which the subject must adapt in order to

complete the task.

Verbal instructions are given in order to explain the task goals and the colored visual cue for rotation, which is provided as a green maze wall associated with the unrotated viewpoint. Patients are instructed to complete the maze sequentially by moving the avatar through each of the rotating cubic markers in turn, until all target markers have disappeared, at which point the researcher resets and rotates the maze to one of 4 randomized camera orientations. The subjects were instructed to solve sequential randomized rotating mazes sequentially, for at least 4 trials of each maze type or approximately 20 minutes. The task was synchronized via square wave audio pulses emitted by Unity to the neural recording system, empirically calibrated for operating system digital-to-analogue converter delay.

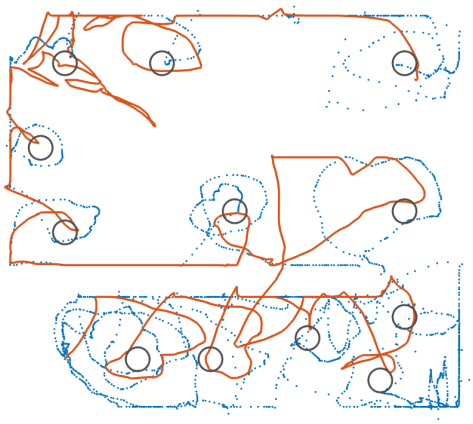

Figure 5.2: Sample of average task performance. Plot represents the maze being traversed as if in unrotated condition. Red line represents one maze run-through with a 45° camera rotation. Blue dotted line represents a run with a 90° camera rotation. Note the initial deviation in the red line by approximately 45°, to which the subject quickly adapts. 90° task adaptation is not as apparent, and the errors are a lot larger.

5.2.3 Data Processing

Behavioral data in the Unity task were logged at display framerate (60Hz) to flat files with time, avatar position (x, z, y), control axis (dx, dy) magnitude, and audio-producting event timestamps. This behavioral data is upsampled and interpolated in order to align in time with captured sEEG and ECoG data. An optimal track is computed that passes through all maze targets in order of likelihood for capture, to compute a quantification of deviation from optimal track trajectory. For each accumulated movement segment (1/60 sec), angular deviation as cosine angle error from optimal track trajectory is accumulated.

Subsequently, sEEG and ECoG data were processed. Artifacts were removed from raw electrophysiology time series, and line noise was removed with notch filters at 60, 120, and 180Hz. Broadband changes were extracted with a 4th order Butterworth band pass filter (70–200 Hz) to select for γ-band activity. Power spectrum envelopes were then extracted by taking the Hilbert transform. An ANOVA analysis was performed in order to localize electrodes with the maximum maze-rotation-specific modulation, controlled for movement velocity and track trajectory deviation.

5.2.4 Stimulation Design

We conducted direct cortical stimulation (DCS) studies after subjects were placed back on anti-epileptic medications (AEDs), and all subjects gave written, informed consent. This usually means patients had one or two days of pre-stimulation training sessions and prior experience with the task, which can exhibit a learning effect in some rotational cases. During the stimulation day (50 Hz, 200μs pulse width, 4 second trains with 4 seconds on, 4 seconds off) stimulation applied to subiculum-adjacent structures to the best of our localization in order to observe the effect on recall performance. Additionally, control stimulation is applied to off-target structures far from suspected epileptogenic areas not believed associated with rotation learning.

5.3 Results

5.3.1 Identify structures associated with visual rotation

We find broadband (70-200Hz) changes in 3 patients, located to or near the dorsal parahippocampal gyrus in the subiculum, as previously determined by MRI-CT coregistration. In particular, these regions demonstrate statistically significant modulation of broadband changes to camera rotation condition in the task, controlled for other task-related behavior such as avatar movement, or deviation from optimal trajectory, as seen in Fig. 5.3.

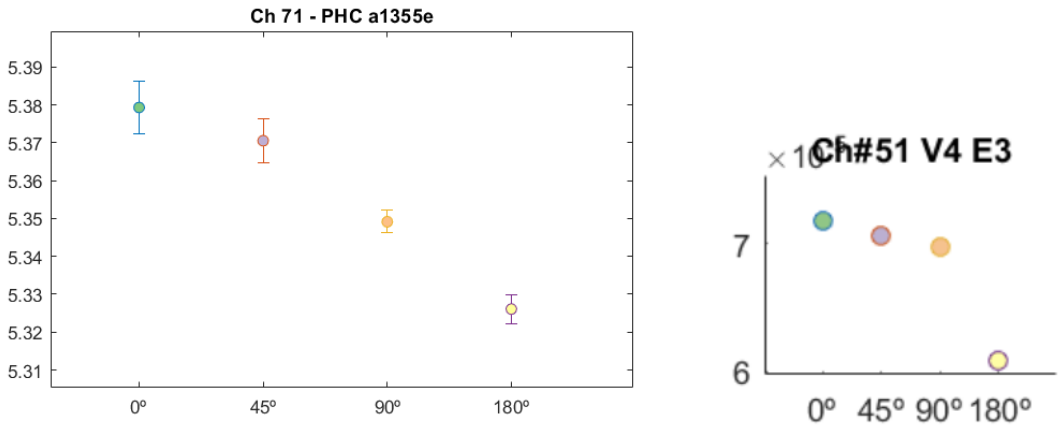

Figure 5.3: High-γ modulation at the subiculum with respect to rotation in two subjects. Arbitrary units; note that in both cases 180° rotation condition constitutes a statistically significant in a lower average spectral power in broadband γ.

This result is of particular interest due to recent work in this region in both rats and humans exhibiting potential correlations with spatial navigation boundaries [98], as well as axis orientation of navigational goals with respect to known visual landmarks [97].

5.3.2 Alter visuomotor rotation task performance with DCS

Interestingly, with potential implication to the specificity of the 180° rotation adaptation, on-target task-nonspecific stimulation with 4s-on, 4s-off waveform statistically significantly affected activity in the 180-degree task condition in one subject tried, as seen in Fig. 5.4.

As no statistically significant effects were found in any other condition, we hypothesize that this target effect is specific to recall or processing of a particular transformation.

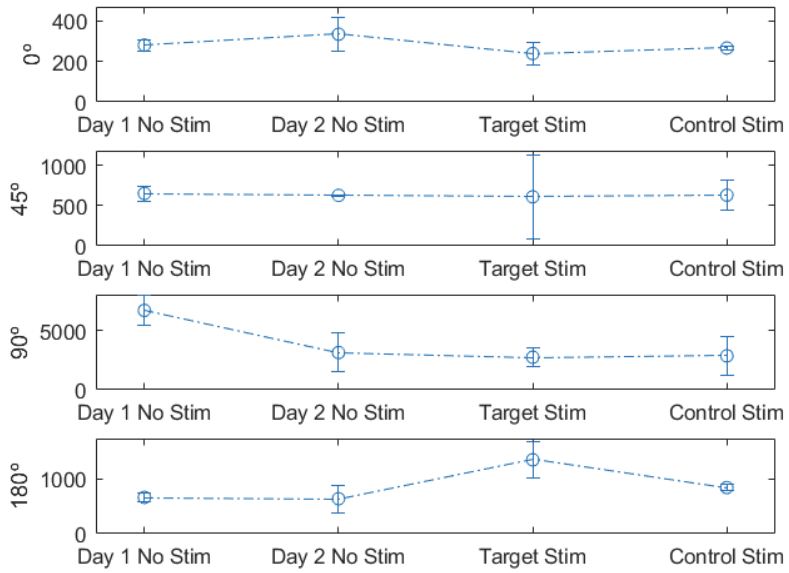

Figure 5.4: Cortical stimulation disruption task to the parahippocampal area. All four rotation conditions are represented from top to bottom. Y-axis in each plot is accumulated cosine error, and thus the lower the Y-axis, the better the task performance. Note the rise in task error and therefore reduced task performance during target stim in the 180° condition.

5.4 Discussion

In recent work in *Olson et al.* [97], specific dorsal subiculum activity entrained to the axis of the maze is observed, when rats were landmarks around the room with which to reorient their cognitive map of the maze. We believe this landmark-based orienting behavior of inferring the axis of a rotationally-invariant spatial representation of their environment is of particular significance. In this task, a difference in a subiculum activity correlate seem to be observed in a specific rotation condition, which is also the rotation condition that may have been specifically disrupted in targeted stimulation.

This may be associated with another interesting phenoma in rotated manual tasks: compared to the 90° rotation condition, for most individuals the 180° rotation task is usually easier and more performant, for unknown reasons. We hypothesize that this increased performance may be an adaptation to mirror usage, for which the axis of reflection behaves identically in a third-person maze task as a 180° board rotation. If so, our existing ability to rotate internal cognitive maps may be disrupted by targeted stimulation in the DCS alteration task.

Another recent work with sEEG electrodes implanted in a navigation task is the work done by *Lee et al.* [98], where distinct correlations of spatial boundaries were found in subiculum electrodes as the first-person avatar controlled by the subjects approached a virtual environmental boundary. The authors hypothesize in this case that these 1-4Hz and 4-10Hz modulations may be associated with boundary recall. Given our current findings and the previous literature on the likely role of the subiculum with regards to head direction and landmark axis rotation, we believe that these modulations may be signatures of active attempts at rotation of the subjects' internal cognitive spatial map, in order to navigate to new targets.

Future work in this area should examine the relation between task learning and rotation. One way of investigating the hypothesis of learned mirror behavior is to see if the subiculum modulation characteristic is directly associated with task performance in 180° rotation conditions as compared to unrotated, though task performance may be relatively difficult to quantify here. Another avenue of investigation is to observe the within-trial maze performance in order to observe the interaction between this visuospatial rotation effect, and that of the trajectory correction effect that would be most likely observed in the 45° condition. Splitting the behavioral performance into inter-target segments in order to observe the effect of the rotation on a particular segment's performance can reveal learning in specific maze configurations.

Chapter 6

ENGINEERING TOOLS FOR PATIENT-INTERFACING NEUROENGINEERING

6.1 Motivation

We present here a series of visualization and hardware "glue" tools for interfacing between the needs of research instrumentation and the highly regulated tools used in clinical environments. Researcher-focused tools must be easy to deploy, intuitive to use, and without compromising patient safety.

6.2 Interactive Neural Connectivity Visualization

Adapted from published work [99] ©2017 IEEE. Reprinted, with permission from authors.
We present here a browser-based application for visualizing patterns of connectivity in 3D stacked data matrices with large numbers of pairwise relations. Visualizing a connectivity matrix, looking for trends and patterns, and dynamically manipulating these values is a challenge for scientists from diverse fields, including neuroscience and genomics. In particular, high-dimensional neural data include those acquired via electroencephalography (EEG), electrocorticography (ECoG), magnetoencephalography (MEG), and functional MRI. Neural connectivity data contains multivariate attributes for each edge between different brain regions, which motivated our lightweight, open source, easy-to-use visualization tool for the exploration of these connectivity matrices to highlight connections of interest. Here we present a client-side, mobile-compatible visualization tool written entirely in HTML5/JavaScript that allows in-browser manipulation of user-defined files for exploration of brain connectivity. Visualizations can highlight different aspects of the data simultaneously across different dimensions. Input files are in JSON format, and custom Python scripts have been written

to parse MATLAB or Python data files into JSON-loadable format. We demonstrate the analysis of connectivity data acquired via human ECoG recordings as a domain-specific implementation of our application. We envision applications for this interactive tool in fields seeking to visualize pairwise connectivity.

6.2.1 Introduction

We present an interactive exploration tool specifically tailored to visualize large numbers of pairwise neural connectivity dynamics. We further demonstrate the utility of this tool for analyzing pairwise connections across various regions of the brain based on electrocorticography (ECoG) data.

Interpreting neural connectivity is a challenging problem because cortical connectivity visualizations are largely exploratory and require the encoding of many multivariate attributes that exist for each pairwise edge, as each edge can be its own high-dimensional correlation matrix. These multiple metrics for each connection require an investment of user time to navigate and interpret. Unlike social networks or aggregate flow for which directed graphs are often designed, neural connectivity is highly nonstationary through time, and the set of descriptive statistics change rapidly. This adds many potential encoding dimensions for any visualization tool, leading to a critical need for user interactivity to explore data and formulate appropriate questions. Fig. 6.1 highlights sources of data, and potential dimensions along which a user may seek to subselect and visualize the data.

Our dataset explorations emphasize the use of the tool to analyze pairwise connectivity in ECoG datasets. The utilization of our tool demonstrates a unique opportunity to apply and extend existing interactive visualization techniques, such as chord diagrams, dynamic querying and selection, and interactivity, to exploratory neuroscience.

6.2.2 Related Work and Motivation

Visualizing neural connectivity is a significant problem in the field of neuroscience. Examples of current tools to address this problem can be found in a centralized repository named “The

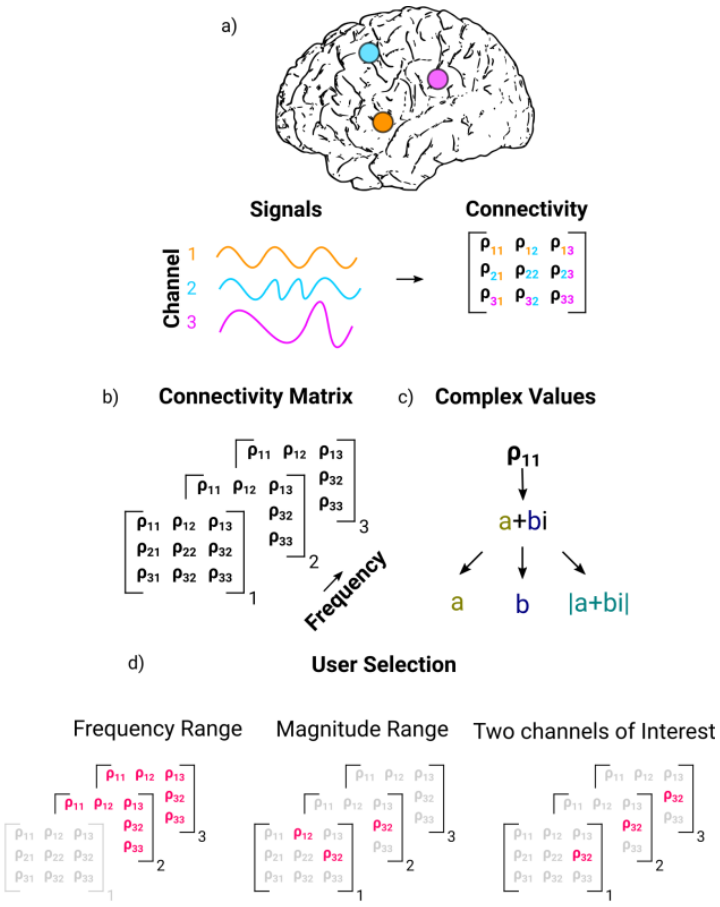

Figure 6.1: A) Sources of ECoG signals, which can be generalized to any spatially specific measurement of correlation. From these time series traces, researchers calculate matrices of connectivity values. B) connectivity matrices often exist for various frequency bands of interest, and D) are often complex valued. D) various dimensions of matrix selection.

Neuroimaging Informatics Tools and Resources Clearinghouse" (NITRC) founded by the National Institutes of Health (NIH), which hosts hundreds of tools (mostly for MRI data) for the analysis and visualization of Neuroimaging data. A subset of tools for MEG and ECoG data are available as MATLAB plugins, which require package download, a MATLAB license, and a user interface with a powerful but complicated software suite. We propose instead an open source, browser-based visualization toolkit.

Other past visualization techniques include rendering each anatomical location on a vir-

tual cortex. However, this approach often leads to occlusions in the resulting visualization due to the sheer number of overlapping connection pairs. Additional techniques include static graphs of frequency dependent functional connectivity through undirected graphs based on fMRI data [100]. Of note is the labeling of various anatomic locations in free space, with a web of connections. While this common visualization demonstrates connectivity between numerous nodes and captures the connectivity of the system, we sought a more intuitive way to represent connectivity.

A review of various methods [101] demonstrates different approaches used in the past for demonstrating both functional connectivity (correlations in activity between various regions) and anatomic connectivity (fiber tract density between regions). Visualization strategies range from literal demonstration of the brain's anatomical structure, to more abstract visualizations depicting the brain with nodes and edges. We sought for our application a simple, uncluttered interface highlighting connectivity patterns without requiring rotation to visualize obscured regions.

Other recent advances in visualization of neural data include the folding of time curves to visualize patterns of temporal activation [102] and stacking of adjacency matrices representing temporal snapshots to visualize changes in networks over time [102]. While these tools offer great flexibility and exploratory depth in dealing with time series data, we desired a simpler, more lightweight approach to visualize connectivity matrices which were constant across a time period. We wished to implement strategies similar to the interactive pruning [102] and rapid exploratory nature of the above tools. We also desired a tool agnostic to the underlying data matrix, enabling the use of whichever connectivity value the researcher desires.

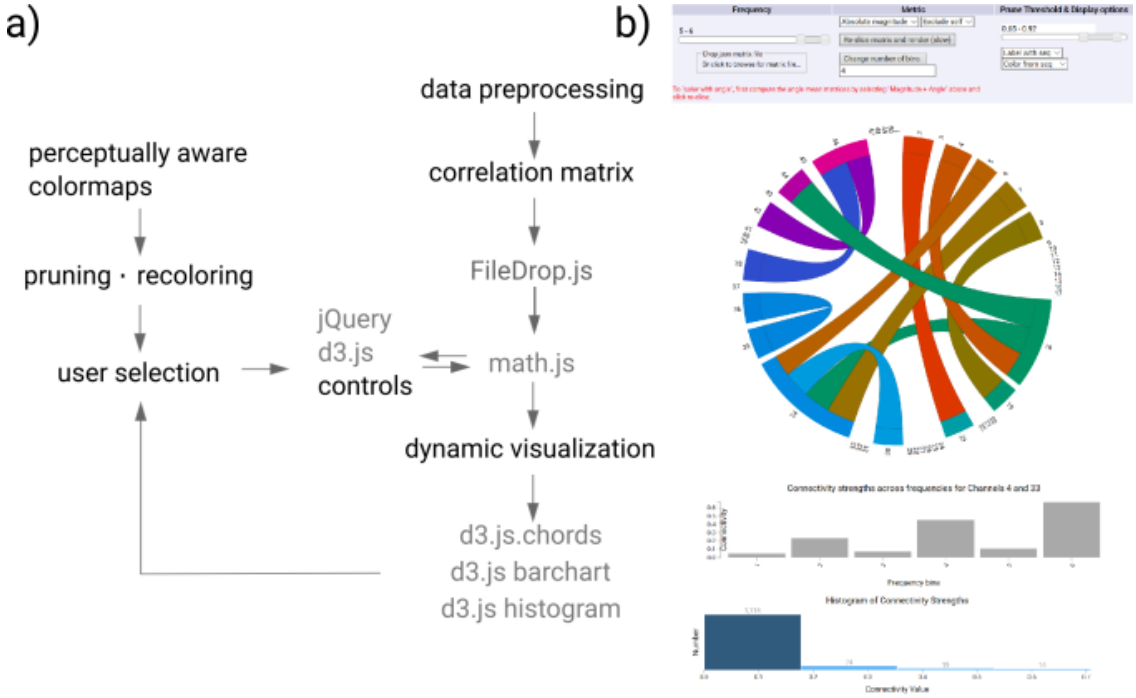

Figure 6.2: a) Schematic overview of the approach to data visualization. b) Example screenshot from the visualization highlighting the use of subselection, thresholding, dynamic bar graph generation, and hover feature.

6.2.3 Methods and Implementation

Visualization Architecture

Our visualization architecture, with corresponding static screenshot, is shown in the schematic in Fig. 6.2. A correlation matrix (3D matrix of connectivity strengths at various sensor locations and frequency ranges) is loaded into a client-side JavaScript-enabled page in a desktop or mobile browser via drag and drop or a browsing menu. The correlation matrices, nested arrays in JavaScript Object Notation (JSON) format, are loaded using HTML5 standards compatible file handing routines. These datasets can be generated by the end-user, by conversion from either a Python numpy data file or a MATLAB data file, using our included Python script. These two data formats represent the vast majority of pairwise connectivity data in neuroscience.

The basis upon which our visualization builds upon is the d3.js [103] implementation of Krzywinski's "circos" [104], which we chose as a visualization technique for representing pairwise connections with minimal occlusion. Our implementation can handle non-symmetric connectivity matrices, where there is directional connectivity strengths between nodes. For additional visualization dimensions, we simultaneously plot dynamic bar charts between pairs of electrodes across frequency bands, as well as a global histogram that demonstrates the average strength across all frequencies for all nodes. For the implementation to be functionally usable, the interface must be extended with interactivity that is rapid and responsive when selecting and visualizing more information about pairwise connections.

The user selects a frequency range of interest, a statistical measure of interest (absolute value or magnitude and phase information, if both are present), the inclusion or exclusion of self-connections, and then presses the "re-slice matrix and render" button to submit the query and update the chord diagram (Fig. 6.2). This uses the JavaScript math.js library to subselect and compute an average matrix slice across the selected frequencies. The browser-based controls use JavaScript d3.js and jQuery controller frameworks to create cross-platform, responsive controls. The user-selected threshold cutoff value dynamically prunes connections above or below the selected strength from the diagram in real time. A callback with active tweening of the arc and chord shapes with d3 transitions conveys a smooth but rapid transition between rendered frames (Fig. 6.2a).

As the color representation of nominal categories is extremely important [105] and spatial information must be accurately conveyed, we tailored a `CIE L*a*b` colorscale that fades in two directions, as well as an `L*c*h` colorscale that transitions in color unidirectionally (Fig. 6.3b). In this way, the two `CIE L*a*b` colors correspond to spatial locations on our ECoG grid. For datasets where spatial ordering is not as clear, the `L*c*h` unidirectional colorscale emphasizes separability of nodes. Additional color files can be supplied by the user to tailor the data conveyed by color.

Once the chord diagram is set up for visualization, the user hovers over a node or a chord to display connection strengths for that node, or between the two nodes specified by a given

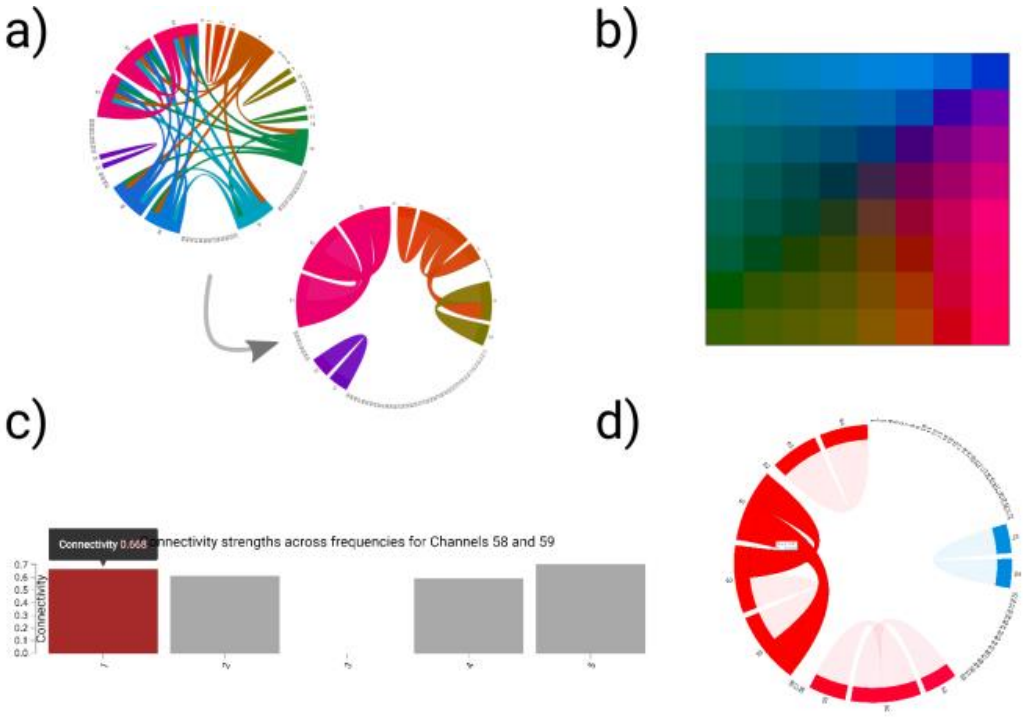

Figure 6.3: a) example screenshot illustrating rapid fade and tween pruning using a single slider to select for maximally salient chords and remove occlusion. Note that regions with similar colors convey a local group of intra-region connections while dissimilar colors convey longer distance, crosscortical connections. The user then has the option to color the chord diagram based off anatomic locations from a file (if present), or in a constant luminance scheme based off sequential order. b) A modified `L*a*b` colorspace controlled for luminance for coloring arcs representing spatial locations around the chord diagram to give the user rapid assessment of sensor proximity. Hover-over functionality for both c) the bar chart and d) chord diagram.

chord. An additional user option for coloring via mean phase angle of the connection uses a divergent color palette from ColorBrewer (`colorbrewer.org`) to show differences between positive and negative phase angles in complex data.

Upon clicking a chord, a bar graph dynamically updates to display connection strengths across frequencies for the two nodes of interest (Fig. 6.2b). By hovering over any bar in the chart, the connectivity strength for that frequency will be displayed. These features were implemented using the "hover" and "on click" functionalities from JS and d3 (Fig. 6.3c,

d). By revealing the connection strengths across all frequencies, the user gains additional insight into the topology of connectivity for two regions without losing the global connectivity pattern provided by the chord diagram.

For any selected set of frequencies, a histogram displays all channel-by-channel connectivity values in a given frequency range (Fig. 6.3b). Using interactive JS functionality, users input a desired bin size to visualize different binnings of their data, allowing for rapid coarse and fine visualizations. By the combination of dynamic features, and three separate visualization strategies (chord diagram, bar chart, and histogram), for the data, users can interpret their datasets in a multifaceted manner without any software downloads or programming.

All provided datasets were acquired with written informed consent through a protocol approved by the University of Washington Institutional Review Board. Our sample data sets are human ECoG datasets acquired during a resting state, where the subject was not actively engaged in any task. Data were processed for connectivity metrics [106].

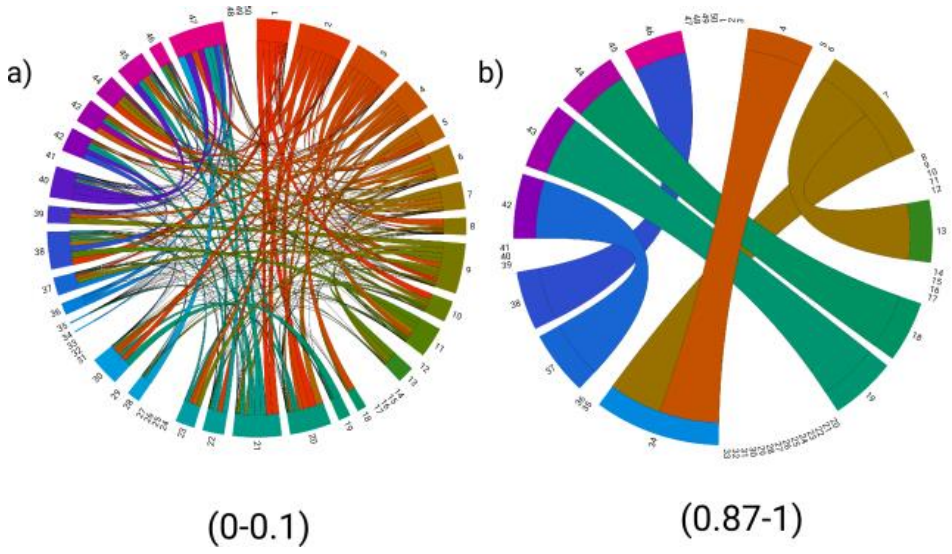

Figure 6.4: ICC values in the high gamma (70–200 Hz in ECoG) range for nine subjects. A) low thresholded values, illustrating many long-range unstable connections. B) high thresholded values, illustrating fewer, mostly local, stable connections. We highlight the connection between Brodmann areas 4 and 34, motor cortex and entorhinal cortex, respectively.

The screenshot in Fig. 6.2b illustrates our visualization tool. We use this tool to explore connectivity matrices of differing values, including phase locking value (PLV) [106], phase slope index (PSI), correlation, and coherence, as well as intraclass correlation (ICC) of these measures over time [107]. Of note is the ability of the application to handle different statistical measures of connectivity, highlighting its extensibility to other data types and data sets. Of note is that our example involves symmetric connectivity, but our application can handle non-symmetric matrices. In this instance, the chord would be thicker near the node with the greater value for the asymmetric matrix. This is useful when looking at connections that are stronger in one causal direction than another.

One particular application highlights (Fig. 6.4) the use of our tool to explore ICC over three sessions of PLV in the high gamma band (HG, 70–200 Hz in ECoG) between various regions of the cortex across 9 subjects. PLY describes the consistency of a phase difference between two signals throughout time, while ICC is an ANOVA-based metric for the evaluation of the stability of connections over time across multiple individuals. The stationarity of brain signals is a topic of research interest in assessing the function and structure of cortical networks. HG signals in ECoG are known to be associated with local synchronous neural activity [108]. We use our application to first prune high gamma (70–200 Hz in frequency) ICC values to a low ICC value range (Fig. 6.4a), revealing widespread unstable connections between regions. Although difficult to currently interpret, this visualization allows us to further analyze these highly unstable regions. Further exploration of high ICC values demonstrates fewer, more local stable connections over time (Fig. 6.4b). An example chord of interest illustrates the high ICC between Brodmann areas regions 4 and 34, representing a highly stable connection between motor and entorhinal cortex. Entorhinal cortex is associated with spatial processing [109], positing interesting questions to explore as to why this region might have stable connections with motor cortex. This finding highlights the use of our tool to explore novel connectivity patterns uniquely available from human electrophysiological recordings.

A different data set explored by our research group assesses the spatial representation

of connections across the cortex. Using PLV as a metric, we first subselect and visualize connectivity related to the beta band (13–30 Hz, Fig. 6.5a) and PLY between 0.65 and 1. After switching to high frequency (high gamma) PLY and thresholding for the same values (Fig. 6.5b), we observe a different pattern of connectivity. This emphasizes the utility of our tool as an exploratory form of analysis to inform further inquiries.

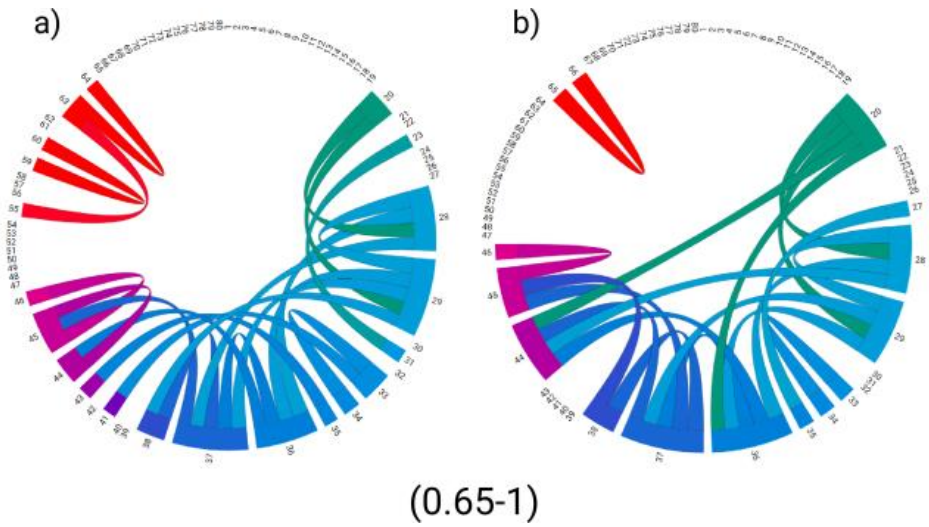

Figure 6.5: PLV values for a single subject. A) beta band (13–30 hz) displaying local, looping connections. B) high gamma, 70–200 hz), displaying a different pattern of connectivity.

Our results for test matrices of size $65 \times 64 \times 64$ and $5 \times 64 \times 64$ reveal re-rendering and math. js processing within 500 ms to a second depending on the user's' machine. Code profiling revealed the bottlenecks to be in the math. js processing and computations on matrices, so in the event of matrices orders of magnitude larger than our current ones, we may need to consider alternative approaches. Since the visualization tool does not require any additional software packages, this is a significant advantage over existing tools that may require MATLAB or other software on the end user's computer.

In conclusion, we demonstrate a browser-based, open source, easy to use application to quickly visualize, prune, reslice and explore complex data matrices encoding relationships between pairwise nodes.

6.3 Simulated Automatic Mouse Input

We created an open hardware input mouse simulator in order to adapt to existing clinical hardware in high-compliance voltage neural stimulation experiments. While available clinical neurostimulators such as the Cadwell Cascade IONM (Cadwell, Kennewick, WA, USA) offer safe, approved evoked potential experiments with the capacity of μs waveforms with controllable compliance voltages of up to $100V$, the existing operating interface is restricted to manual operation. In order to automate the process of precisely timed regular delivery of cortical evoked potential stimulation, we created an external simulated USB-HID (Human Input Device) with adjustable timing controls in order to conduct motor evoked potential experiments.

An Adafruit Feather 32u4 (Adafruit Industries, New York, NY, USA) based on the `Atmega32u4` chipset was used in order to simulate a USB-HID input device, and issue mouse click commands. The resulting microcontroller prototype can be adjusted to issue unlimited mouse click events with an interval between 50 ms to multiple seconds, in a steady fashion. This prototype can be seen in Fig. 6.6. The microcontroller firmware can be found at `https://github.com/uwgridlab/Automouse`.

6.4 Audiovisual Synchronization

We created an open hardware synchronization circuit in order to afford better flexibility in recording the task performance concurrently with neural signals. The circuit design allowed for audiovisual pulses from the stimulus presenting system to be directly connected to a clinical headstage with 100-microsecond latency, while preserving galvanic isolation and safety of the study patient.

As clinically used medical equipment are heavily certified to electrical safety standards, the most important among which is IEC 60601 (`https://www.iso.org/standard/65529.html`), which limits allowable patient leakage currents in normal operating conditions to within $10\mu A$. As a result, in order to automate behavioral data collection of existing non-

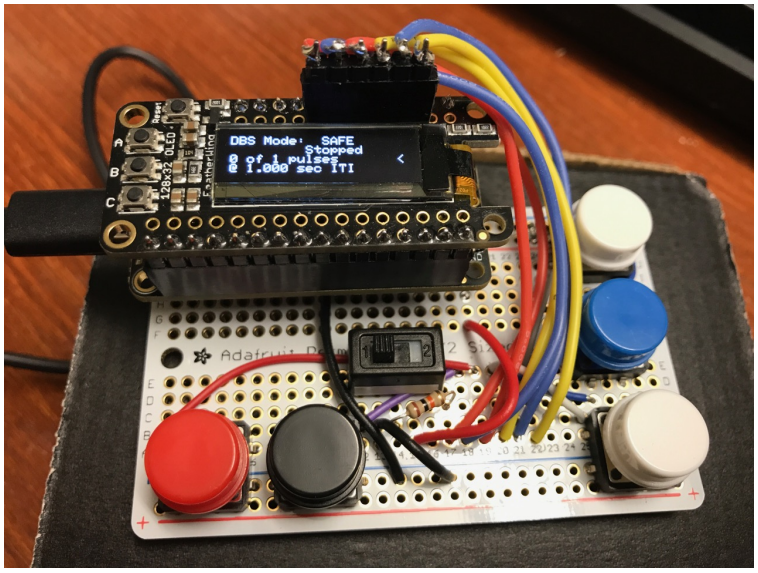

Figure 6.6: Adafruit Feather 32u4-based open hardware input mouse simulator that issues external simulated USB-HID mouse click commands with adjustable timing controls in order to conduct motor evoked potential experiments.

automated clinical systems, such as the `Natus XLTek EMU128FS` (Natus Medical, Pleasanton, CA, USA), fully optically isolated DC-float synchronization solutions must be used.

6.4.1 Design

A safety-isolated dual-channel flexible audio and photodiode trigger for electrophysiological recording time synchronization and verification.

The board has 2 inputs: a mono audio trigger (3.5mm / 1/8" jack, stereo combined) and a photodiode.

The photodiode is generally mounted to a screen or other photo synchronization trigger, and its sensitivity is adjustable with a trim pot. It's powered by a single regulated > 5V low voltage source, usually a 9V battery. The audio jack is plugged into an audio synchronization trigger, and looks for any (3Hz highpassed) audio input higher than 0.7 V. The audio half is powered by a mini-USB cable which may be hooked up to wall AC at some point, and the entire audio input is optically isolated from the photo trigger half of the board.

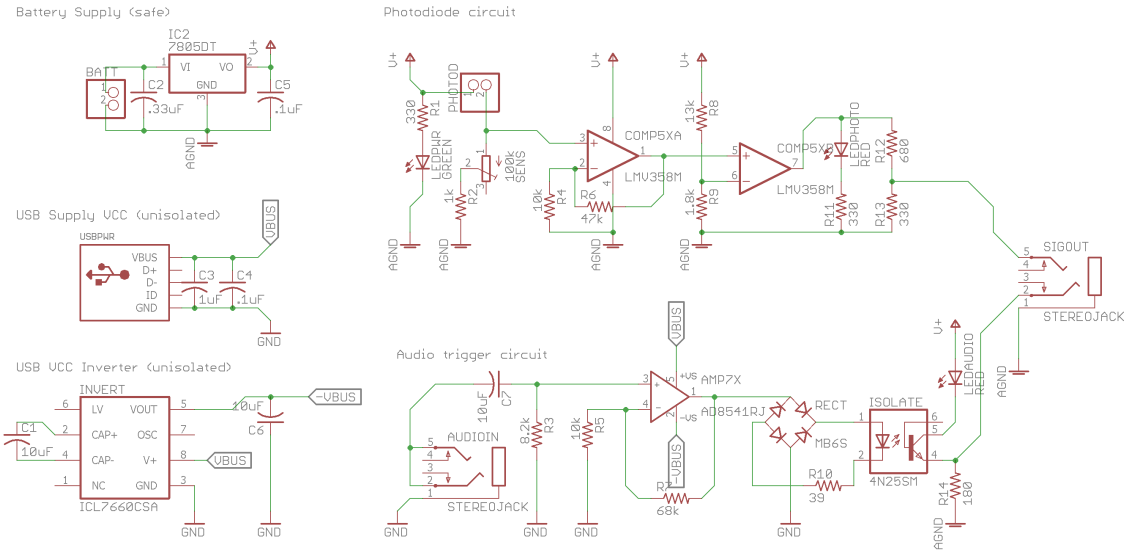

Figure 6.7: Analog isolation board schematic.

The output is an additional 3.5mm (1/8") audio jack with the L channel (tip) carrying the (rectified, amplified, isolated) audio trigger signal and the R channel (ring) carrying the (amplified) photodiode signal. Both channel should swing from 0 (off) - 2V (trigger on) with the standard BOM items.

The design allows for this board to be "trigger glue" between a psychophysical presentation (audio or on-screen stimuli) and electrophysiological recording systems when sub-millisecond synchronization is required, such as for neurostimulation. Note that output voltages are still in the < 2V range with a single-digit Ω output impedance and can be directly used with auxiliary inputs in recording systems.

However for in-vivo clinical recordings this should be further reduced as close as possible to the recording system via passive voltage dividers down to safe voltages and currents. For example $1k\Omega$ and $39k\Omega$ resistor voltage divider in order to achieve a $\frac{2V \cdot 1k\Omega}{1k\Omega+39k\Omega} = 50mV$ DC signal to fit within a common $\pm 250mV$ neural recording instrumentation dynamic range, and $\frac{2V}{1k\Omega+39k\Omega} = 50\mu A$ for all failure conditions for in-vivo recordings where this isolated synchronization signal is relayed to a clinical recording channel referenced to patient skull

reference, in compliance with IEC 60601 design standards.

This prototype schematic can be seen in Fig. 6.7 and Fig. 6.8. The assembled prototype can be seen in Fig. 6.9. The manufacturing files can be found at `https://github.com/uwgridlab/Lightmagic`.

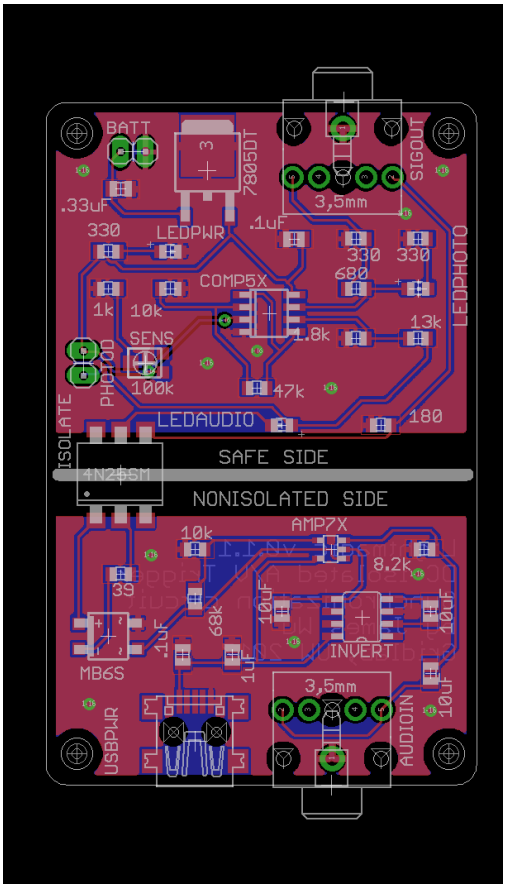

Figure 6.8: Analog isolation board render. Note the optoisolator and the separate ground planes between the computer-connected audio input portion (bottom) and the battery-supplied output portion (top), with galvanic isolation to any wall power.

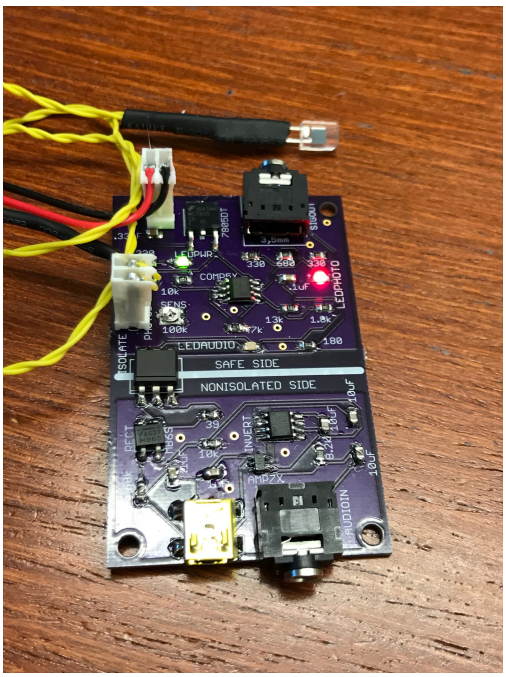

Figure 6.9: Analog isolation board, assembled, with a green power status LED and a red status LED indicating that the (L) ring channel is currently in the 'on' state, with the photodiode (top of photo) detecting light.

Appendix A

ADDITIONAL UPPER-LIMB NEUROENGINEERING STUDIES

A.1 Online 2D Closed-Loop Manual Manipulation BCI

Under the experimental paradigm indicated in Chapter 2, where a reduced non-negative basis was derived and a subject was actively instructed to adapt and match one of 4 grip postures and hold position for 10 seconds. Active dynamic control of 2 PCs in the postural space is fully enabled during this time. Over movement was allowed as needed.

Unfortunately, due to high gain and direction biases in classification, holding center targets in grasp posture was very difficult, and there was a lot of system bias against holding a flat grip.

Compared to chance of Gaussian distributed noise, the subject was able to perform above chance in two of four grasp types, and achieve a success rate of 47.5% in matching 10 grasp types and dwelling for an above-chance period of time.

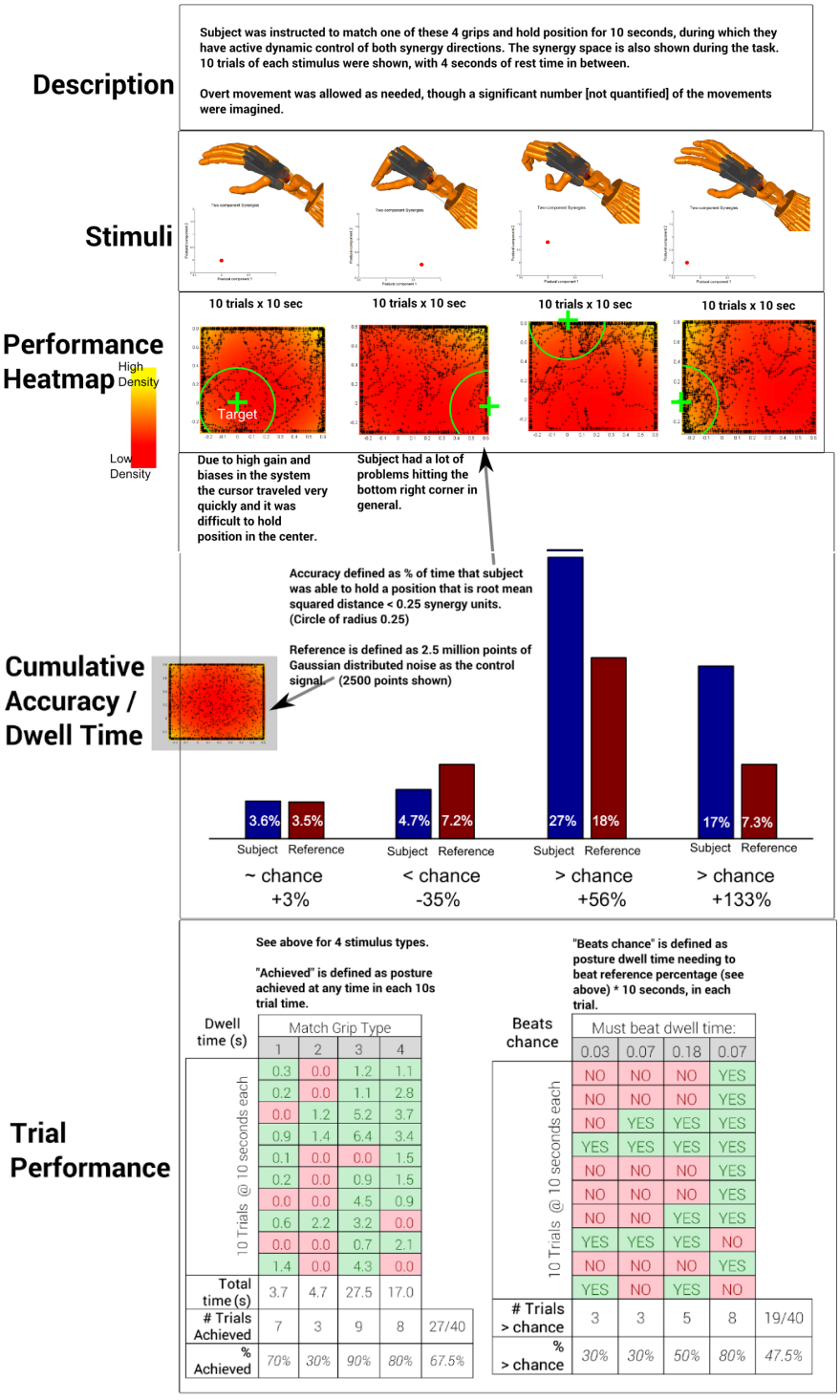

Figure A.1: Two-dimensional manual manipulation BCI testing and results.

BIBLIOGRAPHY

[1] Hans Moravec. *Mind Children: The Future of Robot and Human Intelligence*. Harvard University Press, 1988.

[2] Max Roser and Hannah Ritchie. Technological progress. *Our World in Data*, 2019. https://ourworldindata.org/technological-progress.

[3] Tomas Mikolov, Kai Chen, Greg Corrado, and Jeffrey Dean. Efficient Estimation of Word Representations in Vector Space. *arXiv:1301.3781 [cs]*, January 2013. arXiv: 1301.3781.

[4] Chen Li, Tingnan Zhang, and Daniel I. Goldman. A Terradynamics of Legged Locomotion on Granular Media. *Science*, 339(6126):1408–1412, March 2013.

[5] Brian S. Armour, Elizabeth A. Courtney-Long, Michael H. Fox, Heidi Fredine, and Anthony Cahill. Prevalence and causes of paralysis—united states, 2013. *American Journal of Public Health*, 106(10):1855–1857, oct 2016.

[6] Laura Specker Sullivan, Eran Klein, Tim Brown, Matthew Sample, Michelle Pham, Paul Tubig, Raney Folland, Anjali Truitt, and Sara Goering. Keeping disability in mind: A case study in implantable brain–computer interface research. *Science and Engineering Ethics*, jun 2017.

[7] Aiva Ievins and Chet T. Moritz. Therapeutic Stimulation for Restoration of Function After Spinal Cord Injury. *Physiology*, 32(5):391–398, August 2017.

[8] Glosser.ca. Derivative of file:artificial neural network.svg, cc by-sa 3.0. https://commons.wikimedia.org/w/index.php?curid=24913461, 2018.

[9] Tdunningvectorization. Own work, cc by 3.0. https://commons.wikimedia.org/w/index.php?curid=24913461, 2018.

[10] T. Wesley Mills (1847–1915). Wikidata: Q7792479, converted to vector by offnfopt - popular science monthly volume 42, public domain, https://commons.wikimedia.org/w/index.php?curid=52029745, 2018.

[11] Brian Litt. Dipoles and the EEG. *American Journal of EEG Technology*, 31(2):119–121, June 1991.

[12] Jonathan R. Wolpaw, Dennis J. McFarland, Gregory W. Neat, and Catherine A. Forneris. An EEG-based brain-computer interface for cursor control. *Electroencephalography and Clinical Neurophysiology*, 78(3):252–259, March 1991.

[13] Gert Pfurtscheller, Doris Flotzinger, and Joachim Kalcher. Brain-Computer Interface—a new communication device for handicapped persons. *Journal of Microcomputer Applications*, 16(3):293–299, July 1993.

[14] Jonathan R Wolpaw, Niels Birbaumer, Dennis J McFarland, Gert Pfurtscheller, and Theresa M Vaughan. Brain–computer interfaces for communication and control. *Clinical Neurophysiology*, 113(6):767–791, June 2002.

[15] Nathan E. Crone, Alon Sinai, and Anna Korzeniewska. High-frequency gamma oscillations and human brain mapping with electrocorticography. In Christa Neuper and Wolfgang Klimesch, editor, *Progress in Brain Research*, volume 159 of *Event-Related Dynamics of Brain Oscillations*, pages 275–295. Elsevier, 2006.

[16] D. J. Krusienski and J. J. Shih. Control of a brain–computer interface using stereotactic depth electrodes in and adjacent to the hippocampus. *Journal of Neural Engineering*, 8(2):025006, March 2011.

[17] Naohiro Takemura, Takao Fukui, and Toshio Inui. A Computational Model for Aperture Control in Reach-to-Grasp Movement Based on Predictive Variability. *Frontiers in Computational Neuroscience*, 9, 2015.

[18] T. Flash and N. Hogan. The coordination of arm movements: an experimentally confirmed mathematical model. *The Journal of Neuroscience*, 5(7):1688–1703, July 1985.

[19] Christopher M. Harris and Daniel M. Wolpert. Signal-dependent noise determines motor planning. *Nature*, 394(6695):780–784, August 1998.

[20] Emanuel Todorov and Michael I. Jordan. Optimal feedback control as a theory of motor coordination. *Nature Neuroscience*, 5(11):1226–1235, November 2002.

[21] Emanuel Todorov. Optimality principles in sensorimotor control. *Nature Neuroscience*, 7(9):907–915, September 2004.

[22] J O'Keefe, N Burgess, J G Donnett, K J Jeffery, and E A Maguire. Place cells, navigational accuracy, and the human hippocampus. *Philosophical Transactions of the Royal Society B: Biological Sciences*, 353(1373):1333–1340, August 1998.

[23] Torkel Hafting, Marianne Fyhn, Tora Bonnevie, May-Britt Moser, and Edvard I. Moser. Hippocampus-independent phase precession in entorhinal grid cells. *Nature*, 453(7199):1248–1252, June 2008.

[24] Tsuneyuki Kobayashi, Hisao Nishijo, Masaji Fukuda, Jan Bures, and Taketoshi Ono. Task-Dependent Representations in Rat Hippocampal Place Neurons. *Journal of Neurophysiology*, 78(2):597–613, August 1997.

[25] J. Bures, A. A. Fenton, Yu Kaminsky, and L. Zinyuk. Place cells and place navigation. *Proceedings of the National Academy of Sciences*, 94(1):343–350, January 1997.

[26] P. E. Sharp and C. Green. Spatial correlates of firing patterns of single cells in the subiculum of the freely moving rat. *Journal of Neuroscience*, 14(4):2339–2356, April 1994.

[27] John W. Krakauer, Claude Ghez, and M. Felice Ghilardi. Adaptation to Visuomotor Transformations: Consolidation, Interference, and Forgetting. *Journal of Neuroscience*, 25(2):473–478, January 2005.

[28] John W. Krakauer. Motor Learning and Consolidation: The Case of Visuomotor Rotation. *Advances in experimental medicine and biology*, 629:405–421, 2009.

[29] Jinsung Wang and Robert L. Sainburg. Adaptation to Visuomotor Rotations Remaps Movement Vectors, Not Final Positions. *Journal of Neuroscience*, 25(16):4024–4030, April 2005.

[30] Jeremiah D Wander and Rajesh PN Rao. Brain–computer interfaces: a powerful tool for scientific inquiry. *Current Opinion in Neurobiology*, 25:70–75, April 2014.

[31] Jerry J. Shih, Dean J. Krusienski, and Jonathan R. Wolpaw. Brain-Computer Interfaces in Medicine. *Mayo Clinic Proceedings*, 87(3):268–279, March 2012.

[32] Janis J Daly and Jonathan R Wolpaw. Brain–computer interfaces in neurological rehabilitation. *The Lancet Neurology*, 7(11):1032–1043, November 2008.

[33] N. E. Crone, D. L. Miglioretti, B. Gordon, and R. P. Lesser. Functional mapping of human sensorimotor cortex with electrocorticographic spectral analysis. II. Event-related synchronization in the gamma band. *Brain*, 121(12):2301–2315, December 1998.

[34] N. E. Crone, D. L. Miglioretti, B. Gordon, J. M. Sieracki, M. T. Wilson, S. Uematsu, and R. P. Lesser. Functional mapping of human sensorimotor cortex with electrocorticographic spectral analysis. I. Alpha and beta event-related desynchronization. *Brain*, 121(12):2271–2299, December 1998.

[35] J. F. Marsden, K. J. Werhahn, P. Ashby, J. Rothwell, S. Noachtar, and P. Brown. Organization of Cortical Activities Related to Movement in Humans. *The Journal of Neuroscience*, 20(6):2307–2314, March 2000.

[36] S. Ohara, T. Nagamine, A. Ikeda, T. Kunieda, R. Matsumoto, W. Taki, N. Hashimoto, K. Baba, T. Mihara, S. Salenius, and H. Shibasaki. Electrocorticogram-electromyogram coherence during isometric contraction of hand muscle in human. *Clinical Neurophysiology: Official Journal of the International Federation of Clinical Neurophysiology*, 111(11):2014–2024, November 2000.

[37] Takeshi Satow, Masao Matsuhashi, Akio Ikeda, Junichi Yamamoto, Motohiro Takayama, Tahamina Begum, Tatsuya Mima, Takashi Nagamine, Nobuhiro Mikuni, Susumu Miyamoto, Nobuo Hashimoto, and Hiroshi Shibasaki. Distinct cortical areas for motor preparation and execution in human identified by Bereitschaftspotential recording and ECoG-EMG coherence analysis. *Clinical Neurophysiology*, 114(7):1259–1264, July 2003.

[38] Kai J. Miller, Eric C. Leuthardt, Gerwin Schalk, Rajesh P. N. Rao, Nicholas R. Anderson, Daniel W. Moran, John W. Miller, and Jeffrey G. Ojemann. Spectral Changes in Cortical Surface Potentials during Motor Movement. *The Journal of Neuroscience*, 27(9):2424–2432, February 2007.

[39] Eric C. Leuthardt, Gerwin Schalk, Jonathan R. Wolpaw, Jeffrey G. Ojemann, and Daniel W. Moran. A brain–computer interface using electrocorticographic signals in humans. *Journal of Neural Engineering*, 1(2):63, June 2004.

[40] Allen R. Wyler, George A. Ojemann, Ettore Lettich, and Arthur A. Ward. Subdural strip electrodes for localizing epileptogenic foci. *Journal of Neurosurgery*, 60(6):1195–1200, June 1984.

[41] P. Shenoy, K.J. Miller, J.G. Ojemann, and R. P N Rao. Generalized Features for Electrocorticographic BCIs. *IEEE Transactions on Biomedical Engineering*, 55(1):273–280, January 2008.

[42] G. Schalk, K. J. Miller, N. R. Anderson, J. A. Wilson, M. D. Smyth, J. G. Ojemann, D. W. Moran, J. R. Wolpaw, and E. C. Leuthardt. Two-dimensional movement control

using electrocorticographic signals in humans. *Journal of Neural Engineering*, 5(1):75, March 2008.

[43] J. Lin, Ying Wu, and T.S. Huang. Modeling the constraints of human hand motion. In *Workshop on Human Motion, 2000. Proceedings*, pages 121–126, 2000.

[44] Tobias Pistohl, Tonio Ball, Andreas Schulze-Bonhage, Ad Aertsen, and Carsten Mehring. Prediction of arm movement trajectories from ECoG-recordings in humans. *Journal of Neuroscience Methods*, 167(1):105–114, January 2008.

[45] Tonio Ball, Andreas Schulze-Bonhage, Ad Aertsen, and Carsten Mehring. Differential representation of arm movement direction in relation to cortical anatomy and function. *Journal of Neural Engineering*, 6(1):016006, February 2009.

[46] P. Shenoy, K.J. Miller, J.G. Ojemann, and R.P.N. Rao. Finger Movement Classification for an Electrocorticographic BCI. In *3rd International IEEE/EMBS Conference on Neural Engineering, 2007. CNE '07*, pages 192–195, May 2007.

[47] Kai J. Miller, Larry B. Sorensen, Jeffrey G. Ojemann, and Marcel den Nijs. Power-Law Scaling in the Brain Surface Electric Potential. *PLOS Computational Biology*, 5(12):e1000609, December 2009.

[48] J. Kubánek, K. J. Miller, J. G. Ojemann, J. R. Wolpaw, and G. Schalk. Decoding flexion of individual fingers using electrocorticographic signals in humans. *Journal of Neural Engineering*, 6(6):066001, December 2009.

[49] Soumyadipta Acharya, Matthew S. Fifer, Heather L. Benz, Nathan E. Crone, and Nitish V. Thakor. Electrocorticographic amplitude predicts finger positions during slow grasping motions of the hand. *Journal of Neural Engineering*, 7(4):046002, August 2010.

[50] M. G. Bleichner, Z. V. Freudenburg, J. M. Jansma, E. J. Aarnoutse, M. J. Vansteensel, and N. F. Ramsey. Give me a sign: decoding four complex hand gestures based on high-density ECoG. *Brain Structure and Function*, pages 1–14, October 2014.

[51] Matthew S. Fifer, Soumyadipta Acharya, Heather L. Benz, Mohsen Mollazadeh, Nathan E. Crone, and Nitish V. Thakor. Towards Electrocorticographic Control of a Dexterous Upper Limb Prosthesis. *IEEE pulse*, 3(1):38–42, January 2012.

[52] Nanying Liang and Laurent Bougrain. Decoding Finger Flexion from Band-Specific ECoG Signals in Humans. *Frontiers in Neuroscience*, 6, June 2012.

[53] Tobias Pistohl, Thomas Sebastian Benedikt Schmidt, Tonio Ball, Andreas Schulze-Bonhage, Ad Aertsen, and Carsten Mehring. Grasp Detection from Human ECoG during Natural Reach-to-Grasp Movements. *PLoS ONE*, 8(1):e54658, January 2013.

[54] Jie Wang, Lu Yang, Long Gao, and Qiang Miao. Current progress on weak signal detection. In *2013 International Conference on Quality, Reliability, Risk, Maintenance, and Safety Engineering (QR2MSE)*, pages 1812–1818, July 2013.

[55] M. Spüler, A. Walter, A. Ramos-Murguialday, G. Naros, N. Birbaumer, A. Gharabaghi, W. Rosenstiel, and M. Bogdan. Decoding of motor intentions from epidural ECoG recordings in severely paralyzed chronic stroke patients. *Journal of Neural Engineering*, 11(6):066008, December 2014.

[56] Arthur D. Kuo. A mechanical analysis of force distribution between redundant, multiple degree-of-freedom actuators in the human: Implications for the central nervous system. *Human Movement Science*, 13(5):635–663, October 1994.

[57] F A Mussa-Ivaldi, S F Giszter, and E Bizzi. Linear combinations of primitives in vertebrate motor control. *Proceedings of the National Academy of Sciences of the United States of America*, 91(16):7534–7538, August 1994.

[58] M. Desmurget, C. Prablanc, Y. Rossetti, M. Arzi, Y. Paulignan, C. Urquizar, and J. C. Mignot. Postural and synergic control for three-dimensional movements of reaching and grasping. *Journal of Neurophysiology*, 74(2):905–910, August 1995.

[59] Marco Santello, Martha Flanders, and John F. Soechting. Postural Hand Synergies for Tool Use. *The Journal of Neuroscience*, 18(23):10105–10115, December 1998.

[60] G. Schalk, D.J. McFarland, T. Hinterberger, N. Birbaumer, and J.R. Wolpaw. BCI2000: a general-purpose brain-computer interface (BCI) system. *IEEE Transactions on Biomedical Engineering*, 51(6):1034–1043, June 2004.

[61] Colin M. Light, Paul H. Chappell, and Peter J. Kyberd. Establishing a standardized clinical assessment tool of pathologic and prosthetic hand function: Normative data, reliability, and validity. *Archives of Physical Medicine and Rehabilitation*, 83(6):776–783, June 2002.

[62] Naaz Kapadia, Vera Zivanovic, Molly Verrier, and Milos R. Popovic. Toronto Rehabilitation Institute-Hand Function Test: Assessment of Gross Motor Function in Individuals With Spinal Cord Injury. *Topics in Spinal Cord Injury Rehabilitation*, 18(2):167–186, 2012.

[63] Vikash Kumar, Jing Wu, Emo Todorov, Jeffrey G Ojemann, and Rajesh P. N. Rao. A high-fidelity robotic platform for the development of closed-loop invasive brain-computer interfaces for motor control, 2014.

[64] V. Kumar, Zhe Xu, and E. Todorov. Fast, strong and compliant pneumatic actuation for dexterous tendon-driven hands. In *2013 IEEE International Conference on Robotics and Automation (ICRA)*, pages 1512–1519, May 2013.

[65] F. Fritsch and R. Carlson. Monotone Piecewise Cubic Interpolation. *SIAM Journal on Numerical Analysis*, 17(2):238–246, April 1980.

[66] Katie Ly, Jing Wu, Lila Levinson, Benjamin Shuman, Katherine Steele, Jeffrey Ojemann, and Rajesh Rao. Electrocorticographic dynamics predict sustained grasping and upper-limb kinetic output. In *2018 IEEE International Conference on Systems, Man, and Cybernetics (SMC)*. IEEE, oct 2018.

[67] J. Cronin, J. Wu, K. Collins, D. Sarma, R. Rao, J. Ojemann, and J. Olson. Task-Specific Somatosensory Feedback via Cortical Stimulation in Humans. *IEEE Transactions on Haptics*, PP(99):1–1, 2016.

[68] E.C. Leuthardt, K.J. Miller, G. Schalk, R. P N Rao, and J.G. Ojemann. Electrocorticography-based brain computer Interface-the seattle experience. *IEEE Transactions on Neural Systems and Rehabilitation Engineering*, 14(2):194–198, June 2006.

[69] J. Wu, B. R. Shuman, B. W. Brunton, K. M. Steele, J. D. Olson, R. P. N. Rao, and J. G. Ojemann. Multistep model for predicting upper-limb 3d isometric force application from pre-movement electrocorticographic features. In *2016 38th Annual International Conference of the IEEE Engineering in Medicine and Biology Society (EMBC)*, pages 1564–1567, August 2016.

[70] Nicholas R. Anderson, Tim Blakely, Gerwin Schalk, Eric C. Leuthardt, and Daniel W. Moran. Electrocorticographic (ECoG) correlates of human arm movements. *Experimental Brain Research*, 223(1):1–10, September 2012.

[71] Kai J Miller, Christopher J Honey, Dora Hermes, Rajesh PN Rao, Marcel denNijs, and Jeffrey G Ojemann. Broadband changes in the cortical surface potential track activation of functionally diverse neuronal populations. *NeuroImage*, 85, Part 2:711–720, January 2014.

[72] Lindsay R. Bremner and Richard A. Andersen. Coding of the Reach Vector in Parietal Area 5d. *Neuron*, 75(2):342–351, July 2012.

[73] P. S. Archambault, S. Ferrari-Toniolo, R. Caminiti, and A. Battaglia-Mayer. Visually-guided correction of hand reaching movements: The neurophysiological bases in the cerebral cortex. *Vision Research*, September 2014.

[74] Stefan Schaffelhofer, Andres Agudelo-Toro, and Hansjörg Scherberger. Decoding a Wide Range of Hand Configurations from Macaque Motor, Premotor, and Parietal Cortices. *The Journal of Neuroscience*, 35(3):1068–1081, January 2015.

[75] Hai Sun, Timothy M. Blakely, Felix Darvas, Jeremiah D. Wander, Lise A. Johnson, David K. Su, Kai J. Miller, Eberhard E. Fetz, and Jeffery G. Ojemann. Sequential activation of premotor, primary somatosensory and primary motor areas in humans during cued finger movements. *Clinical Neurophysiology*, 126(11):2150–2161, November 2015.

[76] Zuoguan Wang, Aysegul Gunduz, Peter Brunner, Anthony L. Ritaccio, Qiang Ji, and Gerwin Schalk. Decoding onset and direction of movements using Electrocorticographic (ECoG) signals in humans. *Frontiers in Neuroengineering*, 5:15, 2012.

[77] Dora Hermes, Kai J. Miller, Herke Jan Noordmans, Mariska J. Vansteensel, and Nick F. Ramsey. Automated electrocorticographic electrode localization on individually rendered brain surfaces. *Journal of Neuroscience Methods*, 185(2):293–298, January 2010.

[78] G. Schalk, J. Kubánek, K. J. Miller, N. R. Anderson, E. C. Leuthardt, J. G. Ojemann, D. Limbrick, D. Moran, L. A. Gerhardt, and J. R. Wolpaw. Decoding two-dimensional movement trajectories using electrocorticographic signals in humans. *Journal of Neural Engineering*, 4(3):264, September 2007.

[79] Sajid M. Siddiqi, Byron Boots, and Geoffrey J. Gordon. Reduced-Rank Hidden Markov Models. *arXiv:0910.0902 [cs]*, October 2009. arXiv: 0910.0902.

[80] Mark M. Churchland, John P. Cunningham, Matthew T. Kaufman, Justin D. Foster, Paul Nuyujukian, Stephen I. Ryu, and Krishna V. Shenoy. Neural population dynamics during reaching. *Nature*, 487(7405):51–56, July 2012.

[81] Yaqian Guo, Trevor Hastie, and Robert Tibshirani. Regularized linear discriminant analysis and its application in microarrays. *Biostatistics*, 8(1):86–100, January 2007.

[82] Robert Tibshirani. Regression Shrinkage and Selection via the Lasso. *Journal of the Royal Statistical Society. Series B (Methodological)*, 58(1):267–288, 1996.

[83] J. Wu, K. Casimo, D. J. Caldwell, R. P. N. Rao, and J. G. Ojemann. Electrocorticographic dynamics predict visually guided motor imagery of grasp shaping. In *2017 8th*

International IEEE/EMBS Conference on Neural Engineering (NER), pages 199–202, May 2017.

[84] Tobias Pistohl, Andreas Schulze-Bonhage, Ad Aertsen, Carsten Mehring, and Tonio Ball. Decoding natural grasp types from human ECoG. *NeuroImage*, 59(1):248–260, January 2012.

[85] K.J. Miller, T. Blakely, G. Schalk, M. den Nijs, R. P N Rao, and J.G. Ojemann. Three cases of feature correlation in an electrocorticographic BCI. In *30th Annual International Conference of the IEEE Engineering in Medicine and Biology Society, 2008. EMBS 2008*, pages 5318–5321, August 2008.

[86] Jiri Hammer, Jörg Fischer, Johanna Ruescher, Andreas Schulze-Bonhage, Ad Aertsen, and Tonio Ball. The role of ECoG magnitude and phase in decoding position, velocity, and acceleration during continuous motor behavior. *Neuroprosthetics*, 7:200, 2013.

[87] Kai J. Miller, Gerwin Schalk, Eberhard E. Fetz, Marcel den Nijs, Jeffrey G. Ojemann, and Rajesh P. N. Rao. Cortical activity during motor execution, motor imagery, and imagery-based online feedback. *Proceedings of the National Academy of Sciences*, 107(9):4430–4435, March 2010.

[88] Jonathan C. Kao, Paul Nuyujukian, Stephen I. Ryu, Mark M. Churchland, John P. Cunningham, and Krishna V. Shenoy. Single-trial dynamics of motor cortex and their applications to brain-machine interfaces. *Nature Communications*, 6, July 2015.

[89] V. Kumar and E. Todorov. MuJoCo HAPTIX: A virtual reality system for hand manipulation. In *2015 IEEE-RAS 15th International Conference on Humanoid Robots (Humanoids)*, pages 657–663, November 2015.

[90] Byron M. Yu, John P. Cunningham, Gopal Santhanam, Stephen I. Ryu, Krishna V. Shenoy, and Maneesh Sahani. Gaussian-Process Factor Analysis for Low-Dimensional Single-Trial Analysis of Neural Population Activity. *Journal of Neurophysiology*, 102(1):614–635, July 2009.

[91] G. G. Brown. Perception Op Depth with Disoriented Vision. *British Journal of Psychology. General Section*, 19(2):117–146, 1928.

[92] Adriana Fiorentini, C. Ghez, and L. Maffei. Physiological correlates of adaptation to a rotated visual field. *The Journal of Physiology*, 227(1):313–322, December 1972.

[93] T. A. Martin, J. G. Keating, H. P. Goodkin, A. J. Bastian, and W. T. Thach. Throwing while looking through prismsII. Specificity and storage of multiple gaze—throw calibrations. *Brain*, 119(4):1199–1211, August 1996.

[94] Douglas P. Field, Thomas F. Shipley, and Douglas W. Cunningham. Prism adaptation to dynamic events. *Perception & Psychophysics*, 61(1):161–176, January 1999.

[95] Pierre Baraduc and Daniel M. Wolpert. Adaptation to a Visuomotor Shift Depends on the Starting Posture. *Journal of Neurophysiology*, 88(2):973–981, August 2002.

[96] Steve M. Kim, Surya Ganguli, and Loren M. Frank. Spatial Information Outflow from the Hippocampal Circuit: Distributed Spatial Coding and Phase Precession in the Subiculum. *Journal of Neuroscience*, 32(34):11539–11558, August 2012.

[97] Jacob M. Olson, Kanyanat Tongprasearth, and Douglas M. Nitz. Subiculum neurons map the current axis of travel. *bioRxiv*, page 050641, April 2016.

[98] Sang Ah Lee, Jonathan F. Miller, Andrew J. Watrous, Michael R. Sperling, Ashwini Sharan, Gregory A. Worrell, Brent M. Berry, Joshua P. Aronson, Kathryn A. Davis, Robert E. Gross, Bradley Lega, Sameer Sheth, Sandhitsu R. Das, Joel M. Stein, Richard Gorniak, Daniel S. Rizzuto, and Joshua Jacobs. Electrophysiological Signatures of Spatial Boundaries in the Human Subiculum. *Journal of Neuroscience*, 38(13):3265–3272, March 2018.

[99] Jing Wu, David J Caldwell, Kaitlyn Casimo, Jeffrey G Ojemann, and Rajesh PN Rao. Interactive web application for exploring matrices of neural connectivity. In *2017 8th International IEEE/EMBS Conference on Neural Engineering (NER)*, pages 42–45. IEEE, 2017.

[100] Raymond Salvador, John Suckling, Christian Schwarzbauer, and Ed Bullmore. Undirected graphs of frequency-dependent functional connectivity in whole brain networks. *Philosophical Transactions of the Royal Society B: Biological Sciences*, 360(1457):937–946, 2005.

[101] Basak Alper, Benjamin Bach, Nathalie Henry Riche, Tobias Isenberg, and Jean-Daniel Fekete. Weighted graph comparison techniques for brain connectivity analysis. In *Proceedings of the SIGCHI conference on human factors in computing systems*, pages 483–492. ACM, 2013.

[102] Benjamin Bach, Conglei Shi, Nicolas Heulot, Tara Madhyastha, Tom Grabowski, and Pierre Dragicevic. Time curves: Folding time to visualize patterns of temporal evolution in data. *IEEE transactions on visualization and computer graphics*, 22(1):559–568, 2016.

[103] Michael Bostock, Vadim Ogievetsky, and Jeffrey Heer. D^3 data-driven documents. *IEEE transactions on visualization and computer graphics*, 17(12):2301–2309, 2011.

[104] Martin Krzywinski, Jacqueline Schein, Inanc Birol, Joseph Connors, Randy Gascoyne, Doug Horsman, Steven J Jones, and Marco A Marra. Circos: an information aesthetic for comparative genomics. *Genome research*, 19(9):1639–1645, 2009.

[105] Jeffrey Heer and Michael Bostock. Crowdsourcing graphical perception: using mechanical turk to assess visualization design. In *Proceedings of the SIGCHI conference on human factors in computing systems*, pages 203–212. ACM, 2010.

[106] Kaitlyn Casimo, Felix Darvas, Jeremiah Wander, Andrew Ko, Thomas J. Grabowski, Edward Novotny, Andrew Poliakov, Jeffrey G. Ojemann, and Kurt E. Weaver. Regional Patterns of Cortical Phase Synchrony in the Resting State. *Brain Connectivity*, 6(6):470–481, March 2016.

[107] Kenneth O McGraw and Seok P Wong. Forming inferences about some intraclass correlation coefficients. *Psychological methods*, 1(1):30, 1996.

[108] Supratim Ray, Nathan E Crone, Ernst Niebur, Piotr J Franaszczuk, and Steven S Hsiao. Neural correlates of high-gamma oscillations (60–200 hz) in macaque local field potentials and their potential implications in electrocorticography. *Journal of Neuroscience*, 28(45):11526–11536, 2008.

[109] James J Knierim, Joshua P Neunuebel, and Sachin S Deshmukh. Functional correlates of the lateral and medial entorhinal cortex: objects, path integration and local–global reference frames. *Philosophical Transactions of the Royal Society B: Biological Sciences*, 369(1635):20130369, 2014.